University of Trento
Department of Civil, Environmental and Mechanical Engineering

DOCTORAL SCHOOL IN ENGINEERING OF
CIVIL AND MECHANICAL STRUCTURAL SYSTEMS
XXVIII CYCLE

Performance Optimisation of Dielectric Elastomer Generators

Author:
Eliana Bortot

Supervisor:
Prof. Massimiliano Gei

November 2015

University of Trento
University of Bergamo
University of Brescia
University of Padova
University of Trieste
University of Udine
IUAV University of Venezia

Doctoral School in
Engineering of Civil and Mechanical Structural Systems

XXVIII cycle

Head of the Doctoral School:

Prof. Davide Bigoni, University of Trento (Italy)

Final examination: 17/12/2015

Board of Examiners:

Prof. Nicola Pugno, University of Trento (Italy)

Prof. Maria Adelaide Parisi, Polytechnic of Milan (Italy)

Dr. Giuseppe Zurlo, National University of Galway (Ireland)

“Non esiste una dignità della ricerca, perché nessuno può dire con sicurezza che una data ricerca non serve nè servirà mai a nulla. [...] Possiamo solo fabbricare mattoni, mattoni universali, con cui sia possibile fare qualsiasi cosa. Possiamo farci case, torri, ospedali, e persino fabbriche di mattoni. Ed è nostro dovere farli solidi, più solidi possibile, affinché le torri che edificheremo con quei mattoni possano arrivare più in alto possibile, e durare oltre le nostre vite.”

“It is impossible to set a worthiness upon a scientific research, because of the lack of certainty that a given research is definitely needed and useful. [...] What we can do is just to make bricks, universal bricks, with which it would be possible to do anything. We can build houses, towers, hospitals, and even brick factories. And our duty is to make them strong, the stronger the better, so that the towers which we are going to build with those bricks could reach the maximum heights and last beyond our lives.”

Marco Malvaldi
”Argento vivo”

Summary

A Dielectric Elastomer Generator (DEG) is an electromechanical transducer, basically a highly deformable parallel-plate capacitor, made up of a soft DE membrane coated with two compliant electrodes on its opposite surfaces. This device is able to convert mechanical work, emanating from its interaction with the environment, into electrical energy. The capacitance depends on the deformation undergone by the membrane, and its variability can be exploited to extract electric energy by (*i*) initially stretching, (*ii*) then charging the capacitor, (*iii*) subsequently releasing the stretch and finally (*iv*) harvesting the charge at a higher electric potential.

The *optimisation procedure* for a load-driven soft planar DEG is presented, assuming hyperelastic and ideal dielectric behaviour. The DEG undergoes the ideal four-stroke electromechanical cycle previously described and its performance is evaluated on the basis of the energy extracted during a cycle and of the efficiency, defined as the ratio of the harvested energy on the total invested energy. The amount of extracted energy is limited due to possible failures of the device, which are, in the most general case, electric breakdown, material rupture, buckling-like instabilities due to loss of the tensile stress state and electromechanical instability. These failure mechanisms determine the allowable state region for the generator. Hence, in order to identify the best cycle that complies with these limits, a constrained optimisation problem is formulated and the generator performance is estimated. For the different loading cases examined, namely equibiaxial stress state and plane strain, numerical results show, as expected, a critical dependence of the harvested energy on the ultimate stretch ratio and, against expectations, a universal limit on the dielectric strength of the DE membrane beyond which the optimal cycle is independent of this parameter. Thus, there is an upper bound on the harvested energy, which depends only on the ultimate stretch ratio.

In addition to the simple parallel-plate configuration, an annular DEG deforming *out-of-plane* has been analysed. In this configuration the generator is made up of an annular membrane constrained at the boundary by a rigid ring and at the centre by a rigid plate, on which an external force is applied. Due to the loading, the membrane deforms *non-homogeneously* out-of-plane. In order to avoid loss of the tensile stress state, electric breakdown and electromechanical instability, the applied voltage is controlled, thereby limiting the maximum voltage and keeping the maximum stretch in an admissible range. Numerical results show that the prestretch of the membrane is crucial for an effective behaviour of the device. In fact, the unprestretched generator performs poorly with regard to both energy and efficiency. A small prestretch, of approximately 5%, ensure a sixfold improvement in the gained energy and a fivefold increment in efficiency. The performance of the generator is evaluated for different values of the applied load and

of the prestretch. This analysis shows that increasing the applied force the harvested energy increases monotonically, while the efficiency increases until a peak value and then decreases. Hence, for an out-of-plane DEG, the choice of the applied force is decisive to ensure a good trade-off among energy and efficiency. Moreover, a comparison of different DEG layouts demonstrates that the annular DEG can compete with the equibiaxial planar generator, in terms not only of efficiency, but also of harvested energy.

What has been so far pointed out is valid under the hypothesis of ideal, lossless material. Since polymers are affected by *time-dependent effects*, this hypothesis appears to be not completely realistic. Indeed, a predicting model for soft dielectric elastomer generators must include a realistic model of the electro-mechanical behaviour of the elastomer filling, the variable capacitor and of the electrical circuit connecting all the device components. To this end, the ideality assumption of the material and of the cycle has to be removed. Hence, a complete framework for a reliable simulation of soft energy harvesters is proposed for a soft viscous dielectric elastomer generator, operating in an electrical circuit for energy harvesting and subjected to a periodic mechanical stretch. The electrical model of the generator takes into account the effects of the electrodes and of the conductivity current through the dielectric material. A *phenomenological electro-viscoelastic model* at large strain is proposed and calibrated on the basis of experimental data available in literature for a polyacrylate elastomer (VHB-4910). The effects of viscoelasticity and of possible changes of the permittivity with strains on the generator performance are hence investigated. Numerical results underline the importance of time-dependent effects on the evaluation of the generator performance. The main outcome of this analysis is that, compared with a hyperelastic model, the efficiency is reduced by viscoelasticity for high values of the mean stretch and of the amplitude of stretch oscillation. The reduction is almost insensitive of the mechanical frequency while the efficiency is further reduced by the variation of the permittivity with strain. Moreover, viscoelastic effects modify the allowable state region of the generator. At regime condition, the failure curves relative to electromechanical instability and to loss of the tensile stress state are strongly modified by the viscous effects. This fact results in the alteration of the allowable state region of the generator. Furthermore, due to the change in shape and size of the admissible region under this condition, a more surprising result is the fact that the natural configuration ($\lambda = 1$) is a not-allowed state. As a consequence, there is an upper bound on the maximal stretch oscillation amplitude. Focusing on the main features of the electrical circuit, an important outcome of the analysis is the identification of a value range of the external electric load for which the efficiency is maximal. Furthermore, the viscous dissipation of the material dominates the energy loss arising from the leakage current across the dielectric membrane.

Acknowledgements

This dissertation collects the researches I carried out during the last three years as a Ph.D. student at the Dept. of Civil, Environmental and Mechanical Engineering of the University of Trento. I would like to take this opportunity to thank the people who have supported me during this work.

First of all, I would like to express my sincere gratitude to my advisor, Prof. Massimiliano Gei, for his patience, remarks, suggestions and encouragement throughout these years. I am deeply grateful to him for believing in me, working with him sincerely contributes to my scientific and personal growth.

I would like also to thank Dr. Roberta Springhetti, who provided me the opportunity to join the research on EAPs, for her unfailing presence.

I am deeply thankful to all members of the group of Solid and Structural Mechanics at the University of Trento: Prof. Davide Bigoni, Prof. Luca Deseri, Prof. Nicola Pugno, Prof. Andrea Piccolroaz, Dr. Francesco Dal Corso and Dr. Fiorella Pantano. I would like to thank all my current and former colleagues, in particular Dr. Luca Argani, Dr. Federico Bosi, Dr. Aldo Madaschi, Dr. Diego Misseroni, Dr. Lorenzo Morini, Stefano Signetti, Pietro Pollaci, Summer Shazad, Costanza Armanini, Nicola Bordigon and Mirko Tommasini.

I am deeply indebted to Prof. Gal deBotton for his cooperation during these three years. His valuable suggestions and his friendly words of advice guided me through this research path since the beginning.

I would like to express my deepest gratitude to Prof. Andreas Menzel for his strong support, encouragement and his confidence in my work. I am also deeply grateful to the whole group of the Institute of Mechanics at TU Dortmund for their friendly and warm hospitality during my four-month stay in 2013 and for making me feel part of the ”family” even after: Prof. Jörn Mosler, Prof. Björn Kiefer, Dr. Thorsten Bartel, Dr. Guillermo Dìaz Ortìz, Dr. Krishnendu Haldar, Dr. Richard Ostwald, Dr. Tobias Waffenschmidt, Alexander Bartels, Rolf Berthelsen, Karsten Buckmann, Cèsar Polindara, Raphael Holtermann, Dinesh Kumar Dusthakar, Maniprakash Subramanian and the wonderful secretaries Tina McDonagh and Kerstin Walter.

Special thanks go to Prof. Ralf Denzer, former member of the Institute of Mechanics at TU Dortmund and now working at Lund University, for his constant support, for the scientific discussions and the friendly chats. His precious teachings and help have been decisive to the success of this work.

Last but not the least, I have to thank my family: my dad Fabio, my mom Francesca, my aunt Maristella and my grandmother Angela. Without their everlasting support, their patience, understanding and love this work would not have been possible.

Trento, December 2015

Eliana Bortot

List of publications

The main results presented in this thesis have been published in the following publications:

- Bortot, E., Springhetti, R., Gei, M. (2014) Enhanced soft dielectric composite generators: The role of ceramic fillers. *Journal of the European Ceramic Society*, **34** (11), 2623-2632. doi:10.1016/j.jeurceramsoc.2013.12.014
- Springhetti, R., Bortot, E., DeBotton, G., Gei, M. (2014) Optimal energy-harvesting cycles for load-driven dielectric generators in plane strain. *IMA Journal of Applied Mathematics*, **79** (5), 929-946. doi:10.1093/imamat/hxu025
- Bortot, E., Denzer, R., Menzel, A., Gei, M. (2014) Analysis of a viscous soft dielectric elastomer generator operating in an electrical circuit. *Proceedings in Applied Mathematics and Mechanics*, **14** (1), 511-512. doi:10.1002/pamm.201410243
- Bortot, E., Springhetti, R., DeBotton, G., Gei, M. (2015) Optimization of load-driven soft dielectric elastomer generators. *Procedia IUTAM*, **22**, 42–51. doi:10.1016/j.piutam.2014.12.006
- Bortot, E., Gei, M., DeBotton, G. (2015) Optimal energy harvesting cycles for load-driven dielectric elastomer generators under equibiaxial deformation. *Meccanica*, **50** (11), 2751-2766. doi:10.1007/s11012-015-0213-1
- Bortot, E., Denzer, R., Menzel, A., Gei, M. (2015) Analysis of a viscous soft dielectric elastomer generator operating in an electrical circuit. *International Journal of Solids and Structures. In press.* doi:10.1016/j.ijsolstr.2015.06.004
- Bortot, E., Gei, M. (2015) Harvesting energy with an out-of-plane dielectric elastomer generator. *Proceedings in Applied Mathematics and Mechanics*, **15** (1), 379–380. doi:10.1002/pamm.201510180.
- Bortot, E., Gei, M. (2015) Harvesting energy with load-driven dielectric elastomer annular membranes deforming out-of-plane. *Extreme Mechanics Letters*, **5**, 62-73. doi:10.1016/j.eml.2015.09.009

Other results obtained during the Ph.D. course are reported in the following publications:

- Gei, M., Springhetti, R., Bortot, E. (2013) Performance of soft dielectric laminated composites. *Smart Materials and Structures*, **22** (10), 104014. doi:10.1088/0964-1726/22/10/104014

- Schlaak, H.F., Gei, M., Bortot, E., Haus, H., Mössinger, H. (2015) Dielectric Elastomer as EAPs: models. In Carpi F. (ed) *EAP Reference Book*, Springer. *In press.*

Contents

Summary **v**

Acknowledgements **vii**

List of Publications **ix**

Contents **xi**

List of Figures **xv**

List of Tables **xix**

Abbreviations **xxiii**

Physical Constants **xxv**

Symbols **xxvii**

1 Introduction **1**

2 Dielectric elastomer generators: theory **5**

2.1 Theoretical background: kinematics and governing equations 6
2.2 Energy-density functions for isotropic dielectric elastomers 8
2.3 Electro-hyperelastic model 9
  2.3.1 Plane-strain loading 10
  2.3.2 Equibiaxial loading 11
2.4 Electro-viscoelastic model 12
2.5 Load-driven harvesting cycle 14
2.6 Modes of failure and failure envelope 16
  2.6.1 Ideal hyperelastic DEG under plane-strain loading conditions . . . 17
  2.6.2 Ideal hyperelastic DEG under equibiaxial loading conditions 19
2.7 Performance of a dielectric elastomer generator: gained and invested energies, effectiveness and efficiency 22

3 Optimisation of an ideal DEG in plane-strain loading mode **25**

3.1 Constrained optimisation problem for plane-strain loading mode 26

3.1.1 The harvested energy H_g . . . 26
3.1.2 The invested energy H_i . . . 28
3.1.3 Influence of the electric breakdown . . . 28
3.2 Numerical results . . . 30
3.2.1 High ultimate stretch regime (HΛU): $\lambda_U = 3$ . . . 31
3.2.2 Moderate ultimate stretch regime (MΛU): $\lambda_U = 1.8$ . . . 32
3.3 A universal plot for plane-strain load-driven DEGs . . . 33
3.3.1 Electromechanical properties for the best energy and efficiency cycles 35
3.4 Plane-strain DEGs based on commercially available soft DEs . . . 36

4 Optimisation of an ideal DEG in equibiaxial loading mode 41
4.1 Constrained optimisation problem for equibiaxial loading mode . . . 42
4.1.1 The harvested energy H_g . . . 42
4.1.2 The invested energy H_i . . . 43
4.1.3 Influence of the electric breakdown . . . 44
4.2 Numerical results . . . 47
4.2.1 High ultimate stretch regime (HΛU): $\lambda_U = 3$ . . . 48
4.2.2 Moderate ultimate stretch regime (MΛU): $\lambda_U = 2.1$ and $\lambda_U = 1.8$. 49
4.2.3 Low ultimate stretch regime (LΛU): $\lambda_U = 1.4$ . . . 51
4.3 A universal plot for equibiaxial load-driven DEGs . . . 52
4.3.1 Electromechanical properties for the best energy and efficiency cycles 53
4.4 Equibiaxial DEGs based on commercially available soft DEs . . . 56
4.5 Benefits of ceramic filler addition . . . 59
4.5.1 Material *a*) . . . 62
4.5.2 Material *b*) . . . 65
4.5.3 Material *c*) . . . 66

5 Optimisation of an ideal DEG in out-of-plane loading mode 69
5.1 Governing equations and material modelling of the annular DE membrane 70
5.2 The load-driven harvesting cycle for an out-of-plane DEG . . . 75
5.3 Harvested energy, efficiency, and performance evaluation . . . 76
5.3.1 Influence of the prestretch . . . 79
5.3.2 Influence of the radius ratio . . . 82
5.3.3 Influence of the maximum applied load . . . 83
5.4 Comparison of different DEG materials and configurations . . . 85
5.4.1 Comparison of different DEG materials . . . 85
5.4.2 Comparison of different DEG configurations . . . 87

6 Viscoelastic DEG operating in an electric circuit for energy harvesting 89
6.1 A simple real harvesting circuit . . . 90
6.2 Calibration of the electro-viscoelastic model . . . 93
6.2.1 Calibration of the mechanical behaviour . . . 93
6.2.2 Calibration of the electrical behaviour . . . 95
6.3 Generator operating in the electrical circuit . . . 96
6.4 Equibiaxial loading . . . 99
6.4.1 Cycle characterisation of a viscoelastic DEG . . . 100
6.4.2 Efficiency analysis . . . 102

6.4.3 Failure envelope at regime conditions 106
6.5 Uniaxial loading 111

7 Conclusions 115

A Non-linear optimisation: Nelder-Mead method 119

B Constrained optimisation problem: Lagrange multiplier method 123

C Annular membrane solving procedure: numerical shooting method 127

Bibliography 129

List of Figures

1.1 Examples of DE energy harvesters: a) heel-strike generator tested by SRI international [10] and b) polymeric oscillating water column developed in the PolyWEC project [61]. 2

2.1 Reference and deformed configurations of a soft planar DE generator with undeformed dimensions $(l_0 \times l_0 \times h_0)$: as a result of the deformation, the current dimensions are $l_1 = l_0\lambda_1$, $l_2 = l_0\lambda_2$ and $h = h_0\lambda_3$. 5

2.2 The load-driven harvesting cycle plotted on the a) mechanical and b) electrical planes and c) illustration of the four strokes with a service battery at the right and a storage battery at the left; the illustrations in c) are referred to the initial states of each individual stroke. 15

2.3 Failure envelopes for a plane-strain loaded DEG on the electrical $\bar{\phi}$–$\bar{\omega}_0$ plane for increasing values of the electric breakdown strength ($\bar{E}_{eb} = 0.4, 0.6, 0.8, 1$) and of the ultimate stretch ($\lambda_U = 1.5, 2, 2.5, 3, 3.5$). 18

2.4 Failure envelopes at $\bar{E}_{eb} = 0.8$ and $\lambda_U = 3$ on the a) mechanical $\bar{S}_{11}$–λ and b) electrical $\bar{\phi}$–$\bar{\omega}_0$ planes for a plane-strain loaded DEG. 19

2.5 Failure envelopes for an equibiaxially loaded DEG on the electrical $\bar{\phi}$–$\bar{\omega}_0$ plane for increasing values of the electric breakdown strength ($\bar{E}_{eb} = 1.09, 1.2, 1.3, 1.5, 1.7$) and of the ultimate stretch ($\lambda_U = 1.5, 2, 2.5, 3, 3.5$). . 21

2.6 Failure envelopes at $\bar{E}_{eb} = 0.8$ and $\lambda_U = 3$ on the a) mechanical $\bar{S}$–λ and b) electrical $\bar{\phi}$–$\bar{\omega}_0$ planes for an equibiaxially loaded DEG. 21

3.1 Reference and deformed configurations of a soft planar DE generator with undeformed dimensions $(l_0 \times l_0 \times h_0)$ subjected to a plane-strain loading: as a result of the deformation, the current dimensions are $l_1 = l_0\lambda$, $l_2 = l_0$ and $h = h_0\lambda^{-1}$. 25

3.2 Region of admissible state for a plane-strain loaded DEG with $\bar{E}_{eb} = 0.8$, $\lambda^* = 1.667$ and $\hat{\omega}_0 = 2.828$ on the a) mechanical and b) electrical planes. . 29

3.3 Optimal cycles on the mechanical and electrical planes for $\lambda_U = 3$ and: a) $\bar{E}_{eb} = 0.6$ and b) $\bar{E}_{eb} \geq 0.8263$. 31

3.4 Optimal cycles on the mechanical and electrical planes for $\lambda_U = 1.8$ and $\bar{E}_{eb} \geq 0.6889$. 32

3.5 A universal plot for planar plane-strain load-driven DEGs. The abscissa and the ordinate of the plot correspond to the electromechanical limits of the film λ_U and $\bar{E}_{eb}$, respectively. The dark-blue curve divides the space of materials parameters into two sections, depending on the mode of failure at point D of the optimal harvesting cycle. Beyond the light-blue curve the electric breakdown becomes unimportant in the definition of the allowable state region. The dark-blue dashed curve is related to the analytical prediction (3.14). 33

3.6 Approximation of the cycle area through a rectangle whose height is equal to the potential difference $\delta\bar{\phi}$ among the loss of tension ($S_{22} = 0$) and the ultimate stretch λ_U curve. 34

3.7 Values of the electric breakdown strength E_{eb} [MV/m] as a function of the shear modulus μ and of the relative dielectric permittivity ϵ_r for the best performance in terms of: a) efficiency, $\lambda_U = 1.546$ (MΛU) and $\bar{E}_{eb} = 0.5929$, and b) energy, $\lambda_U = 3$ (HΛU) and $\bar{E}_{eb} = 0.8263$. 37

4.1 Reference and deformed configurations of a soft planar DE generator with undeformed dimensions ($l_0 \times l_0 \times h_0$) subjected to equibiaxial loading: as a result of the deformation, the current dimensions are $l = l_1 = l_2 = l_0\lambda$ and $h = h_0\lambda^{-2}$. 41

4.2 Region of admissible state for an equibiaxially loaded DEG with $\bar{E}_{eb} = 1.0912$, $\lambda^* = 1.259$, $\lambda^{**} = 1.739$, $\tilde{\omega}_0 = 15.642$ and $\hat{\omega}_0 = 26.981$ on the a) mechanical and b) electrical planes. 45

4.3 Optimal cycles for $\lambda_U = 3$ and: a) $\bar{E}_{eb} = 0.9$, b) $\bar{E}_{eb} = 1.038$, c) $\bar{E}_{eb} = 1.091$, and d) $\bar{E}_{eb} \geq 1.396$. 48

4.4 Optimal cycles for $\lambda_U = 2.1$ and: a) $\bar{E}_{eb} < 1.091$ and b) $\bar{E}_{eb} \geq 1.091$. . . . 50

4.5 Optimal cycles for $\lambda_U = 1.8$ and: a) $\bar{E}_{eb} < 1.091$ and b) $\bar{E}_{eb} \geq 1.091$. . . . 50

4.6 A universal plot for planar equibiaxial load-driven DEGs. The abscissa and the ordinate of the plot correspond to the electromechanical limits of the film λ_U and $\bar{E}_{eb}$, respectively. The dark-blue and orange curves divide the space of materials parameters into sections depending on the mode of failure at point D of the optimal harvesting cycle. Along the solid-dotted dark-blue curve we distinguish between the high, the moderate and the low ultimate stretch regions. Uniquely below the dark-blue curve, the failure depends on the electrical breakdown limit. Along the solid light-blue curve we distinguish between Case a and Case b, so that above this curve the electrical breakdown does not participate in the definition of the allowable state region. 52

4.7 Values of the electric breakdown strength E_{eb} [MV/m] as a function of the shear modulus μ and of the relative dielectric permittivity ϵ_r for the best performance in terms of: a) efficiency, for $\lambda_U = 1.563$ (MΛU) and $\bar{E}_{eb} = 1.091$ and b) energy, for $\lambda_U = 3$ (HΛU) and $\bar{E}_{eb} = 1.396$. 55

4.8 Universal design curve for planar equibiaxial load-driven DEGs already introduced in Fig. 4.6: electromechanical characteristics of the three composites, black shapes, and of their PDMS matrices, white shapes. 62

4.9 Optimal cycle for (I) the pure PDMS and (II) the PDMS–%10PMN–PT composite, on the A) mechanical and B) electrical planes, in the case $\lambda_U = 1.8$. With respect to the EB influence on the optimal cycle, both materials appertain to subregion (iii) (cf. e.g. Fig. 4.8). With respect to the EB influence on the admissible state region, the pure PDMS is related to Case b, whereas the composite pertains to Case a. 64

4.10 Optimal cycle for (I) the pure PDMS and (II) the PDMS–%10PMN–PT composite, on the A) mechanical and B) electrical planes, in the case $\lambda_U = 3.0$. With respect to the EB influence on the optimal cycle, the pure PDMS lies on subregion (vii), while the composite belongs to subregion (vi) (cf. e.g. Fig. 4.8). With respect to the EB influence on the admissible state region, the pure PDMS is related to Case b, instead the composite pertains to Case a. 64

5.1 Sketch of the periodic four-phase cycle for the investigated electroactive membrane generator (phases IV and I coincide): a) membrane configurations; b) mechanical force ($\mathcal{F}$)–out-of-plane displacement (u) plane; c) multi-membrane device subjected to a total force $\mathcal{F}_{tot}$. 71

5.2 Configurations of the annular membrane generator: a) undeformed, b) prestretched and c) deformed. 72

5.3 The investigated harvesting cycle: a) illustration of the four strokes along the I–II–I path with a service battery at the right and a storage battery at the left b) plot of the cycle on the electrical Q–ϕ plane and on the mechanical $\mathcal{F}$–u plane. The measure of the area of the cycle, on both planes, is equal to the modulus of the harvested energy, $|H_g|$. The light-grey shaded areas represent the electrical and the mechanical work invested into the conversion process. 77

5.4 Influence of the prestretch on the performance of a generator with $r_0^e/r_0^i = 2$. Plot on the electrical ϕ–Q plane of the optimal cycle for different prestretch values, namely $\lambda_{pre} = 1$, 1.05, 1.1, 1.25, 1.5 and 2, and $\mathcal{F}_{max} = 90$ N. The relevant failure mode is indicated below the prestretch label. . 79

5.5 Influence of the prestretch λ_{pre} on the performance of a generator with $r_0^e/r_0^i = 2$, $\mathcal{F}_{max} = 90$ N: a) gained energy per unit mass $\hat{H}_g$ and b) efficiency η. The failure mode in the relevant prestretch range is reported below the horizontal axis. 80

5.6 Influence of the prestretch λ_{pre} on the performance of a generator with $r_0^e/r_0^i = 2$, $\mathcal{F}_{max} = 90$ N: a) maximum stretch λ_{max} and b) maximum current electric field E_{max}. The failure mode in the relevant prestretch range is reported below the horizontal axis. 81

5.7 Influence of the radius ratio r_0^e/r_0^i on the performance of the generator for different prestretches: a) gained energy per unit mass $\hat{H}_g$ and b) efficiency η. 83

5.8 Influence of the maximum applied load $\mathcal{F}_{max}$ on a) the efficiency η and b) the gained energy per unit mass $\hat{H}_g$ of a generator with $r_0^e/r_0^i = 2$. A dot at the end of a curve indicates that one stretch in the membrane has reached the ultimate value $\lambda_{max} = \lambda_U = 4$ (in all cases $\lambda_1 = \lambda_{max}$). 84

6.1 Soft dielectric elastomer generator: a) reference configuration and b) scheme of the equivalent circuit diagram. 90

6.2 Scheme of the electrical circuit in which the dielectric elastomer generator operates. 91

6.3 Viscoelastic behaviour of VHB-4910: stress response at different strain rates as obtained from parameter identification. Dots: experimental data based on experiments by Tagarielli et al. [58]; solid lines: simulated data. 95

6.4 Dielectric permittivity of VHB-4910 at different equibiaxial stretches for two representative frequencies $\bar{f}$ as obtained from parameter identification based on experiments by Tagarielli et al. [58]. 96

6.5 Plot of loading cycles of a DEG a) in the mechanical S–λ and b) in the electrical $\phi_C + \phi_{R_s}$–Q planes at different initial times t_i, namely 10, 50, 100 and 200 seconds. Model VC, $\lambda_o = 3.0$, $\mathit{\Lambda} = 0.50$, $f = 0.1$ Hz, $R_{ext} = 0.1$ GΩ. 100

6.6 Plot of loading cycles of a DEG a) in the mechanical S–λ and b) in the electrical $\phi_C + \phi_{R_s}$–Q planes at different initial times t_i, namely 10, 50, 100 and 200 seconds. Model VC, $\lambda_o = 3.0$, $\varLambda = 0.50$, $f = 1$ Hz, $R_{ext} = 0.1$ GΩ. . . . 101

6.7 Plot of the viscous dissipation $\mathcal{D}_v$ and the leakage dissipation $\mathcal{D}_{R_i}$ at different frequencies f. Model VC, $\lambda_o = 3.0$, $\varLambda = 0.50$, $R_{ext} = 0.1$ GΩ. . . 101

6.8 Plot of the efficiency $\eta(R_{ext}, f)$ for the three different material models: a) hyperelastic, HYP, b) viscoelastic, VC, and c) electrostrictive viscoelastic, VE. Equi-biaxial loading conditions with $\lambda_o = 3.0$; $\varLambda = 0.50$, $\varLambda = 0.25$ and $\varLambda = 0.10$. . . . 104

6.9 Plot of the efficiency η versus a) frequency f at $R_{ext} = 1$ GΩ, and b) external resistance R_{ext} at $f = 1$ Hz. Equi-biaxial loading conditions with $\lambda_o = 3.0$; $\varLambda = 0.50,\ 0.25,\ 0.10$. Dashed, continuous and dotted lines are referred respectively to HYP, VC and VE models. . . . 105

6.10 Plot of the efficiency η versus frequency f for two values of the mean value of the oscillation stretch $\lambda_o = 1.8$ and $\lambda_o = 3$. Equi-biaxial loading conditions with $R_{ext} = 1$ GΩ, VC model. . . . 106

6.11 Plot on the electrical $\bar{\phi}$–$\bar{\omega}_0$ plane of the failure envelope for different values of the mean stretch λ_o. Solid lines are referred to the VC model, dashed lines to the HYP model. . . . 108

6.12 Plot on the electrical $\bar{\phi}$–$\bar{\omega}_0$ plane of the a) loss of tensile state and b) electromechanical instability curves for different values of the mean stretch, namely $\lambda_o = 1.8, 3, 4$. Solid lines are referred to the VC model, dashed lines to the HYP model. . . . 109

6.13 Plot of the cycle on the electrical plane for different values of the product fR_{ext}, at $\lambda_o = 3$ and $\varLambda = 0.695$. The failure curves are represented by dashed black lines for the HYP model and by solid black lines for the VC model. . . . 110

6.14 Plot of the maximal oscillation amplitude $\varLambda_{max}$ as a function of the product fR_{ext} for $\lambda_o = 3$. . . . 111

6.15 Plot of the efficiency $\eta(R_{ext}, f)$ for an external resistance R_{ext} =1 GΩ and $\lambda_o = 3.0$, $\varLambda = 0.50$ and $\varLambda = 0.25$. Dashed, continuous and dotted lines are referred respectively to HYP, VC and VE models. . . . 112

A.1 Nelder-Mead method: reflection of the simplex. . . . 121

A.2 Nelder-Mead method: expansion of the simplex. . . . 121

A.3 Nelder-Mead method: contraction of the simplex a) outside and b) inside. 121

A.4 Nelder-Mead method: shrinkage of the simplex. . . . 122

List of Tables

3.1 Classification of the optimal cycles for plane-strain load-driven DEGs, according to the relevance of the electric breakdown E_{eb} on the failure at D, cf. Fig. 3.5. 30

3.2 Relevant numerical values for optimal cycles associated with a DEG with $\lambda_U = 3$ and different values of $\bar{E}_{eb}$. 32

3.3 Relevant numerical values for optimal cycles associated with a DEG with $\lambda_U = 1.8$ and different values of $\bar{E}_{eb}$. 33

3.4 Electromechanical properties ensuring the best performance in terms of efficiency and harvested energy for a plane-strain load-driven DEG. 35

3.5 Physical properties assumed for the elastic dielectrics. 38

3.6 The harvested energy-density μH_g, activation electric potential per unit referential thickness $\Delta\phi/h_0$ and material classification M-C, determined for the optimal cycles according to the dielectric strength limits and the maximal stretch ratios λ_C determined for the maximum stresses $S_{\max}$. . . 38

4.1 Classification of the optimal cycles for equibiaxial load-driven DEGs, according to the relevance of the electric breakdown E_{eb} on the failure at D, cf. Fig. 4.6. 47

4.2 Relevant numerical values for optimal cycles associated with a DEG with $\lambda_U = 3$ and different values of $\bar{E}_{eb}$. 49

4.3 Relevant numerical values for optimal cycles associated with a DEG with $\lambda_U = 2.1$ and different values of $\bar{E}_{eb}$. 51

4.4 Relevant numerical values for optimal cycles associated with a DEG with $\lambda_U = 1.8$ and different values of $\bar{E}_{eb}$. 51

4.5 Relevant numerical values for optimal cycles associated with a DEG with $\lambda_U = 1.4$ and for different values of $\bar{E}_{eb}$. 52

4.6 Electromechanical properties ensuring the best performance in terms of efficiency and harvested energy for an equibiaxial load-driven DEG. . . . 54

4.7 Physical properties and electric breakdown parameters for the rigid electrode configuration. 56

4.8 Electric breakdown data for the two elastomers at different ultimate stretches λ_U, see [60]. 56

4.9 Data for DEGs with two MΛU elastomers and two configurations: $\hat{H}_g = \mu H_g/\rho$, harvested energy density per unit mass, $\Delta\phi/h_0$, activation electric potential per unit referential thickness, η, efficiency, M-C, material classification according to Fig. 4.6, $\hat{H}_{max} = \mu H_{max}/\rho$, theoretically achievable energy, ζ, effectiveness; n, number of 1 mm thick layers required to sustain 1 kN at λ_U, $n\tilde{H}_g$, total harvested energy by the multi-membrane DEG. . . 57

4.10 Data for DEGs with two HΛU elastomers and two configurations: $\hat{H}_g = \mu H_g/\rho$, harvested energy density per unit mass, $\Delta\phi/h_0$, activation electric potential per unit referential thickness, η, efficiency, M-C, material classification according to Fig. 4.6, $\hat{H}_{max} = \mu H_{max}/\rho$, theoretically achievable energy, ζ, effectiveness; n, number of 1 mm thick layers required to sustain 1 kN at λ_U, $n\tilde{H}_g$, total harvested energy by the multi-membrane DEG. . . 58
4.11 Sets of parameters for the ceramic–polymer composites analyzed. 60
4.12 Sets of parameters for the three PDMS involved in the ceramic–polymer composites. 61
4.13 Material classification M-C, according to Fig. 4.8, and generated energy-density per unit shear modulus H_g for the selected harvesting cycles for the composite material *a*) and its matrix. 63
4.14 Material classification M-C according to Fig. 4.8, generated energy per unit volume μH_g, required voltage $\Delta\phi$ (inside square brackets) and percentage gain for the selected harvesting cycles allowed by the composite material *a*) over its matrix. 63
4.15 Material classification M-C, according to Fig. 4.8, and generated energy-density per unit shear modulus H_g for the selected harvesting cycles for the composite material *b*) and its matrix. 65
4.16 Material classification M-C according to Fig. 4.8, generated energy per unit volume μH_g and per unit mass $\hat{H}_g$, required voltage $\Delta\phi$ for the selected harvesting cycles (inside square brackets) and percentage gain allowed by the composite material *b*) over its matrix. 66
4.17 Material classification M-C, according to Fig. 4.8, and generated energy-density per unit shear modulus H_g for the selected harvesting cycles for the composite material *c*) and its matrix. 67
4.18 Material classification M-C according to Fig. 4.8, generated energy per unit volume μH_g, required voltage $\Delta\phi$ for the selected harvesting cycles (inside square brackets) and percentage gain allowed by the composite material *c*) over its matrix. 67

5.1 Electromechanical properties of VHB-4910. 78
5.2 Influence of the prestretch λ_{pre} on the performance of a generator with $r_0^e/r_0^i = 2$. Gained energy per unit mass $\hat{H}_g$, efficiency η, supplied voltage $\Delta\phi$ and obtained voltage jump $\phi^D - \phi^C$ are reported. For each examined prestretch the failure mode experienced by the device is listed. Furthermore, the improvement in the gained energy $\delta\hat{H}_g$ and in the efficiency $\delta\eta$ with respect to the unprestretched case ($\lambda_{pre} = 1$) are quantified. 82
5.3 Influence of the radius ratio on the generator performance: internal radius r_0^i ($r_0^e = 500$ mm), and maximum applied load $\mathcal{F}_{max}$. For the best performance of the generator, the prestretch λ_{pre}, the gained energy per unit mass $\hat{H}_g$, the efficiency η, the applied voltage $\Delta\phi$ and the obtained voltage jump $\phi^D - \phi^C$ are reported. 83
5.4 Electromechanical properties of the natural rubber ZruElast A1040 [31]. . 85

5.5a Performance comparison of devices made up of two different materials working at maximum efficiency. Left-hand and central parts of the table refer to the behaviour of a single membrane. The right-hand side of the table reports the performance of multi-membrane systems subjected to a total maximum force $\mathcal{F}_{tot} = 34$ kN: n, number of layers required; $n|H_g|$, total energy harvested. 86
5.5b Performance comparison of devices made up of two different materials working at maximum energy. Left-hand and central parts of the table refer to the behaviour of a single membrane. The right-hand side of the table reports the performance of multi-membrane systems subjected to a total maximum force $\mathcal{F}_{tot} = 34$ kN: n, number of layers required; $n|H_g|$, total energy harvested. 86
5.6a Performance comparison at $\lambda_{max} = 2.4$ for different prototype generator configurations, acrylic material properties (VHB-4910) 87
5.6b Performance comparison at $S_{max} = 70$ kPa for different prototype generator configurations, acrylic material properties (VHB-4910) 87

6.1 Mechanical material parameters. 95
6.2 Electrical and coupling material parameters. 96
6.3 Energy produced by the generator and mechanical work invested at two different frequencies, $f = 0.1$ Hz and $f = 1$ Hz, computed after 200 s for the three material models considered: $\lambda_o = 3$, $\Lambda = 0.50$, $\epsilon_r^0 = 6.4$, $R_{ext} = 0.1$ GΩ. The reference volume V_0 is given by $l_0^2\, h_0$. 102
6.4 Maximal oscillation amplitude Λ_{max} achievable in an equibiaxial test without inducing in-plane negative stresses. Model VC, $R_{ext} = 0.1$ GΩ, $f = 1$ Hz. 102
6.5 Energy produced by the generator and mechanical work invested for the three selected amplitudes $\Lambda = 0.10$, $\Lambda = 0.25$ and $\Lambda = 0.50$, computed after 200 s for the VC model: $\lambda_o = 3$, $f = 1$ Hz, $\epsilon_r^0 = 6.4$, $R_{ext} = 0.1$ GΩ. The reference volume V_0 is given by $l_0^2\, h_0$. 103

Abbreviations

DE	**D**ielectric **E**lastomer
DEA	**D**ielectric **E**lastomer **A**ctuator
DEG	**D**ielectric **E**lastomer **G**enerator
EAP	**E**lectro **A**ctive **P**olymer

CCTO	calcium copper titanate $\mathbf{C}a\mathbf{C}u_3\mathbf{T}i_4\mathbf{O}_{12}$
PDMS	**P**oly–**D**i**M**ethyl–**S**iloxane
PMN–PT	lead magnesium niobate $\mathbf{P}b(\mathbf{M}g_{1/3}\mathbf{N}b_{2/3})O_3$ – lead titanate $\mathbf{P}b\mathbf{T}iO_3$
PZT	lead zirconate–titanate $\mathbf{P}b[\mathbf{Z}r_{1-x}\mathbf{T}i_x]O_3$

Physical Constants

Vacuum Permittivity $\epsilon_0 = 8.854\ 187\ 817 \times 10^{-12}\ \mathrm{Fm^{-1}}$

Elementary Charge $q_e = 1.602\ 176\ 53 \times 10^{-19}\ \mathrm{C}$

Symbols

$\tilde{H}_{max}$	theoretically achievable energy	[J]
$\tilde{H}_g$	harvested energy	[J]
$\tilde{H}_i$	invested energy	[J]
H_{max}	theoretically achievable energy-density per unit shear modulus	dimensionless
H_g	harvested energy-density per unit shear modulus	dimensionless
H_i	invested energy-density per unit shear modulus	dimensionless
$\hat{H}_g$	harvested energy per unit mass	[J kg^{-1}]
$\hat{H}_i$	invested energy per unit mass	[J kg^{-1}]
$\boldsymbol{P}$	current polarisation	[C m^{-2}]
$\boldsymbol{E}$	current electric field	[V m^{-1}]
$\boldsymbol{E}^0$	nominal electric field	[V m^{-1}]
$\boldsymbol{D}$	current electric displacement	[C m^{-2}]
$\boldsymbol{D}^0$	nominal electric displacement	[C m^{-2}]
Q	electric charge	[C]
i	electric current	[A]
E_{eb}	current electric breakdown strength	[V m^{-1}]
$\boldsymbol{X}$	material position vector	
$\boldsymbol{x}$	spatial position vector	
$\boldsymbol{F}$	deformation gradient	dimensionless
$\boldsymbol{S}$	Piola stress	[Pa]
$\boldsymbol{f}_e$	electrical body force	[N m^{-3}]
$\boldsymbol{f}$	mechanical body force	[N m^{-3}]
$\boldsymbol{C}$	Cauchy–Green tensor	
$\boldsymbol{C}_{v\alpha}$	internal variable tensor	
$\boldsymbol{\mathcal{F}}$	force vector	[N]

$\mathcal{T}$	temperature	[K]
f	frequency	[Hz]
T	period	[s]
W	strain-energy function based on $\boldsymbol{E}^0$, Gibbs potential	
$\mathcal{W}$	strain-energy function based on $\boldsymbol{D}^0$, Helmholtz potential	
R_s	electric resistance	[Ω]
R_i	electric resistance	[Ω]
R_{ext}	electric resistance	[Ω]
C	electric capacitance	[F]
P_{in}	input power	[W]
P_{out}	output power	[W]
E_{in}	input electrical energy	[J]
E_{out}	output electrical energy	[J]
ΔE	energy produced by the generator	[J]
l_0	nominal side length	[m]
l	current side length	[m]
h_0	nominal thickness	[m]
h	current thickness	[m]
r_0	nominal radius	[m]
r	current radius	[m]
u	maximum transverse displacement	[m]
r_0^i	nominal inner radius	[m]
r_0^e	nominal external radius	[m]
A_0	reference undeformed area	[m^2]
A	current area	[m^2]
V_0	reference undeformed volume	[m^3]
V	current volume	[m^3]
J	volume ratio	dimensionless

μ	shear modulus	[Pa]
ρ_0	density in the undeformed configuration	[kg m^{-3}]
ρ	density in the current configuration	[kg m^{-3}]

ϵ	permittivity	[F m^{-1}]
β_α	proportionality factor among the shear modulus of the α Maxwell element and the long term one	dimensionless
$\dot{\varGamma}_\alpha$	material parameter, inverse of the viscosity of the α Maxwell element	[s^{-1} Pa^{-1}]
$\varPhi(\boldsymbol{X})$	electrostatic potential	
ω_0	referential charge density	[C m^{-2}]
ϕ	voltage	[V]
$\bar{\omega}_0$	referential charge density	dimensionless
$\bar{\phi}$	voltage	dimensionless
η	efficiency	dimensionless
ζ	effectiveness	dimensionless
λ	principal stretch	dimensionless
λ_{pre}	prestretch	dimensionless
λ_v	viscous principal stretch	dimensionless
λ_o	oscillation mean value	dimensionless
$\varLambda$	oscillation amplitude	dimensionless
ψ	angular frequency	[rad s^{-1}]
θ	slope of the deformed membrane	[rad]

In memory of Prof. Federico di Varmo

Chapter 1

Introduction

In recent years, the urgency of energy from renewable resource has become increasingly crucial, thereby giving new impulse to the development of new concepts and modern techniques. Among the various energy harvesting technologies, a particularly promising one is based on soft *dielectric elastomers* (DEs) [1, 9, 10, 38, 44]. Being reliable, quick responsive, light, cheap and involving a few moving parts, such electro-mechanical transducers are suitable for different applications, allowing energy extraction from sea waves, wind gusts, human gait and other natural sources of mechanical work, see for example Figs. 1.1a and 1.1b.

A *Dielectric Elastomer Generator* (DEG) is basically conceived as a highly stretchable parallel-plate capacitor with variable capacitance, able to produce electrical energy converting the mechanical work done by an external oscillating load. This device is simply made up of a soft DE membrane, whose upper and lower surfaces are treated so as to act like compliant electrodes. The capacitance depends on the current geometry of the dielectric film, therefore it changes as a consequence of the stretch and release of the membrane induced by its interaction with the external environment. This significant capacitance variability can be exploited to extract electrical energy through a four-stroke cycle where (i) an initial, relatively slow, stretching of the elastomeric film induced by the rising force is followed by (ii) a fast charging phase. Then, (iii) the capacitor is relaxed due to the slow release of the load and (iv), finally, the charge is harvested at high electric potential and at low force.

Different configurations and harvesting cycles have been proposed in the literature essentially involving three charging–discharging strategies, distinguished by the electrical variable - among electric field, charge and voltage - to be kept constant along both the stretching and the contracting phases induced by the mechanical force [39]. In this work, differently from others [25, 30, 36], we assume that the mechanical load and the electric

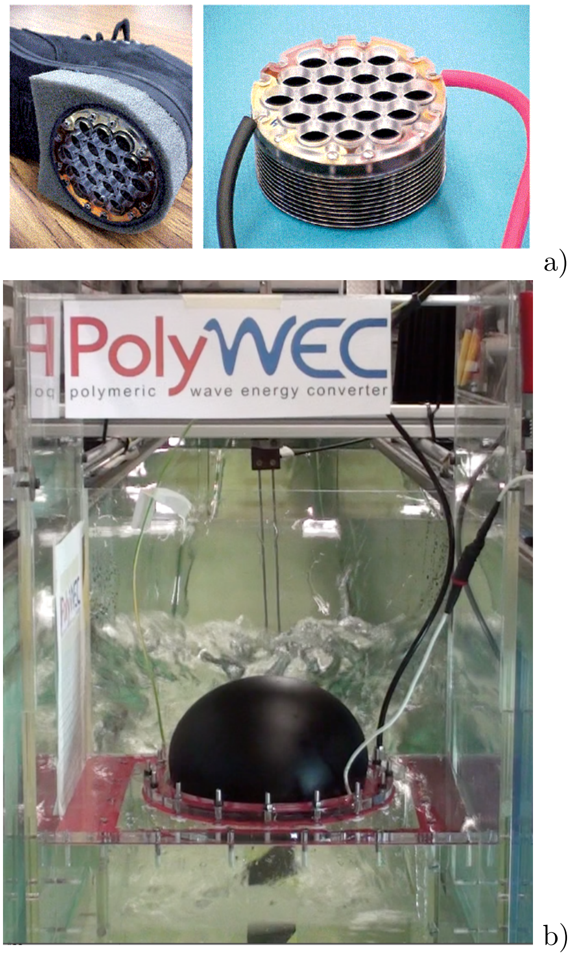

FIGURE 1.1: Examples of DE energy harvesters: a) heel-strike generator tested by SRI international [10] and b) polymeric oscillating water column developed in the PolyWEC project [61].

charge are alternately held constant during the cycle. This means that the stretching and contracting phases occur at constant charge, for example when the system is electrically isolated (open-circuit condition), while charging and harvesting phases take place at stationarity points of the loading function.

The amount of extracted energy is limited due to possible failures of the dielectric membrane, which are, in the most general circumstances, electric breakdown, material rupture, buckling-like instabilities, due to loss of the tensile stress state, and electromechanical instability [5, 49]. These failure mechanisms determine the allowable state region for the generator [37].

A few recent papers are dedicated to the analysis of the performance of DEGs and to the identification of the more profitable electromechanical loading strategies allowing the maximisation of the energy gain. Kaltseis et al. [30] introduced a method to measure the produced energy and the efficiency of a balloon-like generator. Huang et al. [25, 26]

showed that significant improvements in the generated energy density can be achieved using an equibiaxial mechanical loading configuration accounting also for viscoelasticity. Vertechy et al. [61] proposed a polymer-based oscillating-water-column energy converter (Fig. 1.1b).

This monograph is dedicated to a systematic investigation of the performance optimisation of DEGs in the framework of the nonlinear theory of electro-elasticity. The main goal of this research is the identification, by means of a numerical analysis, of those cycles able to produce the maximum energy fulfilling the constraints associated with the various failure modes.

After recalling, in Chap. 2, the basic elements of continuum electro-mechanics and the working principles of DEGs, the optimisation procedure for a planar load-driven soft DEG is presented, assuming isotropic hyperelasticity and ideal dielectric behaviour, for plane-strain (Chap. 3) and equibiaxial (Chap. 4) loading modes. In order to identify the best cycle that complies with the limits dictated by the failure envelope, a constrained optimisation problem is formulated and the generator performance is estimated on the basis of both the energy extracted during a cycle and the efficiency, i.e. the ratio of the harvested energy on the total invested energy. For the two loading cases examined, in Chaps. 3 and 4, numerical results for different stretch regimes and performance comparisons for various soft DEs commercially available are presented.

The chosen loading modes are justified on the grounds that plane-strain condition simulates the effect of transverse constraint due to stiff fibres [40] or a supporting frame, while equibiaxial condition can be produced by an external agent in a mechanism involving the expansion of a dielectric balloon due to internal pressure [12, 48, 53].

In addition to the simple parallel-plate configuration, an annular layout has been taken into consideration in Chap. 5. In this case, the generator is made up of a circular membrane constrained at the boundary by a rigid ring and at the centre by a rigid plate, on which an external force is applied. Due to the loading, the membrane deforms non-homogeneously out-of-plane. The deformation undergone by the annular membrane has been already exploited for the realisation of actuators [4, 24], but it is also particularly interesting for sea-wave energy harvesting. Actually, the annular membrane can constitute the basic power take-off element of a floating harvesting device, constituted by a Stewart platform. Moreover, along a complete oscillation of the mechanical load, the annular generator can perform a double electromechanical cycle, as deformation can take place on both sides of the membrane. In the first part of Chap. 5, the influence of the prestretch and of the radius ratio on the DEG performance is investigated. Then, in the final part, performance comparisons are provided. Here, annular DE membranes with different electromechanical properties are investigated and various DEG geometries, under similar stress/stretch conditions, are compared.

Dielectric elastomers, as all polymers, are affected by time-dependent effects, hence the conservative hypothesis appears to be not completely realistic. Indeed, a predicting model for soft DEGs must include an accurate model of the electro-mechanical behaviour of the elastomer filling, the variable capacitor and of the electrical circuit connecting all the device components. To this end, the ideality assumption of the material and of the cycle has to be removed. Hence, in Chap. 6, a complete framework for a reliable simulation of soft energy harvesters is presented for a soft electro-viscoelastic DEG, mechanically excited by a periodic stretch and integrated in an electrical circuit for energy harvesting.

Conclusions are finally drawn in Chap. 7.

Chapter 2

Dielectric elastomer generators: theory

A dielectric elastomer generator is an electro-mechanical transducer able to convert mechanical to electric energy. The basic idea behind its operating principle consists in varying its capacitance with the deformation, hence this device can be regarded as a highly deformable soft capacitor.

In the simplest framework, a three-dimensional soft dielectric elastomer generator is made up of a dielectric elastomer membrane whose surfaces are treated so as to act like compliant electrodes and whose initial volume is $V_0 = l_0 \times l_0 \times h_0$ in the reference undeformed configuration. Essentially, this DEG is a parallel-plate soft capacitor.

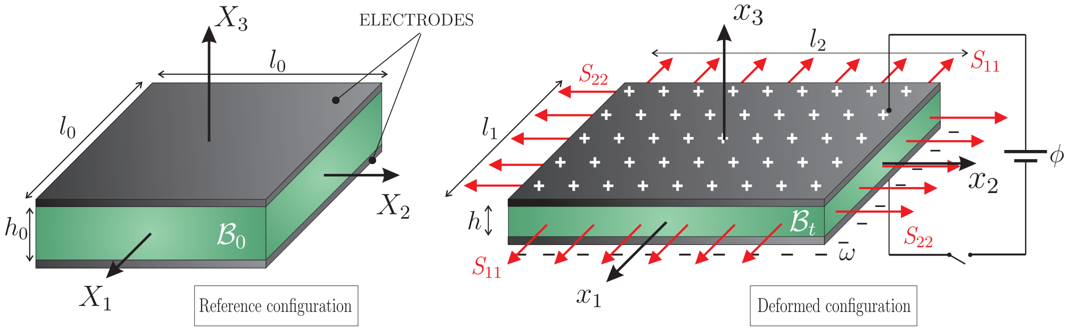

Figure 2.1: Reference and deformed configurations of a soft planar DE generator with undeformed dimensions ($l_0 \times l_0 \times h_0$): as a result of the deformation, the current dimensions are $l_1 = l_0\lambda_1$, $l_2 = l_0\lambda_2$ and $h = h_0\lambda_3$.

We assume that the dielectric membrane is homogeneous, isotropic and incompressible. The membrane is stretched from the undeformed to the current configuration by a combination of (i) a mechanical in-plane force $\mathcal{F}$ induced by the environment, which is the primary source of energy invested into the system, and (ii) an electric field generated by a voltage ϕ applied between the stretchable electrodes. We note that an alternative way to electrically excite the deformation is by depositing electrical charge on the opposite surfaces of the specimen [33]. However, in this work we do not consider this alternative, since, from a practical viewpoint, it is more convenient to impose the required electric potential between the electrodes.

Neglecting fringing effects and assuming isotropy, the electromechanical deformation undergone by the membrane is homogeneous and can be represented by the deformation gradient $\boldsymbol{F} = \mathrm{diag}(\lambda_1, \lambda_2, \lambda_3)$, where λ_1, λ_2 and λ_3 are the principal stretch ratios along the directions ($\boldsymbol{e}_1$, $\boldsymbol{e}_2$, $\boldsymbol{e}_3$), see the coordinate systems in Fig. 2.1. Outside the capacitor the electric field vanishes, and the uniform electric field induced by the applied electric potential inside the membrane has only a component along $\boldsymbol{e}_3$, namely $\boldsymbol{E} = [0, 0, E]^T$.

2.1 Theoretical background: kinematics and governing equations

For the motion of the material body considered, we assume the existence of a sufficiently smooth mapping $\boldsymbol{\varphi}(\boldsymbol{X}, t)$ transforming the position vector $\boldsymbol{X}$ of a material particle in the undeformed configuration $\mathcal{B}_0$ to its spatial position $\boldsymbol{x} = \boldsymbol{\varphi}(\boldsymbol{X}, t)$ in the current configuration $\mathcal{B}_t$ at time t (see e.g. Fig. 2.1). Hence, the deformation gradient tensor is given by $\boldsymbol{F} = \mathrm{Grad}\boldsymbol{\varphi}$, where the gradient is taken with respect to the reference configuration $\mathcal{B}_0$. The local volume ratio is the Jacobian of the deformation gradient tensor $J = \det \boldsymbol{F}$ with $J = 1$ for incompressible materials. The right Cauchy-Green tensor is defined by $\boldsymbol{C} = \boldsymbol{F}^T \boldsymbol{F}$ and, thus, we formally introduce here the stretches λ_1, λ_2, λ_3, as the square roots of the eigenvalues of $\boldsymbol{C}$ such that $J = \lambda_1 \, \lambda_2 \, \lambda_3$.

The quantities of interest to define the current electrostatic state of the dielectric are the electric field $\boldsymbol{E}$, the electric displacements $\boldsymbol{D}$ and the polarisation $\boldsymbol{P}$ in $\mathcal{B}_t$, linked by the relation

$$\boldsymbol{D} = \epsilon_o \, \boldsymbol{E} + \boldsymbol{P},$$

where ϵ_0 is the dielectric permittivity of vacuum ($\epsilon_0 = 8.854$ pF/m).

Electromagnetic interactions are governed by Maxwell's equations. We assume throughout this work that (i) the hypotheses of electrostatics hold true and that (ii) free currents and free charges are absent. Therefore, Maxwell's equations in local form with respect to the current configuration $\mathcal{B}_t$ reduce to

$$\mathrm{curl}\boldsymbol{E} = \boldsymbol{0}\,, \qquad \mathrm{div}\boldsymbol{D} = 0\,, \tag{2.1}$$

or with respect to the reference configuration $\mathcal{B}_0$ to

$$\mathrm{Curl}\boldsymbol{E}^0 = \boldsymbol{0}\,, \qquad \mathrm{Div}\boldsymbol{D}^0 = 0\,, \tag{2.2}$$

where the following nominal fields

$$\boldsymbol{E}^0 = \boldsymbol{F}^T\boldsymbol{E}\,, \qquad \boldsymbol{D}^0 = J\boldsymbol{F}^{-1}\boldsymbol{D}\,, \tag{2.3}$$

are naturally introduced. See [5] for the exact derivation.

The notation used in Eqs. (2.1) and (2.2) is such that the uppercase letters indicate operators acting on $\mathcal{B}_0$, e.g. Grad, Div, Curl, whereas lowercase letters refer to operators defined in the configuration $\mathcal{B}_t$, e.g. grad, div, curl. Eq. $(2.2)_1$ implies that the electric field is conservative, i.e.

$$\boldsymbol{E}^0(\boldsymbol{X}) = -\mathrm{Grad}\mathit{\Phi}(\boldsymbol{X})\,, \tag{2.4}$$

where $\mathit{\Phi}(\boldsymbol{X})$ is the electrostatic potential. At the boundary $\partial\mathcal{B}_0$, the electric field and the electric displacement must fulfil the jump conditions

$$\boldsymbol{N}^0 \times [\![\boldsymbol{E}^0]\!] = \boldsymbol{0}\,, \qquad [\![\boldsymbol{D}^0]\!] \cdot \boldsymbol{N}^0 = -\omega_0\,, \tag{2.5}$$

where ω_0 is the charge density per unit reference electrode surface, $[\![f]\!] = f^a - f^b$ is the jump operator and where $\boldsymbol{N}^0$ denotes the outward referential unit normal vector, pointing from a towards b.

Considering the electric field uniform, as for the parallel-plate DEG sketched in Fig. 2.1, the nominal electric field can be expressed as $E^0 = \phi/h_0$ with $\phi = |\Delta\mathit{\Phi}|$ representing the voltage between the electrodes and h_0 being the reference thickness of the film. The electric field is similarly defined as $E = \phi/h$, where the current thickness h is given by $h = h_0\lambda_3$. The nominal charge density ω_0 can analogously be referred to its current counterpart ω given the charge $Q = \omega A = \omega_0 A_0$, where the current area of the film surfaces A is related to the area in the reference configuration A_0 as $A = A_0\lambda_1\lambda_2$, therefore, $\omega = \omega_0\lambda_1\lambda_2$. For the planar capacitor, Eq. $(2.5)_2$ and Eq. $(2.3)_2$ show that ω and ω_0 correspond to the absolute values of the current electric displacement D and of the nominal electric displacement D^0, respectively.

In the quasi-static case, the local form of the balance of linear momentum in $\mathcal{B}_t$ corresponds to

$$\mathrm{div}\boldsymbol{\sigma} + \boldsymbol{f}_e + \rho\boldsymbol{f} = \boldsymbol{0}\,, \tag{2.6}$$

where $\boldsymbol{\sigma}$ is the Cauchy stress tensor, ρ is the current mass density of the body, $\boldsymbol{f}$ is the mechanical body force and $\boldsymbol{f}_e$ is the electric body force per unit volume [7, 15]. The inertia term is neglected in both rate-independent and rate-dependent quasi-static cases, since its contribution is negligible for the frequency range investigated in this work, as will be explained later in Chap. 6. For the problem at hand, the electric body force can be specified as follows

$$\boldsymbol{f}_e = \mathrm{grad}\boldsymbol{E}\boldsymbol{P}\,.$$

Moreover, the Cauchy stress tensor $\boldsymbol{\sigma}$ is generally non-symmetric, whereas the total stress tensor

$$\boldsymbol{\tau} = \boldsymbol{\sigma} + \boldsymbol{E} \otimes \boldsymbol{D} - \frac{1}{2}\epsilon_0[\boldsymbol{E} \cdot \boldsymbol{E}]\boldsymbol{I}\,,$$

as introduced in e.g. [15, 27, 43, 45], turns out to be symmetric. The second-order identity tensor is denoted by $\boldsymbol{I}$. In this way, it is possible to rewrite the balance of linear momentum as

$$\mathrm{div}\boldsymbol{\tau} + \rho\boldsymbol{f} = \boldsymbol{0}\,.$$

Note that the form of the electric body force $\boldsymbol{f}_e$ is not the only possible one, since the choice of other sets of the electrical and mechanical variables can fit the general theory based on the total stress, see e.g. [8].

The total Piola-type stress tensor $\boldsymbol{S}$ is defined as $\boldsymbol{S} = J\,\boldsymbol{\tau}\boldsymbol{F}^{-T}$, so that the local referential form of the balance of linear momentum can be written as

$$\mathrm{Div}\boldsymbol{S} + \rho_0\,\boldsymbol{f} = \boldsymbol{0}\,,$$

where $\rho_0 = J\rho$ is the referential mass density. At the boundary $\partial\mathcal{B}_0$, the nominal total stress tensor $\boldsymbol{S}$ must satisfy the boundary condition

$$[\![\boldsymbol{S}]\!]\boldsymbol{N}^0 = \boldsymbol{t}^0, \tag{2.7}$$

where $\boldsymbol{t}^0$ is the nominal vector of the mechanical tractions. For the planar DEG examined, since the electrode surfaces orthogonal to $\boldsymbol{e}_3$-direction are traction-free, the boundary condition (2.7) reduces to $S_{33} = 0$.

2.2 Energy-density functions for isotropic dielectric elastomers

The energy-density function is generally defined by considering as free electrical variable the nominal electric field $\boldsymbol{E}^0$, i.e. $W = W(\boldsymbol{F}, \boldsymbol{E}^0)$. Thus, for an isotropic material, the energy can be expressed as a function of the deformation gradient and of the nominal electric field through six invariants $W(\boldsymbol{F}, \boldsymbol{E}^0) = W(I_1, I_2, I_3, I_4, I_5, I_6)$ [15]. The first three invariants are the standard mechanical invariants of $\boldsymbol{C}$, defined as

$$I_1 = \mathrm{tr}\boldsymbol{C}, \quad I_2 = 1/2[(\mathrm{tr}\boldsymbol{C})^2 - \mathrm{tr}(\boldsymbol{C}^2)], \quad I_3 = det\boldsymbol{C}, \tag{2.8}$$

while the last three are electro-mechanical invariants based on the nominal electric field $\boldsymbol{E}^0$ and defined as

$$I_4 = \boldsymbol{E}^0 \cdot \boldsymbol{E}^0, \quad I_5 = \boldsymbol{E}^0 \cdot \boldsymbol{C}^{-1}\boldsymbol{E}^0 = \boldsymbol{E} \cdot \boldsymbol{E}, \quad I_6 = \boldsymbol{E}^0 \cdot \boldsymbol{C}^{-2}\boldsymbol{E}^0. \tag{2.9}$$

The choice of the invariants in Eq. (2.10) is clearly not unique and, for example, $\boldsymbol{C}^{-1}$ could be replaced by $\boldsymbol{C}$ in I_5 and I_6 [16].

In some circumstances, it may be convenient to select the nominal electric displacement $\boldsymbol{D}^0$ as the independent electrical variable. This can be done by defining an energy-density function $\mathcal{W} = \mathcal{W}(\boldsymbol{F}, \boldsymbol{D}^0)$, complementary to W, via the partial Legendre transformation [15]

$$\mathcal{W}(\boldsymbol{F}, \boldsymbol{D}^0) = W(\boldsymbol{F}, \boldsymbol{E}^0) + \boldsymbol{D}^0 \cdot \boldsymbol{E}^0. \tag{2.10}$$

For an isotropic material, $\mathcal{W}$ depends on the three mechanical invariants I_1, I_2 and I_3, defined in Eq. (2.8), and on three additional invariants based on $\boldsymbol{D}^0$ and defined as

$$K_4 = \boldsymbol{D}^0 \cdot \boldsymbol{D}^0, \quad K_5 = \boldsymbol{D}^0 \cdot \boldsymbol{C}\boldsymbol{D}^0, \quad K_6 = \boldsymbol{D}^0 \cdot \boldsymbol{C}\boldsymbol{D}^0. \tag{2.11}$$

2.3 Electro-hyperelastic model

The material is assumed to be incompressible, lossless and governed by an isotropic energy-density function $W(\boldsymbol{F}, \boldsymbol{E}^0)$. The principle of energy conservation leads us to the equality

$$\left[\boldsymbol{S} - \frac{\partial W}{\partial \boldsymbol{F}} + p\boldsymbol{F}^{-T}\right] \cdot \dot{\boldsymbol{F}} - \left[\boldsymbol{D}^0 + \frac{\partial W}{\partial \boldsymbol{E}^0}\right] \cdot \dot{\boldsymbol{E}}^0 = 0\,, \tag{2.12}$$

where the notation $\dot{\bullet}$ denotes the material time derivative. Eq. (2.12) involves that the dissipation is equal to zero, i.e. $\mathcal{D} = 0$.

The scalar p introduced in Eq. (2.12) operates as an indeterminate Lagrange multiplier, which can be identified as a hydrostatic pressure. This scalar can only be determined from the equilibrium equations and the boundary conditions. The undetermined pressure p represents a workless reaction to the kinematic constraint on the deformation field, i.e. the incompressibility constraint $J = 1$.

The energy conservation must be valid for all admissible processes. Hence, a sufficient condition for (2.12) to be fulfilled is that

$$\boldsymbol{S} = \frac{\partial W}{\partial \boldsymbol{F}} - p\boldsymbol{F}^{-T}, \qquad \boldsymbol{D}^0 = -\frac{\partial W}{\partial \boldsymbol{E}^0}. \tag{2.13}$$

For an ideal incompressible elastomer, we can state a constitutive relation of neo-Hookean type under isothermal conditions [7, 15], namely

$$W(\boldsymbol{F}, \boldsymbol{E}^0) = \frac{\mu}{2}[I_1 - 3] - \frac{\epsilon}{2} I_5, \tag{2.14}$$

where I_1 is defined by Eq. $(2.8)_1$ and I_5 by Eq. $(2.10)_2$. Here, μ is the shear modulus and ϵ is the dielectric permittivity of the material, remaining constant along the deformation. Note that the use of the form (2.14) in Eq. $(2.13)_2$ provides the ideal dielectric behaviour $\boldsymbol{D} = \epsilon \boldsymbol{E}$.

In fact, if the dielectric is ideal, the permittivity ϵ is independent of the deformation and we can represent it as $\epsilon = \epsilon_0\, \epsilon_r$, where ϵ_r is the relative permittivity of the material. Generally, ϵ_r is referred to the undeformed configuration, i.e. $\epsilon_r = \epsilon_r^0$. Otherwise, if the dielectric has electrostrictive behaviour, the permittivity is stretch dependent and takes the form $\epsilon(\lambda_1, \lambda_2, \lambda_3) = \epsilon_0\, \epsilon_r(\lambda_1, \lambda_2, \lambda_3)$.

2.3.1 Plane-strain loading

For a parallel plate generator deformed in plane-strain by a force $\mathcal{F}_1$ applied along direction x_1, the principal stretches are $\lambda_1 = \lambda$, $\lambda_2 = 1$ and $\lambda_3 = \lambda^{-1}$. Therefore, the homogeneous electromechanical deformation undergone by the membrane can be represented by the deformation gradient $\boldsymbol{F} = \mathrm{diag}(\lambda, 1, \lambda^{-1})$. Thus, along the prescribed loading path, the Piola-type total stress tensor assumes the form $\boldsymbol{S} = \mathrm{diag}(S_{11}, S_{22}, S_{33})$, where $S_{11} = \mathcal{F}_1/(h_0 l_0)$, $S_{33} = 0$ and S_{22} is the reaction to the kinematic plane-strain constraint.

From the constitutive equations $(2.13)_{1,2}$, employing the strain-energy function (2.14), the hydrostatic pressure p can be computed imposing the vanishing of the stress along direction $\boldsymbol{e}_3$

$$p = \mu \frac{1}{\lambda^2} - \epsilon {E_3^0}^2 \lambda^2, \tag{2.15}$$

so that we can derive the following relations

$$S_{11} = \mu\left(\lambda - \frac{1}{\lambda^3}\right) - \epsilon {E_3^0}^2 \lambda, \quad S_{22} = \mu\left(1 - \frac{1}{\lambda^2}\right) - \epsilon {E_3^0}^2 \lambda^2, \quad D_3^0 = \epsilon E_3^0 \lambda^2. \tag{2.16}$$

Since D_3^0 and E_3^0 correspond to the charge density per unit reference electrode surface ω_0 and to the ratio between the current voltage ϕ and the reference thickness h_0, respectively, in the sequel we find it advantageous to rephrase the equations (2.16) in terms of the *dimensionless* variables

$$\bar{\boldsymbol{S}} = \frac{\boldsymbol{S}}{\mu}, \quad \bar{\phi} = \frac{\phi}{h_0}\sqrt{\frac{\epsilon}{\mu}}, \quad \bar{\omega}_0 = \frac{\omega_0}{\sqrt{\epsilon\mu}}. \tag{2.17}$$

Accordingly, during the harvesting cycle the relations between the applied stress, the applied electric potential, the resulting stretch ratio and the charge accumulated on the electrodes are

$$\bar{S}_{11} = \lambda - \frac{1}{\lambda^3} - \bar{\phi}^2\lambda, \quad \bar{S}_{22} = 1 - \frac{1}{\lambda^2} - \bar{\phi}^2\lambda^2, \quad \bar{\omega}_0 = \bar{\phi}\lambda^2. \tag{2.18}$$

2.3.2 Equibiaxial loading

An equibiaxial stress state of the generator, induced by an in-plane force $\boldsymbol{\mathcal{F}} = [\mathcal{F}, \mathcal{F}, 0]$, corresponds to a uniform in-plane stretch ($\lambda_1 = \lambda_2 = \lambda$). Assuming again incompressibility, the deformation gradient assumes the representation $\boldsymbol{F} = \mathrm{diag}(\lambda, \lambda, \lambda^{-2})$. Therefore, along the prescribed loading path, the total nominal stress tensor takes this form $\boldsymbol{S} = \mathrm{diag}(S_{11}, S_{22}, S_{33})$, where $S_{11} = S_{22} = S = \mathcal{F}/(h_0 l_0)$ and $S_{33} = 0$.

As in the previous case, from the constitutive equations $(2.13)_{1,2}$, employing Eq. (2.14), we can obtain the following expressions for the stress and the electric displacement

$$S_{11} = S_{22} = S = \mu\left(\lambda - \frac{1}{\lambda^5}\right) - \epsilon {E_3^0}^2\lambda^3, \qquad {D_3}^0 = \epsilon E_3^0\lambda^4, \tag{2.19}$$

having determined the hydrostatic pressure p by imposing $S_{33} = 0$

$$p = \mu\frac{1}{\lambda^4} - \epsilon {E_3^0}^2\lambda^4. \tag{2.20}$$

As in the previous case, since D_3^0 and E_3^0 correspond to the charge density per unit reference surface ω_0 and to the current voltage per unit reference thickness ϕ/h_0, respectively, we find it advantageous to rephrase equations (2.19) in terms of the dimensionless variables (2.17)

$$\bar{S} = \lambda - \frac{1}{\lambda^5} - \bar{\phi}^2\lambda^3, \qquad \bar{\omega}_0 = \bar{\phi}\lambda^4. \tag{2.21}$$

2.4 Electro-viscoelastic model

Typical DEs (acrylic elastomers, silicones, rubber) display time-dependent properties. Hence, it is relevant to extend the electro-elastic framework in order to include viscoelastic effects and to thereby model the rate-dependence mechanical behaviour of the material. We assume that the viscosity is related to mechanical contributions only. This means that, even though the material deforms in response of an applied electric voltage, the viscosity is related to the induced deformation only, and not directly to the electrical quantities. In the present work, we will refer to the viscoelastic model proposed by Ask et al. [2, 3], and to the one by Gei and collaborators [5, 22] for the electromechanical behaviour. The main hypotheses at the basis of the electro-viscoelastic model lie in the assumption that the electric fields are static whereas the mechanical response, though quasi-static, is rate-dependent.

A common approach to model viscoelasticity, see e.g. [34, 41, 50], in the finite-strain framework is based on the introduction of a multiplicative split of the deformation gradient into elastic and viscous contributions

$$\boldsymbol{F} = \boldsymbol{F}_{e\alpha}\boldsymbol{F}_{v\alpha}\,, \tag{2.22}$$

where subscript α indicates the possibility of multiple viscosity elements. The multiplicative decomposition (2.22) can be considered as a three-dimensional generalisation of the splitting occurring in a one-dimensional Maxwell rheological element, where a spring and a dashpot are connected in series. In a generalised Maxwell rheological model, an arbitrary number of Maxwell elements is connected in parallel. For later reference, it is convenient to introduce a Cauchy-Green-type deformation tensor defined as

$$\boldsymbol{C}_{v\alpha} = \boldsymbol{F}_{v\alpha}^T\boldsymbol{F}_{v\alpha}\,, \tag{2.23}$$

for each Maxwell element α. This tensor will be taken as the internal variable and shall satisfy $\det \boldsymbol{C}_{v\alpha} = 1$.

Taking into account the viscoelastic effects, the second law of thermodynamics leads us to the dissipation inequality, which is the basis to formulate constitutive equations. In local form, the Clausius–Duhem inequality is

$$\mathcal{D} = \left[\boldsymbol{S} - \frac{\partial W}{\partial \boldsymbol{F}} + p\boldsymbol{F}^{-T}\right]\cdot\dot{\boldsymbol{F}} - \left[\boldsymbol{D}^0 + \frac{\partial W}{\partial \boldsymbol{E}^0}\right]\cdot\dot{\boldsymbol{E}}^0 - \sum_{\alpha}\frac{\partial W}{\partial \boldsymbol{C}_{v\alpha}}\cdot\dot{\boldsymbol{C}}_{v\alpha} \geq 0\,, \tag{2.24}$$

where the last term represent the contribution of viscoelasticity. We remind that the notation $\dot{\bullet}$ denotes the material time derivative.

In order to fully characterise the material behaviour, it is necessary to formulate evolution equations for the internal variables, which describe the rate-dependence of the mechanical quantities.

As we have said, it is assumed that the elastomer is an incompressible material ($J = 1$) complying with a constitutive relation of neo-Hookean type under isothermal conditions. Assuming the nominal electrical field $\boldsymbol{E}^0$ as the independent electrical variable and including viscoelastic effects, the strain-energy function is now considered to take the representation

$$W(\boldsymbol{F}, \boldsymbol{E}^0, \boldsymbol{C}_{v\alpha}) = \frac{\mu}{2}[I_1 - 3] + \frac{1}{2}\sum_{\alpha} \beta_\alpha \, \mu \, [I_{1v\alpha} - 3] - \frac{\epsilon}{2} I_5 \, , \tag{2.25}$$

with I_1 defined by Eq. $(2.8)_1$, $I_{1v\alpha} = \mathrm{tr}(\boldsymbol{C}\boldsymbol{C}_{v\alpha}^{-1})$ and I_5 defined by Eq. $(2.10)_2$. Here, μ is the long-term shear modulus of the material and β_α are positive dimensionless proportionality factors, which relate the shear modulus of the viscous element α to the long-term shear modulus μ.

Based on equation (2.25), a necessary condition for the evolution equations of the internal variables to satisfy is

$$\mathcal{D}_v = -\sum_{\alpha} \frac{\partial W}{\partial \boldsymbol{C}_{v\alpha}} \cdot \dot{\boldsymbol{C}}_{v\alpha} \geq 0 \, . \tag{2.26}$$

The definition of a Mandel-type referential stress tensor as

$$\boldsymbol{M}_{v\alpha} = -\boldsymbol{C}_{v\alpha} \frac{\partial W}{\partial \boldsymbol{C}_{v\alpha}} \tag{2.27}$$

allows to restate the dissipation inequality in the following form

$$\mathcal{D}_v = \sum_{\alpha} \boldsymbol{M}_{v\alpha} \cdot [\boldsymbol{C}_{v\alpha}^{-1} \dot{\boldsymbol{C}}_{v\alpha}] \geq 0 \, . \tag{2.28}$$

A possible format of the evolution equations, which fulfills the dissipation inequality and ensures the symmetry of $\boldsymbol{C}_{v\alpha}$, see [2, 3], is given by

$$\dot{\boldsymbol{C}}_{v\alpha} = \dot{\mathit{\Gamma}}_\alpha \, \boldsymbol{C}_{v\alpha} \boldsymbol{M}_{v\alpha}^{dev\,T} \, , \tag{2.29}$$

where $\dot{\mathit{\Gamma}}_\alpha$ are material parameters, related to the inverse of the viscosity of each α Maxwell element.

2.5 Load-driven harvesting cycle

In the optimisation of the ideal hyperelastic planar DEG (Chapters 3 and 4), we analyse the four-stroke cycle shown schematically in Fig. 2.2c, in which the load and the charge are alternately held constant. Specifically, the four-strokes are

1. stroke A-B: the membrane is stretched by increasing the applied load from $S^A = S_{min}$ to $S^B = S_{max}$ under open circuit condition. During this stage the charge on the electrodes is fixed, so that $\omega_0^A = \omega_0^B$;
2. stroke B-C: at the stretched configuration the charge on the electrodes increases from ω_0^B to ω_0^C by applying a potential jump $\Delta\phi$. During this stroke the load is held fixed, so that $S^B = S^C = S_{max}$;
3. stroke C-D: the elastomer is released by decreasing the load from S^C to $S^D = S^A = S_{min}$, under open circuit condition. In this way the charge is kept constant, so that $\omega_0^C = \omega_0^D$. Note that, during this phase, both the potential between the two electrodes and the electric field increase, attaining their maximal values at the end of the stroke (point D);
4. stroke D-A: the surplus charge $\omega_0^C - \omega_0^A$ is harvested at the high potential to the storage battery while the load is held constant, so that $S^D = S^A = S_{min}$.

The cycle is represented on the thermodynamical planes, as shown in Fig. 2.2. Specifically, Fig. 2.2a corresponds to the mechanical S–λ plane and Fig. 2.2b to the electrical ϕ–ω_0 plane. We note that, practically, strokes B–C and D–A are substantially shorter than the mechanical loading and unloading phases. Thus, the applied external force should be thought of as a continuously oscillating force such that, when it attains its maximal and minimal values, appropriate electrical circuits are temporarily connected to the electrodes. In a real harvesting circuit, instead, the generator is permanently connected to an electric load and to a battery composing a single circuit, as explained later in Chapter 6, and the cycle differs from the one presented here.

The four-stroke harvesting cycle described above is characterised by the four equalities listed in Fig. 2.2c, namely

$$\bar{\omega}_0^A = \bar{\omega}_0^B, \qquad \bar{S}^B = \bar{S}^C, \qquad \bar{\omega}_0^C = \bar{\omega}_0^C, \qquad \bar{S}^D = \bar{S}^A. \tag{2.30}$$

For an ideal lossless dielectric, depending on the loading conditions, equalities (2.30) induce the following relations among the eight values attained at each state of the

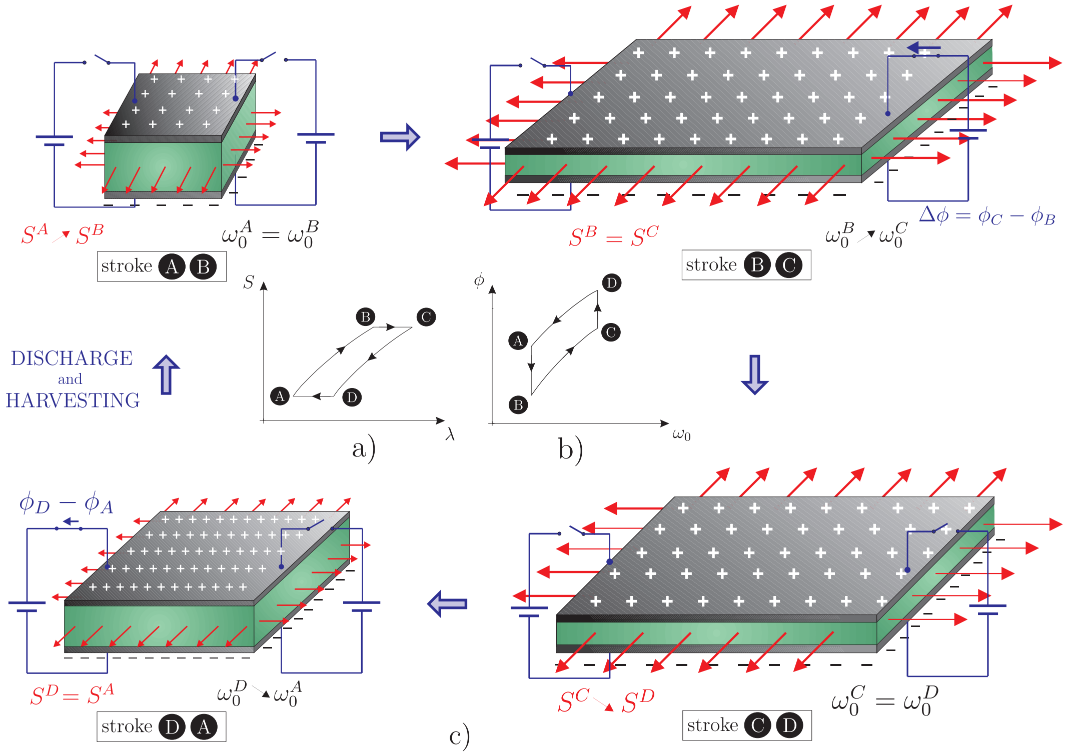
$S^A \nearrow S^B$
$\omega_0^A = \omega_0^B$
stroke A B
$S^B = S^C$
$\omega_0^B \nearrow \omega_0^C$
$\Delta\phi = \phi_C - \phi_B$
stroke B C
DISCHARGE
and
HARVESTING
S
λ
A
B
C
D
a)
ϕ
ω_0
b)
$\phi_D - \phi_A$
$S^D = S^A$
$\omega_0^D \nwarrow \omega_0^A$
stroke D A
$S^C \searrow S^D$
$\omega_0^C = \omega_0^D$
stroke C D
c)

FIGURE 2.2: The load-driven harvesting cycle plotted on the a) mechanical and b) electrical planes and c) illustration of the four strokes with a service battery at the right and a storage battery at the left; the illustrations in c) are referred to the initial states of each individual stroke.

generator by the two independent variables, namely the stretch λ and the dimensionless voltage $\bar{\phi}$,

- **plane-strain loading:**

$$\begin{aligned} \bar{\phi}_A\lambda_A^2 &= \bar{\phi}_B\lambda_B^2, \qquad & \lambda_B - \frac{1}{\lambda_B^3} - \bar{\phi}_B^2\lambda_B &= \lambda_C - \frac{1}{\lambda_C^3} - \bar{\phi}_C^2\lambda_C, \\ \bar{\phi}_C\lambda_C^2 &= \bar{\phi}_D\lambda_D^2, \qquad & \lambda_D - \frac{1}{\lambda_D^3} - \bar{\phi}_D^2\lambda_D &= \lambda_A - \frac{1}{\lambda_A^3} - \bar{\phi}_A^2\lambda_A; \end{aligned} \tag{2.31}$$

- **equibiaxial loading:**

$$\begin{aligned} \bar{\phi}_A\lambda_A^4 &= \bar{\phi}_B\lambda_B^4, \qquad & \lambda_B - \frac{1}{\lambda_B^5} - \bar{\phi}_B^2\lambda_B^3 &= \lambda_C - \frac{1}{\lambda_C^5} - \bar{\phi}_C^2\lambda_C^3, \\ \bar{\phi}_C\lambda_C^4 &= \bar{\phi}_D\lambda_D^4, \qquad & \lambda_D - \frac{1}{\lambda_D^5} - \bar{\phi}_D^2\lambda_D^3 &= \lambda_A - \frac{1}{\lambda_A^5} - \bar{\phi}_A^2\lambda_A^3. \end{aligned} \tag{2.32}$$

2.6 Modes of failure and failure envelope

From an engineering viewpoint, to ensure proper operational conditions of the device, all feasible cycles must lie inside the domain of admissible states for the generator [36, 49, 62]. The contour line that envelops this region is defined by the following possible failure modes of the DEG:

- **electric breakdown** EB: this failure, which depends on the properties of the dielectric elastomer membrane, occurs when the current electric field E reaches the dielectric strength of the material E_{eb};
- **electromechanical instability** EMI: as the electric potential between the electrodes increases the force attracting the electrodes increases too, resulting in thinning of the elastomeric membrane. This, in turn, further increases the force between the electrodes even without any additional increase in the electric potential. At some critical combination of the electric field and the mechanical loading the membrane cannot withstand the attraction force between the electrodes and may collapse [5, 52]. The concept of electromechanical instability is theoretically a loss of positive definiteness of the tangent electro–elastic constitutive operator and is an admissible instability for dead-load tractions/charges on the boundary [5, 21, 52]. When the dielectric is constrained, electromechanical instability may lead the soft film to the typical two-phase pattern, where wrinkled areas and homogeneous zones coexist [49];
- **ultimate stretch** λ_U: this failure also depends on the properties of the film material and takes place when the magnitude of the stretch attains a critical value λ_U at which mechanical failure initiates. In a single loading cycle the ultimate stretch ratio of the VHB-4910 membrane is fairly large and may reach values larger than 5. Nevertheless, it is anticipated that under cyclic loading conditions this value is more restrictive. Accordingly, in the subsequent analysis the ultimate stretch has been limited to value smaller than 3.5;
- **loss of the tensile state** (S=0): to avoid failure due to buckling and wrinkling in compression it is required that the two in-plane stresses be positive. In contrast with the previous failure modes, this one is associated with the geometrical configuration of the device and is related to the small thickness of the film.

We finally add a fourth formal condition, which does not correspond to a failure mode, requiring that the direction of the electric field is not reversed during the cycle, i.e. the **irreversibility of the electric field** $E \geq 0$.

2.6.1 Ideal hyperelastic DEG under plane-strain loading conditions

In the case of an ideal lossless DEG under plane-strain loading conditions, the parts of the failure envelops corresponding to the failure modes defining the region of admissible states in the two work-conjugated planes, can be expressed explicitly in terms of the dimensionless quantities (2.17).

The current **electric breakdown** strength in the dimensionless form is

$$\bar{E}_{eb} = E_{eb}\sqrt{\frac{\epsilon}{\mu}}, \tag{2.33}$$

while the dimensionless nominal electrical field is bounded by $\bar{E}^0_{eb} = \bar{E}_{eb}\lambda_3$. Hence, for the plane-strain loading mode, the electric breakdown corresponds to this condition

$$\bar{\phi} = \bar{E}^0_{eb} = \frac{\bar{E}_{eb}}{\lambda}. \tag{2.34}$$

Inverting the relation $(2.18)_3$ and imposing the failure constraint (2.34), we can obtain the stretch in function of the dimensionless nominal charge density

$$\lambda = \frac{\bar{\omega}_0}{\bar{E}_{eb}}. \tag{2.35}$$

Thus, substituting Eq. (2.34) in Eq. $(2.18)_1$ and Eq. (2.35) in Eq. $(2.18)_3$, we can define the curves corresponding to the electric breakdown failure EB, which surround the region of admissible states respectively in the mechanical and electric planes, as

$$\bar{S}_{11} = \lambda - \frac{1}{\lambda^3} - \frac{\bar{E}^2_{eb}}{\lambda}, \quad \bar{\phi} = \frac{\bar{E}^2_{eb}}{\bar{\omega}_0}. \tag{2.36}$$

The **ultimate stretch** failure is characterised by the condition $\lambda = \lambda_U$ for any value of the stress, hence this failure constraint corresponds to a vertical straight line on the mechanical $\bar{S}$–λ plane. The equivalent curve on the electrical plane can be easily obtained substituting the failure constraint in Eq. $(2.18)_3$. Therefore, the curves corresponding to the ultimate stretch in the mechanical and the electric planes are, respectively,

$$\lambda = \lambda_U, \quad \bar{\phi} = \frac{\bar{\omega}_0}{\lambda^2_U}. \tag{2.37}$$

As far as the planar DEG is concerned, under plane-strain conditions, since the DE membrane is constrained in one direction, the electromechanical instability is not a possible failure [5]. Therefore, in the following, only **loss of tension** is accounted for. A comparison between Eqs. $(2.18)_1$ and $(2.18)_2$ for the two stresses reveals that the inequality $S_{22} \geq 0$ is more restrictive than $S_{11} \geq 0$. Therefore, by imposing the vanishing of the right-hand side of Eq. (2.18)$_2$, we can obtain the dimensionless voltage as a function of the stretch

$$\bar{\phi} = \sqrt{\frac{1}{\lambda^2} - 1}. \tag{2.38}$$

At the same way, inverting Eq. (2.18)$_3$ and substituting it in Eq. (2.18)$_2$, we can obtain the stretch as a function of the nominal charge density by requiring Eq. (2.18)$_2$ to be zero (i.e. $S_{22} = 0$)

$$\lambda = \sqrt{1 + \bar{\omega}_0^2}. \tag{2.39}$$

Hence, after substitution of the failure constraint (2.38) in Eq. (2.18)$_1$ and of relation (2.39) in Eq. (2.18)$_3$, we can characterise, in the two pertinent planes, the portions of the failure envelops corresponding to loss of tension by the curves

$$\bar{S}_{22} = 0, \quad \bar{S}_{11} = \lambda - \frac{1}{\lambda}, \quad \bar{\phi} = \frac{\bar{\omega}_0}{(1 + \bar{\omega}_0^2)}. \tag{2.40}$$

In the mechanical plane the curve corresponding to the last formal condition, i.e. the **irreversibility of the electric field** $E \geq 0$, is characterised by the relation

$$\bar{S}_{11} = \lambda - \frac{1}{\lambda^3}, \tag{2.41}$$

resulting from imposing $\bar{\phi} = 0$ in Eq. (2.18)$_1$.

The plot of these curves on the dimensionless electrical $\bar{\phi}$–$\bar{\omega}_0$ plane is shown in Fig. 2.3 for different values of the electric breakdown threshold $\bar{E}_{eb}$ and of the ultimate stretch λ_U.

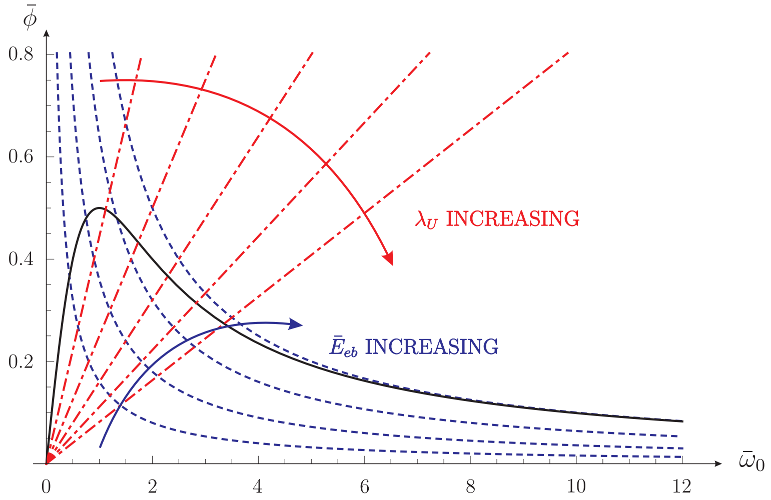

FIGURE 2.3: Failure envelopes for a plane-strain loaded DEG on the electrical $\bar{\phi}$–$\bar{\omega}_0$ plane for increasing values of the electric breakdown strength ($\bar{E}_{eb} = 0.4, 0.6, 0.8, 1$) and of the ultimate stretch ($\lambda_U = 1.5, 2, 2.5, 3, 3.5$).

At fixed electromechanical properties of the material, for example $\bar{E}_{eb} = 0.8$ and $\lambda_U = 3$, the failure curves for the plane-strain loaded generator can be plotted on the two dimensionless work-conjugated planes, as depicted in Figs. 2.4a and 2.4b.

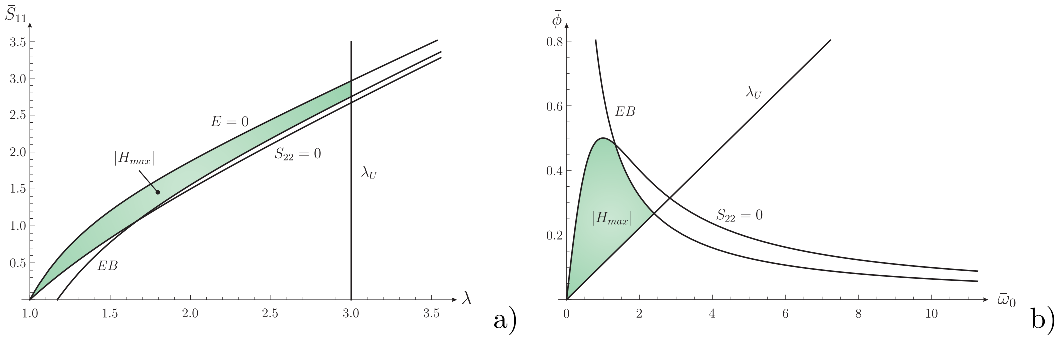

FIGURE 2.4: Failure envelopes at $\bar{E}_{eb} = 0.8$ and $\lambda_U = 3$ on the a) mechanical $\bar{S}_{11}$–λ and b) electrical $\bar{\phi}$–$\bar{\omega}_0$ planes for a plane-strain loaded DEG.

The area enclosed by the failure envelope is the allowable state region and its measure corresponds to the theoretically achievable energy-density per unit shear modulus H_{max}.

2.6.2 Ideal hyperelastic DEG under equibiaxial loading conditions

In the case of equibiaxial loading conditions, the failure curves, delimiting the admissible state region in the work-conjugated planes, can be expressed explicitly in terms of the dimensionless quantities (2.17), as illustrated in the previous Subsection for the plane-strain case.

For the equibiaxial loading mode, the **electric breakdown** corresponds to

$$\bar{\phi} = \bar{E}^0_{eb} = \bar{E}_{eb}\lambda_3 = \frac{\bar{E}_{eb}}{\lambda^2}. \tag{2.42}$$

Inverting Eq. $(2.21)_2$ and imposing the failure constraint (2.42), we can obtain the stretch as a function of the dimensionless nominal charge density

$$\lambda = \sqrt{\frac{\bar{\omega}_0}{\bar{E}_{eb}}}. \tag{2.43}$$

Thus, substituting relation (2.43) in Eq. $(2.21)_2$, the curves in the mechanical and in the electric planes corresponding to the electric breakdown failure are respectively prescribed as

$$\bar{S} = \lambda - \frac{1}{\lambda^5} - \frac{\bar{E}^2_{eb}}{\lambda}, \quad \bar{\phi} = \frac{\bar{E}^2_{eb}}{\bar{\omega}_0}. \tag{2.44}$$

Since we assume that the deformation is homogeneous and the film thickness uniform, the critical condition characterising the **electromechanical instability** can be identified inverting relation (2.21)$_2$ and expressing the voltage as a function of the stress and of the stretch

$$\bar{\phi} = \bar{\phi}(\bar{S}, \lambda) = \sqrt{-\bar{S}\frac{1}{\lambda^3} + \frac{1}{\lambda^2} - \frac{1}{\lambda^8}}. \tag{2.45}$$

By maximising Eq. (2.45) at constant $\bar{S}$ and combining Eqs. (2.21)$_{1,2}$, we can find the analytical expression of the curves corresponding to the electromechanical instability in the two thermodynamic planes

$$\bar{S} = \frac{2}{3}\left(\lambda - 4\frac{1}{\lambda^5}\right), \quad \bar{\phi} = \frac{\bar{\omega}_0}{(3\bar{\omega}_0^2 - 5)^{2/3}}. \tag{2.46}$$

In general, methods to investigate instabilities in electromechanically loaded films triggered by imperfections or inhomogeneities were presented in [13, 17, 22, 53].

As for the plane-strain loading mode, the **ultimate stretch** failure is characterised by the condition $\lambda = \lambda_U$ for any value of the stress, hence this failure constraint individuates a vertical line on the mechanical plane. The equivalent curve on the electrical plane can be easily obtained substituting the failure constraint in Eq. (2.21)$_2$. Therefore, in the mechanical and the electric planes the ultimate stretch limits are

$$\lambda = \lambda_U, \quad \bar{\phi} = \frac{\bar{\omega}_0}{\lambda_U^4}; \tag{2.47}$$

The condition characterising the **loss of tension** can be simply identified by imposing the vanishing of the right-hand side of Eq. (2.21)$_1$. Inverting Eq. (2.21)$_2$ and substituting it in Eq. (2.21)$_1$, we can obtain the nominal charge density as a function of the stretch

$$\lambda = (1 + \bar{\omega}_0^2)^{1/6}. \tag{2.48}$$

Hence, after substitution of Eq. (2.48) in Eq. (2.21)$_2$, we obtain two curves which characterise the portions of the failure envelops corresponding to loss of tension in the work-conjugated planes, i.e.

$$\bar{S} = 0, \quad \bar{\phi} = \frac{\bar{\omega}_0}{(1 + \bar{\omega}_0^2)^{2/3}}. \tag{2.49}$$

Finally, in the mechanical plane the curve corresponding to the condition on the **irreversibility of the electric field** is characterised by the relation

$$\bar{S} = \lambda - \frac{1}{\lambda^5}, \tag{2.50}$$

obtained by imposing $\bar{\phi} = 0$ in Eq. (2.21)$_1$.

The plot of these curves on the dimensionless electrical $\bar{\phi}$–$\bar{\omega}_0$ plane is shown in Fig. 2.5 for increasing values of the electric breakdown threshold $\bar{E}_{eb}$ and of the ultimate stretch λ_U.

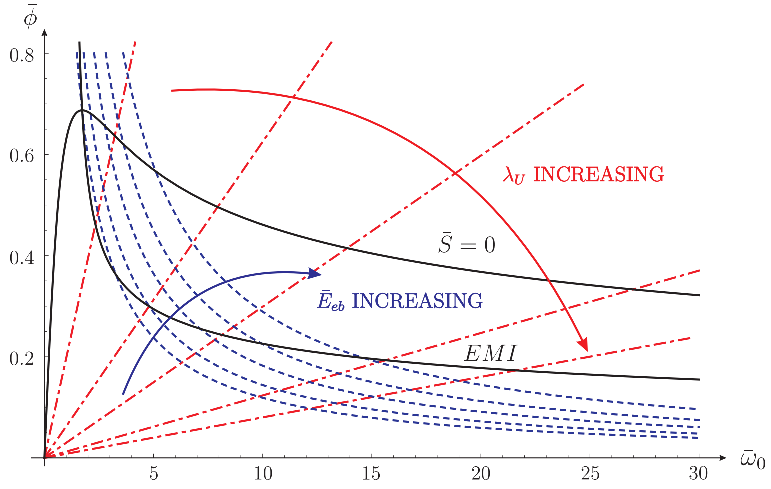

FIGURE 2.5: Failure envelopes for an equibiaxially loaded DEG on the electrical $\bar{\phi}$–$\bar{\omega}_0$ plane for increasing values of the electric breakdown strength ($\bar{E}_{eb} = 1.09, 1.2, 1.3, 1.5, 1.7$) and of the ultimate stretch ($\lambda_U = 1.5, 2, 2.5, 3, 3.5$).

Once the electromechanical properties ($\bar{E}_{eb}$, λ_U) of the dielectric membrane are defined, it is possible to determine the allowable state region. The plots of the failure envelope for a equibiaxially loaded DEG on the two dimensionless work-conjugated $\bar{S}$–λ and $\bar{\phi}$–$\bar{\omega}_0$ planes are depicted respectively in Figs. 2.6a and 2.6b for $\bar{E}_{eb} = 0.8$ and $\lambda_U = 3$.

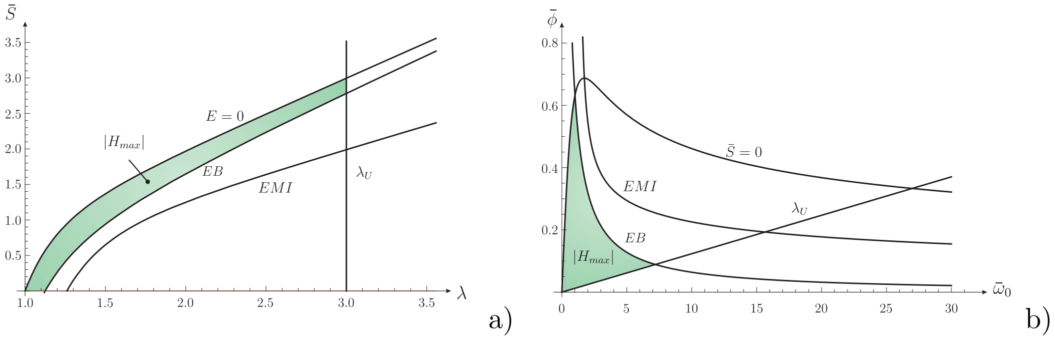

FIGURE 2.6: Failure envelopes at $\bar{E}_{eb} = 0.8$ and $\lambda_U = 3$ on the a) mechanical $\bar{S}$–λ and b) electrical $\bar{\phi}$–$\bar{\omega}_0$ planes for an equibiaxially loaded DEG.

2.7 Performance of a dielectric elastomer generator: gained and invested energies, effectiveness and efficiency

Assuming no body forces and no charge distribution within the dielectric, during a finite time interval Δt from a generic state (1) to a generic state (2) of the electromechanical cycle illustrated in Sect. 2.5, the energy variation is [45]

$$U_{(2)} - U_{(1)} + \frac{\epsilon_0}{2}\left(E_{(2)}^2 - E_{(1)}^2\right) = \int_{t_1}^{t_2} \boldsymbol{S}\cdot\dot{\boldsymbol{F}}\mathrm{d}t + \int_{t_1}^{t_2} \boldsymbol{E}^0\cdot\dot{\boldsymbol{D}}^0\mathrm{d}t = W_{(2)} - W_{(1)}, \quad (2.51)$$

where U is the internal energy-density stored in the material, $E = |\boldsymbol{E}|$ is the modulus of the current electric field and $W = W(\boldsymbol{F}, \boldsymbol{E}^0)$ is the strain energy function, see Sect. 2.2.

Noting that during the cycle, described in Fig. 2.2c of Sect. 2.5, the system is electrically isolated during strokes A–B and C–D, by using Eq. (2.51), the **total flux of electrical energy per unit referential volume** is

$$\begin{aligned}\tilde{H}_g &= \int_{t_B}^{t_C} \boldsymbol{E}^0\cdot\dot{\boldsymbol{D}}^0\mathrm{d}t + \int_{t_D}^{t_A} \boldsymbol{E}^0\cdot\dot{\boldsymbol{D}}^0\mathrm{d}t \\ &= W^C - W^B - \boldsymbol{S}^B\cdot(\boldsymbol{F}^C - \boldsymbol{F}^B) + W^A - W^D - \boldsymbol{S}^A\cdot(\boldsymbol{F}^A - \boldsymbol{F}^D).\end{aligned} \quad (2.52)$$

For later reference, we recall that $\tilde{H}_g$ is the energy extracted from the system and its sign is negative.

Mechanical and electrical works are invested into the system during strokes A–B and B–C. By employing once again Eq. (2.51), the **total invested work per unit reference volume** is simply

$$\tilde{H}_i = W^C - W^A. \quad (2.53)$$

An alternative way to estimate the **energy harvested** during the cycle is to evaluate the area enclosed by the cycle on the dimensionless electrical plane $\bar{\phi} - \bar{\omega}_0$. In fact, in the static and quasi-static cases according to the four-stroke cycle described in Sect. 2.5 the energy harvested by the soft capacitor is

$$\tilde{H}_g = \int_B^C \phi\,\mathrm{d}Q + \int_D^A \phi\,\mathrm{d}Q. \quad (2.54)$$

Since the deformation is homogeneous and the measure of the area delimited by the cycle in the dimensionless electrical plane is equal to the energy-density generated per unit shear modulus $H_g = \tilde{H}_g/(\mu V_0)$, it is convenient to express the energy in terms of the dimensionless variables $\bar{\phi}$ and $\bar{\omega}_0$,

$$H_g = \int_B^C \bar{\phi}\, \mathrm{d}\bar{\omega}_0 + \int_D^A \bar{\phi}\, \mathrm{d}\bar{\omega}_0. \tag{2.55}$$

Sine the **total invested energy** is the sum of the mechanical and electrical energies provided to the generator during strokes A–B and B–C respectively, H_i can be computed through integrations along those paths on the electrical and mechanical dimensionless planes

$$H_i = \frac{\tilde{H}_i}{\mu V_0} = \int_B^C \bar{\phi}\, \mathrm{d}\bar{\omega}_0 + \kappa \int_A^C \bar{S}\, \mathrm{d}\lambda, \tag{2.56}$$

where the factor κ multiplying the second integral depends on the loading conditions of the membrane, e.g. κ is equal to two for equibiaxial load, whereas it is unitary for plane-strain and uniaxial loads. Since $\bar{S}$ is constant along the path B–C, while it is variable along the path A–B ($\bar{S} = \bar{S}(\lambda)$), the second integral in Eq. (2.56) has to be split into two contributes, so that Eq. (2.56) turns out to be

$$H_i = \frac{\tilde{H}_i}{\mu V_0} = \int_B^C \bar{\phi}\, \mathrm{d}\bar{\omega}_0 + \kappa \int_A^B \bar{S}(\lambda)\, \mathrm{d}\lambda + \kappa \int_B^C \bar{S}_{const}\, \mathrm{d}\lambda. \tag{2.57}$$

Thus, as a measure for the generator performance, we define the **efficiency** of the generator

$$\eta = \left| \frac{H_g}{H_i} \right|. \tag{2.58}$$

Once the dielectric strength and the ultimate stretch are determined, we can compute the **theoretically achievable energy**, that is the area bounded by the failure curves on the electrical ϕ–Q plane

$$\tilde{H}_{max} = \left| \oint \phi_{failure}\, \mathrm{d}Q \right|, \tag{2.59}$$

irrespective of the integration path direction. Here, $\phi_{failure}$ is the piecewise function defining the close failure envelope.

Since the measure of the area enclosed by the failure envelope in the dimensionless electrical plane is equal to the energy-density theoretically achievable per unit shear modulus $H_{max} = \tilde{H}_{max}/(\mu V_0)$, it is convenient to express the energy in terms of the dimensionless variables $\bar{\phi}$ and $\bar{\omega}_0$,

$$H_{max} = \left| \oint \bar{\phi}_{failure}\, \mathrm{d}\bar{\omega}_0 \right|. \tag{2.60}$$

Therefore, an alternative way to estimate the performance of a generator is to compute the **effectiveness**

$$\zeta = \frac{|H_g|}{H_{max}}, \tag{2.61}$$

that is the ratio of the optimal dimensionless gained energy H_g to the dimensionless theoretically achievable energy H_{max}.

The computation of both the efficiency and the effectiveness allows the comparison of the various optimal cycles for materials with different electromechanical characteristics.

Moreover, in order to compare the performance of generators made up of different materials, it is convenient to define the energies per unit mass

$$\hat{H}_g = \frac{\mu H_g}{\rho}, \qquad \hat{H}_i = \frac{\mu H_i}{\rho}, \qquad \hat{H}_{max} = \frac{\mu H_{max}}{\rho}, \tag{2.62}$$

with $\rho = \rho_0$ due to incompressibility.

Chapter 3

Optimisation of an ideal DEG in plane-strain loading mode

This Chapter focuses on the performance optimisation of the ideal hyperelastic planar generator deforming in plane-strain presented in Subsect. 2.3.1. The membrane is constrained along direction x_2 and deformed by a force applied along direction x_1, as sketched in Fig. 3.1.

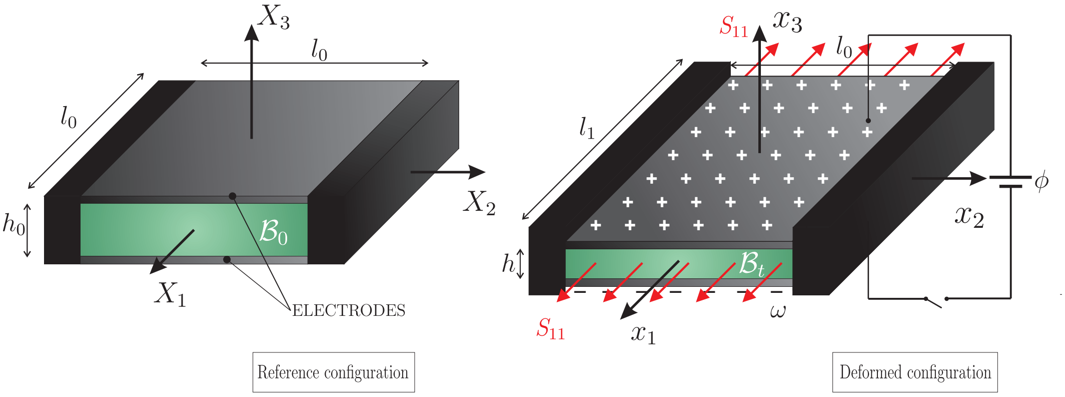
X_3
l_0
l_0
h_0
$\mathcal{B}_0$
X_2
X_1
ELECTRODES
Reference configuration
S_{11}
x_3
l_0
l_1
ϕ
x_2
h
$\mathcal{B}_t$
S_{11}
x_1
ω
Deformed configuration

FIGURE 3.1: Reference and deformed configurations of a soft planar DE generator with undeformed dimensions ($l_0 \times l_0 \times h_0$) subjected to a plane-strain loading: as a result of the deformation, the current dimensions are $l_1 = l_0\lambda$, $l_2 = l_0$ and $h = h_0\lambda^{-1}$.

In the following, we optimise the performance of this ideal generator by determining the optimal cycle, within the admissible state region, out of which the maximal energy can be harvested. Details about the failure envelope have been introduced in Subsect. 2.6.1.

3.1 Constrained optimisation problem for plane-strain loading mode

In the following, we specialise expressions (2.55) of the generated energy and (2.56) of the invested energy for the plane-strain loading mode. The possible failures of the generator will be taken into account as constraints to the cycle optimisation. Particular attention will be paid to the electric breakdown and its influence on both the allowable state region and the failure characterising the optimal cycle.

3.1.1 The harvested energy H_g

With reference to the load-driven harvesting cycle illustrated in Sect. 2.5, noting that S_{11} is constant along both paths B–C and A–D, letting $\bar{S}_{11}^{const} = \bar{S}_{11}^{B}$ along the former and $\bar{S}_{11}^{const} = \bar{S}_{11}^{A}$ along the latter, it is convenient to express the dimensionless electric voltage $\bar{\phi}$ as a function of the stretch λ and the constant stress $\bar{S}_{11}^{const}$. Thus, employing $(2.18)_1$, along the two paths

$$\bar{\phi}(\lambda) = \sqrt{1 - \lambda^{-4} - \bar{S}_{11}^{const}\lambda^{-1}}. \tag{3.1}$$

Moreover, Eq. $(2.18)_3$ allows us to evaluate the differential $\mathrm{d}\bar{\omega}_0$ in terms of the same pair

$$\mathrm{d}\bar{\omega}_0 = \mathrm{d}[\bar{\phi}(\lambda)\lambda^2] = \frac{4\lambda - 3\bar{S}_{11}^{const}}{2\sqrt{1 - \lambda^{-4} - \bar{S}_{11}^{const}\lambda^{-1}}}\mathrm{d}\lambda. \tag{3.2}$$

Hence, the first integral in Eq. (2.55) can be evaluated explicitly

$$\int_B^C \bar{\phi}\,\mathrm{d}\bar{\omega}_0 = \int_{\lambda_B}^{\lambda_C} \left(2\lambda - \frac{3}{2}\bar{S}_{11}^{const}\right)\mathrm{d}\lambda = \left|\lambda\left(\lambda - \frac{3}{2}\bar{S}_{11}^{const}\right)\right|_{\lambda_B}^{\lambda_C}. \tag{3.3}$$

The second integral can be analogously determined. Summation of the two integrals leads to the explicit expression for the dimensionless gained energy, namely

$$H_g = \frac{1}{2}\left[2(\lambda_C^2 - \lambda_B^2) - 3\bar{S}_{11}^{B}(\lambda_C - \lambda_B) + 2(\lambda_A^2 - \lambda_D^2) - 3\bar{S}_{11}^{A}(\lambda_A - \lambda_D)\right]. \tag{3.4}$$

Since $\lambda\bar{S}_{11}^{const} = -\frac{1}{\lambda^2}\lambda^2 - \lambda^2\bar{\phi}^2$, Eq. (3.4) can be written as

$$\begin{aligned} H_g =& \frac{1}{2}\left(\frac{1}{\lambda_A^2} + \lambda_A^2 + \lambda_A\bar{\phi}_A^2\right) - \frac{1}{2}\left(\frac{1}{\lambda_D^2} + \lambda_D^2 + \lambda_D\bar{\phi}_D^2\right) - \bar{S}_{11}^{A}(\lambda_A - \lambda_D) \\ &+ \frac{1}{2}\left(\frac{1}{\lambda_C^2} + \lambda_C^2 + \lambda_C\bar{\phi}_C^2\right) - \frac{1}{2}\left(\frac{1}{\lambda_B^2} + \lambda_B^2 + \lambda_B\bar{\phi}_B^2\right) - \bar{S}_{11}^{B}(\lambda_C - \lambda_B). \end{aligned} \tag{3.5}$$

In addition, according to Eq. (2.18), we can impose the equalities

$$\lambda_C = \lambda_U, \quad \bar{\phi}_D = \bar{E}_U \lambda_D^{-1}, \quad \Delta\bar{\phi} = \bar{\phi}_C - \bar{\phi}_B, \tag{3.6}$$

through relations (2.31). Here, $\bar{E}_U$ is the dimensionless ultimate electric field and $\Delta\bar{\phi}$ is the dimensionless applied voltage jump. The first equality in Eq. (3.6) guarantees that indeed at point C the device attains the maximal allowable stretch for the elastomeric membrane. The second equality ensures that at point D, when the maximal electrical field is induced through the membrane, its value equals the membrane electric breakdown field. These two conditions are required in order to maximise the harvested energy within the failure envelope. The last equality in Eq. (3.6) simply relates the electric potentials at points B and C in terms of the initial controllable quantity $\Delta\bar{\phi}$.

Upon substitution of relations (3.6) into expression (3.5), we end up with the following expression for harvested energy as a function of the parameters set $\{\lambda_A, \lambda_B, \lambda_D, \Delta\bar{\phi}, \bar{E}_U\}$,

$$\begin{aligned} H_g(\lambda_A, \lambda_B, \lambda_D, \Delta\bar{\phi}, \bar{E}_U) =& \frac{1}{2}\Bigg\{ \frac{1}{\lambda_A^2} - \frac{1}{\lambda_D^2} + \frac{1}{\lambda_U^2} - \frac{1}{\lambda_B^2} + \lambda_A^2 - \lambda_D^2 + \lambda_U^2 - \lambda_B^2 \\ &+ \bar{E}_U \left(\frac{\lambda_D^2}{\lambda_U^2} - 1 \right) + \lambda_B^2 \left(\frac{\lambda_B^2}{\lambda_A^2} - 1 \right) \left(\Delta\bar{\phi} - \frac{\bar{E}_U \lambda_D}{\lambda_U^2} \right)^2 \\ &- 2(\lambda_A - \lambda_D) \left[\lambda_A - \frac{1}{\lambda_A^3} \left(1 + \lambda_B^4 \left(\Delta\bar{\phi} - \frac{\bar{E}_U \lambda_D}{\lambda_U^2} \right)^2 \right) \right] \\ &- 2(\lambda_U - \lambda_B) \left[\lambda_B - \frac{1}{\lambda_B^3} \left(1 + \lambda_B^4 \left(\Delta\bar{\phi} - \frac{\bar{E}_U \lambda_D}{\lambda_U^2} \right)^2 \right) \right] \Bigg\}. \end{aligned} \tag{3.7}$$

In order to identify the optimal cycle through which the maximal energy can be harvested, we optimise the expression for H_g with respect to the variables $\{\lambda_A, \lambda_B, \lambda_D, \Delta\bar{\phi}, \bar{E}_U\}$. Practically, since H_g is a negative quantity, we minimise expression (3.7). To ensure that the optimisation is performed over the set of admissible values within the failure envelope, we perform a constraint minimisation where the constraints are

$$\begin{aligned} &\bar{S}_{22}^A \geq 0, \quad \bar{S}_{11}^D \geq \lambda_D - \frac{1}{\lambda_D^3} - \frac{\bar{E}_{eb}^2}{\lambda_D}, \quad \bar{S}_{11}^D \geq \left(\lambda_D - \frac{1}{\lambda_D} \right), \\ &\Delta\bar{S}_{11}^{D-A} = 0, \quad \Delta\bar{S}_{11}^{B-C} = 0, \\ &0 < \bar{E}_U \leq \bar{E}_{eb}, \\ &1 \leq \lambda_A \leq \lambda_U, \quad 1 \leq \lambda_B \leq \lambda_U, \quad 1 \leq \lambda_D \leq \lambda_U. \end{aligned} \tag{3.8}$$

The constraint minimisation is carried out numerically by application of the Nelder-Mead method (for details on this non-linear optimisation procedure see Appendix A).

An alternative strategy for the constraint optimisation of the gained energy is the method of Lagrange multipliers. As explained in Appendix B, it is possible to formulate the generalized Lagrangian function and the Karush-Kuhn-Tucker (KTT) conditions for the problem by expressing the harvested energy and the constraints defining the failure envelopes in terms of the four characteristic stretches $\lambda_A, \lambda_B, \lambda_C$ and λ_D. Imposing then the stationarity condition for the generalized Lagrangian function, we can determine the optimal configuration of the generator in terms of the stretches.

3.1.2 The invested energy H_i

As for the load-driven cycle depicted in Fig. 2.2, noting that along the path A–B, at constant charge, $\bar{S}_{11}$ is variable according to $\bar{S}_{11}(\lambda) = \lambda - \frac{1}{\lambda^3}(1 + \bar{\omega}^2_{0_{const}})$ and integrating Eq. (2.56) with $\kappa = 1$, the explicit expression of the specific invested energy for a plane-strain loaded DEG is

$$H_i = \frac{1}{2}\left[2(\lambda_C^2 - \lambda_A^2) - (\bar{S}_{11}^B \lambda_C - \bar{S}_{11}^A \lambda_A)\right]. \tag{3.9}$$

Reminding that $\lambda \bar{S}_{11}^{const} = -\frac{1}{\lambda^2} + \lambda^2 - \lambda^2 \bar{\phi}^2$, the invested energy can be written as

$$H_i = \frac{1}{2}\left(\frac{1}{\lambda_C^2} + \lambda_C^2 + \lambda_C^2 \bar{\phi}_C^2\right) - \frac{1}{2}\left(\frac{1}{\lambda_A^2} + \lambda_A^2 + \lambda_A^2 \bar{\phi}_A^2\right). \tag{3.10}$$

Once again, this quantity is written in terms of the parameter set $\{\lambda_A, \lambda_B, \lambda_D, \Delta\bar{\phi}, \bar{E}_U\}$. The resulting expression is

$$\begin{aligned} H_i[\lambda_A, \lambda_B, \lambda_D, \Delta\bar{\phi}, \bar{E}_U] = \frac{1}{2}\Bigg\{ & -\lambda_A^2 + \frac{1}{\lambda_U^2}\left(1 + \bar{E}_U \lambda_D^2 + 2\lambda_U^4\right) \\ & - \frac{1}{\lambda_A^2}\left(1 + \frac{\lambda_B^4}{\lambda_U^4}(\bar{E}_U \lambda_D - \Delta\bar{\phi}\lambda_U^2)^2\right)\Bigg\}. \end{aligned} \tag{3.11}$$

Eq. (3.11) enables to maximise the cycle efficiency η (2.58) within the admissible state region via a numerical constrained maximisation. In the following, numerical analyses are executed in order to detect those cycles that leads to the maximal gained energy and to the highest efficiency.

3.1.3 Influence of the electric breakdown

The electric breakdown is extremely important; first of all, it may or may not influence the definition of the allowable state region. Secondly, even if the electric breakdown contributes to the determination of the failure envelope, it may or may not be a failure involved in the optimal cycle.

Focusing on the influence of the electric breakdown on the allowable state region, a comparison between expressions $(2.36)_1$ and $(2.40)_1$ for the stress according to the failure modes EB and $(S_{22}=0)$ reveals the possible existence of an intersection point at which simultaneous failures may take place. This is possible only if $\bar{E}_{eb} \leq 1$, and the combined failure occurs at stretch ratio $\lambda^* \equiv 1/\sqrt{1-\bar{E}_{eb}^2}$ (see Fig. 3.2a), while if $\bar{E}_{eb} > 1$ the electric breakdown will not affect the failure envelope.

On this basis, by imposing the equality of expressions $(2.37)_2$ and $(2.40)_2$ for the voltage relative to the failure modes λ_U and $(S_{22}=0)$, we can compute the value of $\bar{\omega}_0$ at which the two failure take place at the same time, that is $\hat{\omega}_0 = \sqrt{\lambda_U^2 - 1}$ (see Fig. 3.2b). Then, imposing the equality of equations $(2.36)_2$ and $(2.40)_2$ for the voltage corresponding to the failure modes EB and $(S_{22}=0)$, substituting $\hat{\omega}_0$ and solving with respect to the electric breakdown we find

$$\hat{E}_{eb}(\lambda_U) = \sqrt{\frac{\lambda_U^2 - 1}{\lambda_U^2}}. \tag{3.12}$$

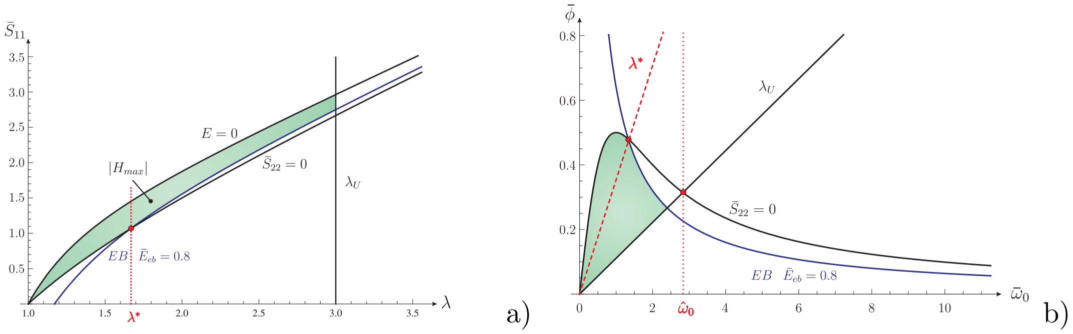

FIGURE 3.2: Region of admissible state for a plane-strain loaded DEG with $\bar{E}_{eb}=0.8$, $\lambda^*=1.667$ and $\hat{\omega}_0=2.828$ on the a) mechanical and b) electrical planes.

Hence, for a given ultimate stretch λ_U, we can distinguish among two cases, to which we will refer in the next Sections:

Case a) if $\bar{E}_{eb} \leq \hat{E}_{eb}$, the failure mode EB must be accounted for in order to define the region of admissible states;

Case b) if $\bar{E}_{eb} > \hat{E}_{eb}$, the optimal cycle lies in the envelope dictated by $(S_{33}=0)$ and λ_U where the EB failure is unattainable.

With respect to Case a, focusing on the influence of the electric breakdown on the optimal cycle, at point D of the cycle one of two independent failure modes may take place, i.e. electric breakdown EB or loss of tensile state ($S_{22} = 0$). The former mode, EB, is trivially associated with the fact that at point D the electric field attains its largest value throughout the cycle. The mode ($S_{22} = 0$) is related to the fact that during the step C–D the membrane is mechanically released (see e.g. Fig. 2.2) and the minimal value of the allowable load is zero. On this basis, we can identify a threshold beyond which the electric breakdown is not attained during the optimal cycle. In fact, this competition between the failure modes leads us to the conclusion that if the electric breakdown limit E_{eb} is smaller than a threshold, then it is the dominant failure mode at D. However, if E_{eb} is larger than this threshold value, then its precise value is irrelevant since only the failure mode ($S_{22} = 0$) will be excited at D. For the sake of the following analysis, in Case a, we distinguish between those optimal cycles in which E_{eb} is attained at point D (failure (i)) and those along which E_{eb} is irrelevant (failure (ii)), as summarised in Tab. 3.1.

	Failure at D
(i)	EB $\cup$ ($S_{22} = 0$)
(ii)	($S_{22} = 0$)

TABLE 3.1: Classification of the optimal cycles for plane-strain load-driven DEGs, according to the relevance of the electric breakdown E_{eb} on the failure at D, cf. Fig. 3.5.

Analysis of the critical threshold value beyond which E_{eb} is irrelevant with respect to the optimal cycle reveals that there is an interplay between this value and the ultimate stretch ratio λ_U (see Fig. 3.5). For the plane-strain generator two classes of materials have been identified: the high ultimate stretch regime (HΛU), characterised by $\lambda_U \geq 2.546$, and the moderate ultimate stretch regime (MΛU), individuated by $\lambda_U < 2.546$. The value of λ_U distinguishing these two regimes has been chosen in analogy with the regime classification obtained for the equibiaxial case, see e.g. Sect. 4.1.3.

3.2 Numerical results

The numerical analysis demonstrates that large values of λ_U lead to an increase in the amount of harvested energy, but, at the same time, to an efficiency decrease. Specifically, as explained later, the maximal efficiency (14.7%) is obtained through a cycle with a moderate maximal stretch $\lambda_U = 1.546$ out of which the extracted energy is $|H_g| = 0.0719$. The maximal harvested energy ($|H_g| = 0.2724$) is harvested through a cycle exploiting the highest allowable stretch ($\lambda_U = 3$), but whose efficiency is just over half of the maximal one (8.2%). This can be understood on grounds of the fact that as the ultimate stretch increases, it is necessary to spend more mechanical work to stretch the dielectric elastomer membrane.

Two values of λ_U, which are characteristic of the high and moderate ultimate stretch regimes (HΛU and MΛU), are investigated in the following.

3.2.1 High ultimate stretch regime (HΛU): $\lambda_U = 3$

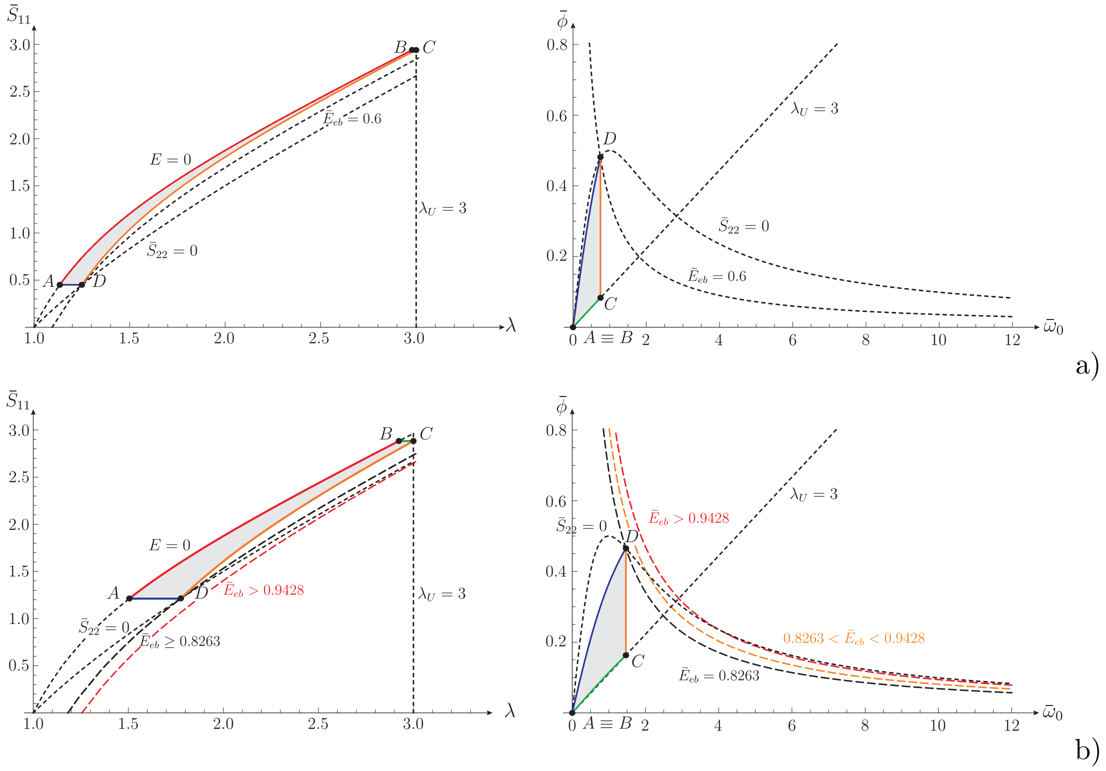

FIGURE 3.3: Optimal cycles on the mechanical and electrical planes for $\lambda_U = 3$ and: a) $\bar{E}_{eb} = 0.6$ and b) $\bar{E}_{eb} \geq 0.8263$.

According to Eq. (3.12), for $\lambda_U = 3$ the electric breakdown is irrelevant beyond the threshold value 0.9428. In Fig. 3.3, two representative harvesting cycles are sketched on the electrical plane, each for a different value of $\bar{E}_{eb}$. The measures of the coloured areas, which are bounded by the four curves representing the four strokes of the cycle, are equal to the amount of energy $|H_g|$ extracted during the harvesting cycle. The dashed curves representing the various failure mechanisms are also shown. In figures 3.3a and b the dashed curves corresponding to the failure modes ($S_{22} = 0$) and λ_U are identical. Thus, the differences between the optimal cycle are solely due to the different values of E_{eb} assumed in each case.

Complementary numerical quantities for the various optimal cycles are listed in Tab. 3.2. For different values of the dielectric strength, the absolute value of the dimensionless gained energy $|H_g|$, the efficiency η (2.58), the dimensionless theoretically achievable energy H_{max}, the effectiveness ζ (2.61) and the dominating failure modes at point D are reported.

[Ref.]	$\bar{E}_{eb}$	$\lvert H_g \rvert$	η	H_{max}	ζ	Failure at D	
Fig. 3.3b	> 0.9428	0.272	8.2%	0.654	41.6%	$(S_{22} = 0)$	(ii) b
Fig. 3.3b	0.9	0.272	8.2%	0.641	42.5%	$(S_{22} = 0)$	(ii) a
Fig. 3.3b	0.8263	0.272	8.2%	0.591	46.1%	EB $\cup$ $(S_{22} = 0)$	(i) a
–	0.8	0.269	7.9%	0.567	47.4%	EB $\cup$ $(S_{22} = 0)$	(i) a
Fig. 3.3a	0.6	0.166	4.6%	0.358	46.3%	EB $\cup$ $(S_{22} = 0)$	(i) a
–	0.5	0.114	3.2%	0.257	42.5%	EB $\cup$ $(S_{22} = 0)$	(i) a
–	0.4	0.073	2.0%	0.169	43.0%	EB $\cup$ $(S_{22} = 0)$	(i) a

TABLE 3.2: Relevant numerical values for optimal cycles associated with a DEG with $\lambda_U = 3$ and different values of $\bar{E}_{eb}$.

3.2.2 Moderate ultimate stretch regime (MΛU): $\lambda_U = 1.8$

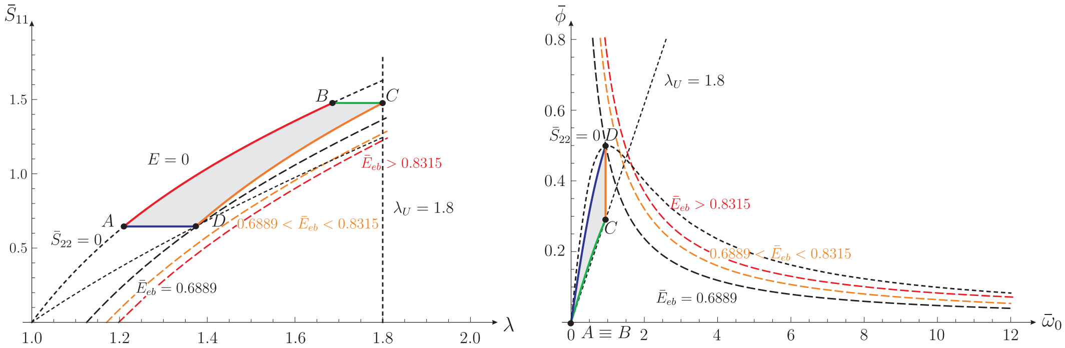

FIGURE 3.4: Optimal cycles on the mechanical and electrical planes for $\lambda_U = 1.8$ and $\bar{E}_{eb} \geq 0.6889$.

According to Eq. (3.12), for $\lambda_U = 1.8$ the electric breakdown is irrelevant beyond the threshold value 0.8315. The numerical analysis, besides, shows that the optimal cycle is not affected by the electric breakdown, when it exceeds the threshold value 0.6889.

Materials with $\lambda_U = 1.8$ and three different electric breakdown limits are shown in Fig. 3.4, the dashed curves are related to the various failure modes. Accordingly, for $\bar{E}_{eb} \geq 0.6889$ the representative optimal harvesting cycle is the same irrespective of the EB failure, as depicted in Fig. 3.4. Similarly to the strategy followed in Subsect. 3.2.1, corresponding relevant numerical values are listed in Tab. 3.3.

[Ref.]	$\bar{E}_{eb}$	$\lvert H_g \rvert$	η	H_{max}	ζ	Failure at D	
Fig. 3.4	> 0.8315	0.272	14.1%	0.242	48.9%	$(S_{22} = 0)$	(ii) b
Fig. 3.4	0.8	0.272	14.1%	0.240	49.4%	$(S_{22} = 0)$	(ii) a
Fig. 3.4	0.6889	0.269	14.1%	0.211	56.3%	EB $\cup$ $(S_{22} = 0)$	(i) a
–	0.6	0.166	12.9%	0.174	61.3%	EB $\cup$ $(S_{22} = 0)$	(i) a
–	0.5	0.114	9.9%	0.129	62.0%	EB $\cup$ $(S_{22} = 0)$	(i) a
–	0.4	0.073	6.7%	0.087	61.3%	EB $\cup$ $(S_{22} = 0)$	(i) a

TABLE 3.3: Relevant numerical values for optimal cycles associated with a DEG with $\lambda_U = 1.8$ and different values of $\bar{E}_{eb}$.

3.3 A universal plot for plane-strain load-driven DEGs

The discussion carried out so far can be conveniently summarized in the two-dimensional plot introduced in Fig. 3.5. The abscissa and the ordinate of the plot correspond the electromechanical limits of the film λ_U and $\bar{E}_{eb}$, respectively.

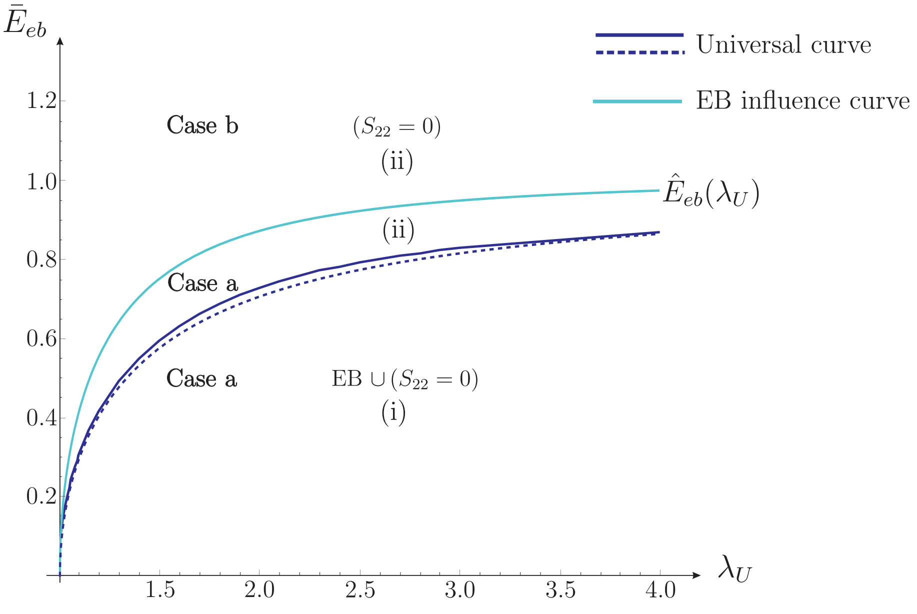

FIGURE 3.5: A universal plot for planar plane-strain load-driven DEGs. The abscissa and the ordinate of the plot correspond to the electromechanical limits of the film λ_U and $\bar{E}_{eb}$, respectively. The dark-blue curve divides the space of materials parameters into two sections, depending on the mode of failure at point D of the optimal harvesting cycle. Beyond the light-blue curve the electric breakdown becomes unimportant in the definition of the allowable state region. The dark-blue dashed curve is related to the analytical prediction (3.14).

In Fig. 3.5, the solid dark-blue curve correspond to the numerical results of the optimisation computed through the algorithm, while the dashed curve is associated with an analytical prediction, as explained in the following of this Section.

In accordance with the qualitative discussion developed in Subsect. 3.1.3, we observe that the dark-blue solid curve splits the two-dimensional $\bar{E}_{eb}$–λ_U space in two. The points below the curve correspond to materials in which the electrical breakdown limit dominates the failure at point D of the optimal cycle. The points above the curve are associated with materials in which the optimal cycle is independent of E_{eb}. At a fixed λ_U, beyond this solid dark-blue curve the energy harvested during the cycle remains constant, as well as the efficiency.

An analytical estimate of the dark-blue curve can be obtained noting that the area of the cycle is visually similar to the rectangle whose height is equal to the potential difference $\delta\bar{\phi}$ among the loss of tension ($S_{22} = 0$) and the ultimate stretch λ_U curve, see e.g. Fig. 3.6.

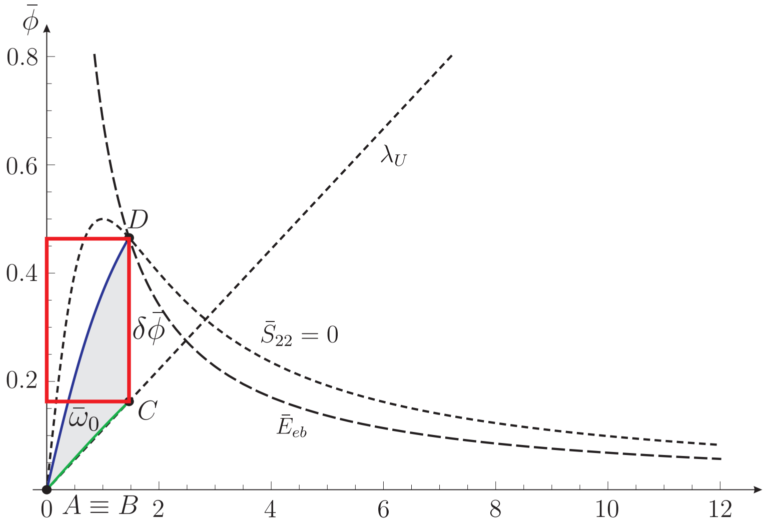

FIGURE 3.6: Approximation of the cycle area through a rectangle whose height is equal to the potential difference $\delta\bar{\phi}$ among the loss of tension ($S_{22} = 0$) and the ultimate stretch λ_U curve.

Thus, we can obtain an analytical expression for the universal curve by maximising the area of the rectangle $\delta\bar{\phi} \times \bar{\omega}_0$ and detecting the value of $\bar{E}_{eb}$ corresponding to this condition. Employing Eq. $(2.40)_2$ and Eq. $(2.37)_2$ to express the voltage difference $\delta\bar{\phi}$, we can find the maximum of the rectangle area by imposing

$$\frac{\mathrm{d}}{\mathrm{d}\bar{\omega}_0}(\delta\bar{\phi}\bar{\omega}_0) = \frac{\mathrm{d}}{\mathrm{d}\bar{\omega}_0}\left(\frac{\bar{\omega}_0^2}{1+\bar{\omega}_0^2} - \frac{\bar{\omega}_0^2}{\lambda_U^2}\right) = 0. \tag{3.13}$$

Solving Eq. (3.13) with respect to $\bar{\omega}_0$, we obtain the value $\bar{\omega}_0^{\bullet} = \sqrt{\lambda_U - 1}$ for which the area of the rectangle (and, hence, the area of the cycle) is maximal. Then, imposing the equality of the voltages relative to the electric breakdown and loss of tension, Eq. $(2.36)_2$ and Eq. $(2.40)_2$, and substituting the value of $\bar{\omega}_0^{\bullet}$, we obtain the value of the dimensionless electric breakdown threshold for which the area of the cycle is maximal

$$\bar{E}_{eb} = \sqrt{\frac{\lambda_U - 1}{\lambda_U}}. \tag{3.14}$$

Eq. (3.14) is the dashed dark-blue curve in Fig. 3.5 and well approximates the numerical result.

The light-blue solid curve represents the limit curve $\hat{E}_{eb}(\lambda_U)$ for the influence on the allowable state region of the electric breakdown failure obtained by employing Eq. (3.12). The points below this light-blue curve correspond to materials in which the electric breakdown is relevant to the definition of the allowable state region (Case a in Subsect. 3.1.3), while points above the curve are associated with materials for which the allowable state region is unresponsive of the breakdown failure (Case b in Subsect. 3.1.3). Hence, beyond the light-blue solid curve, at a fixed λ_U, the maximal energy theoretically extractable by the generator remains constant.

We note that for any given material candidate to be used as a membrane in a DEG subjected to plane-strain loading, the pair $(\lambda_U, \bar{E}_{eb})$ specifies which are the failure mechanisms that limit the optimal cycle. The solid dark-blue curve can be used as a design tool for choosing materials and modes of operations for load driven DEGs. Clearly, an effective design is such that the material parameters are as close as possible to the universal curve.

3.3.1 Electromechanical properties for the best energy and efficiency cycles

The universal dark-blue curve in Fig. 3.5, as said before, is a design tool for the realization of optimal electromechanical transducers. Among the optimal configurations detected by the curve, it is interesting to individuate the optimal couples of electromechanical properties $(\lambda_U,\, \bar{E}_{eb})$ ensuring the best performance with regard to the efficiency, as well as to the harvested energy.

Following the procedure explained at the beginning of this Chapter, we minimise Eq. (3.7) and maximise Eq. (3.11) with respect to the variable set $\{\lambda_A, \lambda_B, \lambda_D, \Delta\bar{\phi}, \bar{E}_U, \bar{E}_{eb}, \lambda_U\}$, imposing the additional constraint $1 < \lambda_U \leq 3$.

The outcome of this procedure is the two pairs of electromechanical properties entailing maximal efficiency and maximal gained energy, see Tab. 3.4.

	λ_U	$\bar{E}_{eb}$	$\lvert H_g \rvert$	η [%]	H_{max}	ζ [%]	Failure
Maximal efficiency	1.546	0.5929	0.072	14.7	0.1713	41.9	(i)a
Maximal energy	3	0.8263	0.272	8.2	0.5908	46.1	(i)a

TABLE 3.4: Electromechanical properties ensuring the best performance in terms of efficiency and harvested energy for a plane-strain load-driven DEG.

Comparing the results, it is evident that the two optimum DEGs, *optimum-efficiency* and *optimum-energy*, are characterised by similar effectiveness. Hence, by exploiting approximately the 40% of the admissible state region, the first DEG operating at MΛU achieves maximal efficiency, whereas the second one harvests maximal energy working at HΛU. It is interesting to note that, even if the energy harvested by the optimum-energy DEG is four times the one produced by the optimum-efficiency device, its efficiency is a half of the value attained by the optimum-efficiency DEG.

For a given value of the dimensionless breakdown threshold $\bar{E}_{eb}$, reminding that it is a function of the material electromechanical properties (μ, ϵ_r) and inverting Eq. (2.33), we can obtain the current electric breakdown E_{eb} and plot it as a function of the shear modulus μ and of the relative permittivity ϵ_r. The plots of the current electric field relative to the optimum-efficiency and to the optimum-energy devices are depicted in Figs. 3.7a and 3.7b for $\mu = 10 \div 1000$ kPa and $\epsilon_r = 2 \div 10$.

The current electric field ranges from 6 to 141 MV/m for the optimum-efficiency device at $\lambda_U = 1.546$ and $\bar{E}_{eb} = 0.5929$ as depicted in Fig. 3.7a, while it ranges from 9 to 196 MV/m for the optimum-energy device at $\lambda_U = 3$ and $\bar{E}_{eb} = 0.8263$, see Fig. 3.7b.

For a fixed couple of electromechanical properties (λ_U, $\bar{E}_{eb}$), on the one hand, the highest the shear modulus μ, the highest the gained energy H_g and, on the other hand, the lower the relative permittivity ϵ_r, the higher the current electric breakdown field E_{eb}. Focusing on the best energy cycle, if the shear modulus is $\mu = 10$, 100, 1000 kPa the gained energy is, respectively, $H_g = 2.724$, 27.240, 272.400 kJ, independently of the relative permittivity ϵ_r. The current breakdown fields corresponding to these values of shear modulus are, respectively, $E_{eb} = 19.64$, 62.09, 196.36 MV/m if $\epsilon_r = 2$, while are $E_{eb} = 9.82$, 31.05, 98.18 MV/m if $\epsilon_r = 8$. These computations show that the effect of an increase in the shear modulus of the material is a directly proportional increase in the energy, while an increment in the relative permittivity results in a proportional decrease in the electric breakdown field (and, generally, in all the other electrical quantities involved).

3.4 Plane-strain DEGs based on commercially available soft DEs

We apply the analysis previously described to two specific commercially available DEs, the acrylic VHB-4910 and the acrylonitrile butadiene rubber (NBR). The VHB-4910, produced by 3M, is a polyacrylate dielectric elastomer available as a pre-cast 1 mm thick polyacrylate adhesive foam. The acrylonitrile butadiene rubber (NBR) is a synthetic

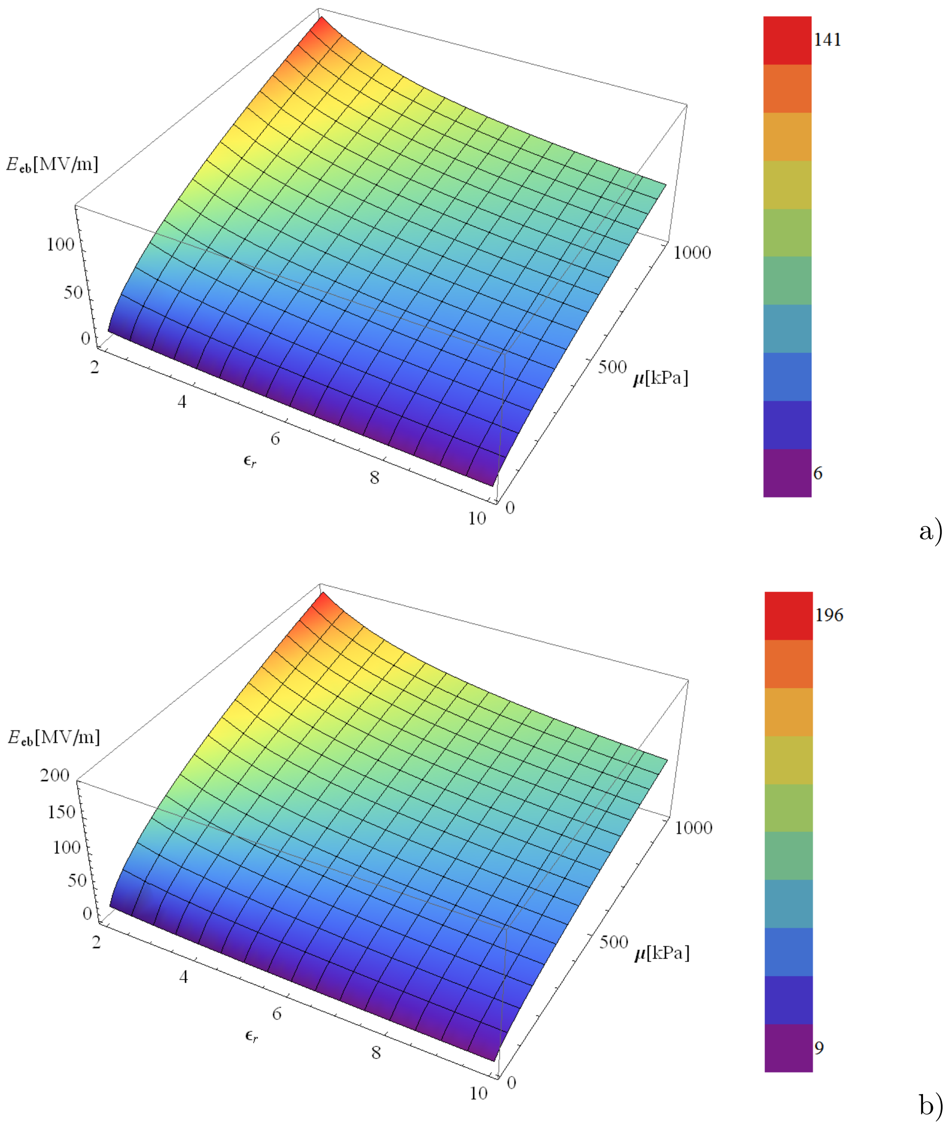

FIGURE 3.7: Values of the electric breakdown strength E_{eb} [MV/m] as a function of the shear modulus μ and of the relative dielectric permittivity ϵ_r for the best performance in terms of: a) efficiency, $\lambda_U = 1.546$ (MΛU) and $\bar{E}_{eb} = 0.5929$, and b) energy, $\lambda_U = 3$ (HΛU) and $\bar{E}_{eb} = 0.8263$.

elastomer, produced by co-polymerization of acrylonitrile (ACN) and butadiene rubber (BR). This rubber exhibits enhanced actuation performance conferred by the presence of the ACN in the range between 18-50% together with vulcanization agents [29]. The pertinent mechanical and electrical properties of the two materials listed in Tab. 3.5 have been reported in [29].

The dielectric strength of these materials, which commonly depends on the applied pre-strain, deserves a particular attention. Thus, we recall that in common EAP applications the films are pre-strained in order to reduce the film thickness and increase the breakdown strength [35, 60]. As an example, the data reported in [35] for VHB-4910 demonstrates that the electric breakdown limit ranges between 20 MV/m in the unstrained state and 218 MV/m in the case of 500% equibiaxial strain. Accordingly, in the sequel two typical values are assumed for the dielectric strength, $E_{eb_1} = 20$ MV/m and $E_{eb_2} = 100$ MV/m.

Material	[Ref.]	μ [kPa]	ϵ_r	$\bar{E}_{eb_1}$	$\bar{E}_{eb_2}$
VHB-4910	[29]	83.4	4.7	0.4468	2.2338
NBR	[29]	1333.4	14	0.1928	0.9642

TABLE 3.5: Physical properties assumed for the elastic dielectrics.

To enable a comparison between the performances of load-driven DEGs based on the these materials, we select the VHB-4910 as a benchmark and determined the maximal stresses ($S_{\max} = S^B_{11}$) attained along the optimal cycles corresponding to all four possible combinations of E_{eb_1}, E_{eb_2}, $\lambda_U = 1.5$ and $\lambda_U = 3$. The four resulting stresses are listed in Tab. 3.6. We note that since the maximal stretch is attained at the end of the electric charging stroke (point C), the stresses corresponding to the larger dielectric breakdown are slightly lower since a larger portion of the allowable stretch is excited electrically. Next, we determined limits on the maximal stretch λ_C of the NBR such that, during the optimal cycles dictated by these stretches and the pair E_{eb_1} and E_{eb_2}, the same maximal stresses will be developed. The resulting stretch ratios for the NBR, together with the harvested energy and the normalized activation potential, are also listed in Tab. 3.6. In this table we also list the material classification (M-C), according to Fig. 3.5. As the shear modulus of the NBR is one order of magnitude larger than that of the acrylic elastomer, the stretches that correspond to similar maximal stresses for the two materials differ of one order of magnitude.

	$E_{eb_1} = 20$ MV/m					$E_{eb_2} = 100$ MV/m				
Material	$S_{\max}$ [kPa]	μH_g [kJ/m^3]	μH_{max} [kJ/m^3]	λ_C	M-C	$S_{\max}$ [kPa]	μH_g [kJ/m^3]	μH_{max} [kJ/m^3]	λ_C	M-C
VHB-4910	132.2	5.49	8.89	1.8	(i)a	123.2	9.88	20.19	1.8	(ii)b
NBR	132.2	0.77	1.25	1.035	(i)a	123.2	0.71	2.19	1.036	(ii)b
VHB-4910	246.3	7.60	17.39	3	(i)a	240.5	22.72	54.56	3	(ii)b
NBR	246.3	1.86	2.37	1.059	(i)a	240.5	2.48	4.92	1.064	(ii)b

TABLE 3.6: The harvested energy-density μH_g, activation electric potential per unit referential thickness $\Delta\phi/h_0$ and material classification M-C, determined for the optimal cycles according to the dielectric strength limits and the maximal stretch ratios λ_C determined for the maximum stresses $S_{\max}$.

At first glimpse we deduce from Tab. 3.6 that the amounts of energy extractable from the VHB-4910 are an order of magnitude larger than those available for the NBR (when the load or the traction on the DEG are specified). This is due to the extensibility of the former and in spite of the fact that the dielectric constant of the VHB-4910 is substantially smaller than that of the NBR.

Another important observation concerns the importance of the classification of the materials. In particular, we note the differences in the energies harvested from the VHB-4910. In the first line of Tab. 3.6 the energy μH_g associated with the VHB-4910 for smaller dielectric strength is comparable with the one extracted from the material whose dielectric strength is 5 times larger. This fact occurs because the material with larger dielectric breakdown is associated with Case b in Fig. 3.5, according to which this larger dielectric strength does not participate in the definition of the allowable state region and hence it is not reached during the optimal cycle (failure (ii)), so that the potential of the material remains unexpressed. Along the third line of Tab. 3.6, where VHB-4910 with larger stretchable domain is considered, the situation is somewhat different: the energy extracted from the material with larger E_{eb} is approximately three times the one extracted from the one with smaller E_{eb}. This is due to the fact that the pair $(\lambda_U, \bar{E}_{eb})$ for the material with larger dielectric breakdown is closer to the universal curve shown in Fig. 3.5, suggesting that this material is closer to the optimal balance between the ultimate stretch ratio and the dielectric breakdown.

Chapter 4

Optimisation of an ideal DEG in equibiaxial loading mode

This Chapter focuses on the performance optimisation of the ideal hyperelastic parallel plate generator deforming equibiaxially presented in Subsect. 2.3.2. The membrane is deformed in-plane by equal forces applied along x_1 and x_2 directions, as depicted in Fig. 4.1.

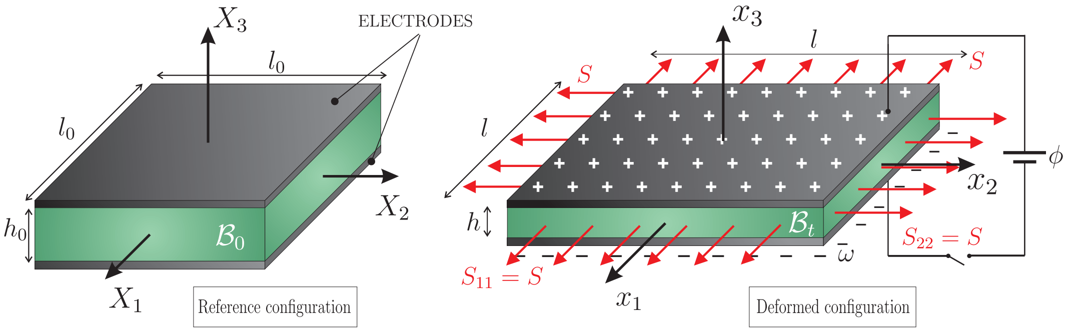
X_3
ELECTRODES
l_0
l_0
h_0
$\mathcal{B}_0$
X_2
X_1
Reference configuration
x_3
l
S
S
l
ϕ
x_2
h
$\mathcal{B}_t$
ω
$S_{22} = S$
$S_{11} = S$
x_1
Deformed configuration

FIGURE 4.1: Reference and deformed configurations of a soft planar DE generator with undeformed dimensions ($l_0 \times l_0 \times h_0$) subjected to equibiaxial loading: as a result of the deformation, the current dimensions are $l = l_1 = l_2 = l_0\lambda$ and $h = h_0\lambda^{-2}$.

In the following, employing the same procedure illustrated in Chap. 3, we optimise the performance of this ideal generator by determining the optimal cycle, within the admissible state region, out of which the maximal energy can be harvested. Details about the modes of failure have been introduced in Subsect. 2.6.2.

4.1 Constrained optimisation problem for equibiaxial loading mode

Here, we specialise expressions (2.55) of the generated energy and (2.56) of the invested energy for the equibiaxial loading mode. The possible failures of the generator will be taken into account as constraints to the cycle optimisation. Particular attention will be paid to the electric breakdown and its influence on both the allowable state region and the failure characterising the optimal cycle.

4.1.1 The harvested energy H_g

With respect to the load-driven harvesting cycle illustrated in Sect. 2.5, reminding that S is constant along both paths B–C and A–D, letting $\bar{S}^{const} = \bar{S}^B$ along the former and $\bar{S}^{const} = \bar{S}^A$ along the latter, it is convenient to express the dimensionless potential $\bar{\phi}$ as a function of the stretch λ and the constant stress $\bar{S}^{const}$. Thus, employing $(2.21)_1$, along the two steps

$$\bar{\phi}(\lambda) = \sqrt{\lambda^{-2} - \lambda^{-8} - \bar{S}^{const}\lambda^{-3}}. \tag{4.1}$$

Moreover, Eq. $(2.21)_2$ allows us to evaluate the differential $\mathrm{d}\bar{\omega}_0$ in terms of the same pair

$$\mathrm{d}\bar{\omega}_0 = \mathrm{d}[\bar{\phi}(\lambda)\lambda^4] = \frac{6\lambda - 5\bar{S}^{const}}{2\sqrt{\lambda^{-2} - \lambda^{-8} - \bar{S}^{const}\lambda^{-3}}}\mathrm{d}\lambda. \tag{4.2}$$

Hence, the first integral in Eq. (2.55) can be evaluated explicitly

$$\int_B^C \bar{\phi}\,\mathrm{d}\bar{\omega}_0 = \int_{\lambda_B}^{\lambda_C} \left(3\lambda - \frac{5}{2}\bar{S}^{const}\right)\mathrm{d}\lambda = \left|\frac{1}{2}\lambda(3\lambda - 5\bar{S}^{const})\right|_{\lambda_B}^{\lambda_C}. \tag{4.3}$$

The second integral can be determined in a similar manner. Summation of the two integrals leads to the explicit expression for the dimensionless gained energy, namely

$$H_g = \frac{1}{2}\left[3(\lambda_C^2 - \lambda_B^2) - 5\bar{S}^B(\lambda_C - \lambda_B) + 3(\lambda_A^2 - \lambda_D^2) - 5\bar{S}^A(\lambda_A - \lambda_D)\right]. \tag{4.4}$$

Since $\lambda\bar{S}^{const} = -\frac{1}{\lambda^4} + \lambda^2 - \lambda^4\bar{\phi}^2$, Eq. (4.4) can be written as

$$\begin{aligned} H_g =& \frac{1}{2}\left(\frac{1}{\lambda_A^4} + 2\lambda_A^2 + \lambda_A^4\bar{\phi}_A^2\right) - \frac{1}{2}\left(\frac{1}{\lambda_D^4} + 2\lambda_D^2 + \lambda_D^4\bar{\phi}_D^2\right) - 2\bar{S}^A(\lambda_A - \lambda_D) \\ &+ \frac{1}{2}\left(\frac{1}{\lambda_C^4} + 2\lambda_C^2 + \lambda_C^4\bar{\phi}_C^2\right) - \frac{1}{2}\left(\frac{1}{\lambda_B^4} + 2\lambda_B^2 + \lambda_B^4\bar{\phi}_B^2\right) - 2\bar{S}^B(\lambda_C - \lambda_B). \end{aligned} \tag{4.5}$$

The same result can be obtained from Eq. (2.52) by employing the dimensionless stress $\bar{\boldsymbol{S}}$ and the strain energy function (2.14) divided by the shear modulus, i.e $W(\boldsymbol{F}, \boldsymbol{E}^0)/\mu$.

In addition, according to Eq. (2.21) and similarly to Subsect. 3.1.1, we can impose the equalities

$$\lambda_C = \lambda_U, \quad \bar{\phi}_D = \bar{E}_U \lambda_D^{-2}, \quad \Delta\bar{\phi} = \bar{\phi}_C - \bar{\phi}_B, \tag{4.6}$$

through relations (2.32).

Upon substitution of relations (4.6) into expression (4.5), we end up with the following expression for harvested energy as a function of the parameters set $\{\lambda_A, \lambda_B, \lambda_D, \Delta\bar{\phi}, \bar{E}_U\}$,

$$\begin{aligned} H_g(\lambda_A, \lambda_B, \lambda_D, \Delta\bar{\phi}, \bar{E}_U) =& \frac{1}{2}\Bigg\{ \frac{1}{\lambda_A^4} - \frac{1}{\lambda_D^4} + \frac{1}{\lambda_U^4} - \frac{1}{\lambda_B^4} + 2(\lambda_A^2 - \lambda_D^2 + \lambda_U^2 - \lambda_B^2) \\ &+ \bar{E}_U \left(\frac{\lambda_D^4}{\lambda_U^4} - 1 \right) + \lambda_B^4 \left(\frac{\lambda_B^4}{\lambda_A^4} - 1 \right) \left(\Delta\bar{\phi} - \frac{\bar{E}_U \lambda_D^2}{\lambda_U^4} \right)^2 \\ &- 4(\lambda_A - \lambda_D) \left[\lambda_A - \frac{1}{\lambda_A^5} \left(1 + \lambda_B^8 \left(\Delta\bar{\phi} - \frac{\bar{E}_U \lambda_D^2}{\lambda_U^4} \right)^2 \right) \right] \\ &- 4(\lambda_U - \lambda_B) \left[\lambda_B - \frac{1}{\lambda_B^5} \left(1 + \lambda_B^8 \left(\Delta\bar{\phi} - \frac{\bar{E}_U \lambda_D^2}{\lambda_U^4} \right)^2 \right) \right] \Bigg\}. \end{aligned} \tag{4.7}$$

In order to identify the optimal cycle, through which the maximal energy can be harvested, we optimise the expression for H_g with respect to the variables $\{\lambda_A, \lambda_B, \lambda_D, \Delta\bar{\phi}, \bar{E}_U\}$. Practically, since H_g is a negative quantity, we minimise expression (4.7). To ensure that the optimisation is performed over the set of admissible values within the failure envelope, we perform a constraint minimisation where the constraints are

$$\begin{aligned} &\bar{S}_A \geq 0, \quad \bar{S}_D \geq \lambda_D - \frac{1}{\lambda_D^5} - \frac{\bar{E}_{eb}^2}{\lambda_D}, \quad \bar{S}_D \geq \frac{2}{3}\left(\lambda_D - 4\frac{1}{\lambda_D^5} \right), \\ &\Delta\bar{S}_{D-A} = 0, \quad \Delta\bar{S}_{B-C} = 0, \\ &0 < \bar{E}_U \leq \bar{E}_{eb}, \\ &1 \leq \lambda_A \leq \lambda_U, \quad 1 \leq \lambda_B \leq \lambda_U, \quad 1 \leq \lambda_D \leq \lambda_U. \end{aligned} \tag{4.8}$$

The constraint minimisation is carried out numerically by application of the Nelder-Mead algorithm.

4.1.2 The invested energy H_i

As for the load-driven cycle displayed in Fig. 2.2, reminding that along the path A–B the charge is constant while the stress varies according to $\bar{S}(\lambda) = \lambda - \frac{1}{\lambda^5}(1 + \bar{\omega}_{0_{const}}^2)$ and integrating Eq. (2.56) with $\kappa = 2$, the explicit expression of the specific invested energy for an equibiaxially loaded DEG is

$$H_i = \frac{1}{2}\left[3(\lambda_C^2 - \lambda_A^2) - (\bar{S}^B\lambda_C - \bar{S}^A\lambda_A)\right]. \tag{4.9}$$

Reminding that $\lambda\bar{S}^{const} = -\frac{1}{\lambda^4} + \lambda^2 - \lambda^4\bar{\phi}^2$, the invested energy can be written as

$$H_i = \frac{1}{2}\left(\frac{1}{\lambda_C^4} + 2\lambda_C^2 + \lambda_C^4\bar{\phi}_C^4\right) - \frac{1}{2}\left(\frac{1}{\lambda_A^4} + 2\lambda_A^2 + \lambda_A^4\bar{\phi}_A^4\right). \tag{4.10}$$

The same result of Eq. (4.10) can be obtained from Eq. (2.53) by employing the strain energy function (2.14) divided by the shear modulus, i.e. $W(\boldsymbol{F}, \boldsymbol{E}^0)/\mu$. Once again, this quantity is written in terms of the parameter set $\{\lambda_A, \lambda_B, \lambda_D, \Delta\bar{\phi}, \bar{E}_U\}$. The resulting expression is

$$\begin{aligned} H_i[\lambda_A, \lambda_B, \lambda_D, \Delta\bar{\phi}, \bar{E}_U] = \frac{1}{2}\Bigg\{ & -2\lambda_A^2 + \frac{1}{\lambda_U^4}\left(1 + \bar{E}_U^2\lambda_D^4 + 2\lambda_U^6\right) \\ & - \frac{1}{\lambda_A^4}\left(1 + \frac{\lambda_B^8}{\lambda_U^8}(\bar{E}_U\lambda_D^2 - \Delta\bar{\phi}\lambda_U^4)^2\right)\Bigg\}. \end{aligned} \tag{4.11}$$

Eq. (4.11) enables to maximise the cycle efficiency η (2.58) within the admissible state region via a numerical constrained maximisation. In the following numerical analyses are executed in order to detect those cycles that leads to the maximal gained energy and to the highest efficiency.

4.1.3 Influence of the electric breakdown

As introduced in Subsect. 3.1.3, the electric breakdown is an extremely important parameter. As before, it may or may not affect the allowable state region. Furthermore, even if the electric breakdown contributes to the outlining of the failure envelope, it may or may not have influence on the optimal cycle.

Focusing on the failure mode stresses, the possible existence of two intersection points, λ^* and λ^{**}, at which simultaneous failures may take place, can be assessed. Specifically, these points can be detected by comparing expressions $(2.44)_1$ and $(2.49)_1$, related to EB and $(S = 0)$, and expressions $(2.44)_1$ and $(2.46)_1$, associated to EB and EMI. Therefore, as in the case of plane-strain loading, we can determine a limit curve for the electric breakdown influence on the allowable state region.

When the electric breakdown strength $\bar{E}_{eb}$ is lower than 1.091, only the intersection point λ^* between loss of tensile state $(S = 0)$ and electric breakdown EB exists and at this point simultaneous failures may take place. By imposing the equality of expressions

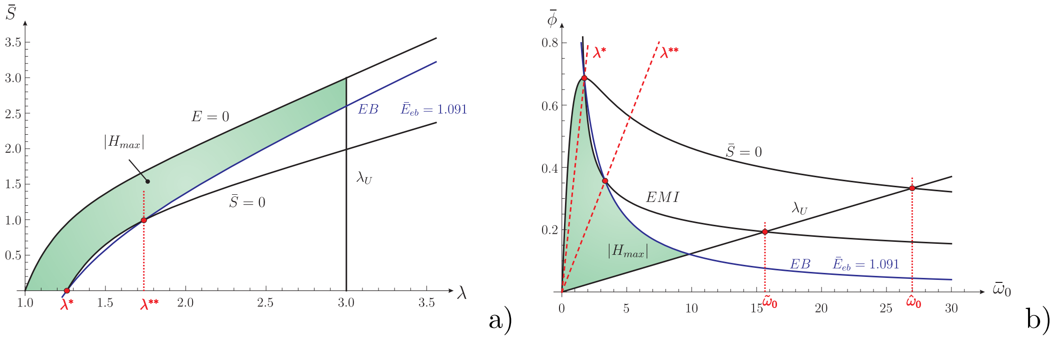

FIGURE 4.2: Region of admissible state for an equibiaxially loaded DEG with $\bar{E}_{eb} = 1.0912$, $\lambda^* = 1.259$, $\lambda^{**} = 1.739$, $\tilde{\omega}_0 = 15.642$ and $\hat{\omega}_0 = 26.981$ on the a) mechanical and b) electrical planes.

$(2.47)_2$ and $(2.49)_2$ for the voltage relative to the failure modes λ_U and $(S = 0)$, we can compute the value of $\bar{\omega}_0$ at which the two failures take place at the same time, that is $\hat{\omega}_0 = \sqrt{\lambda_U^6 - 1}$ (see Fig. 4.2). Then, imposing the equality of equations $(2.44)_2$ and $(2.49)_2$ for the voltage corresponding to the failure modes EB and $(S = 0)$, substituting $\hat{\omega}_0$ and solving with respect to the electric breakdown we find Eq. (4.12a), which is valid until $\lambda_U \leq 1.259$.

If the electric breakdown strength $\bar{E}_{eb}$ is equal to 1.091, the intersection between the electric breakdown EB and the loss of tensile stress $(S = 0)$ occurs at $\lambda^* = 1.259$ and that between the electric breakdown EB and the electromechanical instability EMI takes place at $\lambda^{**} = 1.739$, as depicted in Fig. 4.2. Therefore, for $\bar{E}_{eb} = 1.091$ the electric breakdown does not influence the allowable state region if the ultimate stretch is in the range between 1.259 and 1.739 (4.12b).

When the electric breakdown strength $\bar{E}_{eb}$ is larger than 1.091, only the intersection point λ^{**} between electromechanical instability EMI and electric breakdown EB takes place. By imposing the equality of expressions $(2.47)_2$ and $(2.46)_2$ for the voltage relative to the failure modes λ_U and EMI, we can compute the value of $\bar{\omega}_0$ at which the two failures occur at the same time, that is $\tilde{\omega}_0 = \sqrt{(\lambda_U^6 + 5)/3}$ (see Fig. 4.2). Then, imposing the equality of equations $(2.44)_2$ and $(2.46)_2$ for the voltage corresponding to the failure modes EB and EMI, substituting $\tilde{\omega}_0$ and solving with respect to the electric breakdown we find Eq. (4.12c), which is valid if $\lambda_U \geq 1.739$. Overall, the limit curve for the electric breakdown influence on the allowable state region can be explicit as

$$\hat{E}_{eb}(\lambda_U) = \begin{cases} \sqrt{\dfrac{\lambda_U^6 - 1}{\lambda_U^4}} & \lambda_U \leq 1.259, \quad (4.12a) \\ 1.091 & 1.259 \leq \lambda_U \leq 1.739, \quad (4.12b) \\ \sqrt{\dfrac{\lambda_U^6 + 5}{3\lambda_U^4}} & \lambda_U \geq 1.739. \quad (4.12c) \end{cases}$$

As a consequence, as shown in Subsect. 3.1.3, for a given ultimate stretch λ_U we can distinguish between the two main cases, to which we will refer in the following:

Case a) if $\bar{E}_{eb} \leq \hat{E}_{eb}$, the failure mode EB must be accounted for in order to define the region of admissible states;

Case b) if $\bar{E}_{eb} > \hat{E}_{eb}$, the optimal cycle lies in the envelope dictated by $(S = 0)$, EMI and λ_U where the EB failure is unattainable.

With respect to Case a, focusing on the influence of the electric breakdown on the optimal cycle, one of three independent failure modes may take place at point D: electric breakdown EB, electromechanical instability EMI or loss of tensile state $(S = 0)$. The first two modes, EB and EMI, are trivially associated with the fact that at point D the electric field attains its largest value throughout the cycle. The mode $(S = 0)$ is related to the fact that during the step C–D the membrane is mechanically released (see e.g. Fig.2.2) and we require not to have a compressive stress. A conclusion following this competition between the failure modes is that we can identify a threshold beyond which the electric breakdown is irrelevant with respect to the optimal cycle. On this basis, if the electric breakdown limit E_{eb} is smaller than a threshold, then it is the dominant failure mode at D. However, if E_{eb} is larger than this value, then it is irrelevant since a different mode set the failure at D. For the sake of the following analysis we distinguish between those optimal cycles in which E_{eb} is attained at point D (failures (i), (iv), (v) and (vi)) and those along which E_{eb} is irrelevant (failures (ii), (iii) and (vii)), as summarised in Tab. 4.1.

Analysis of the critical threshold value beyond which E_{eb} is irrelevant with respect to the optimal cycle reveals that there is a fine interplay between this value and the ultimate stretch ratio λ_U. Thus, for the equibiaxial generator, three classes of materials can be identified as follows (see Fig. 4.6):

- For *high ultimate stretch* (HΛU) materials ($\lambda_U \geq 2.546$), the dimensionless threshold value is:

$$\bar{E}_{eb} \cong 0.453\lambda_U + 0.035. \quad (4.13)$$

	Failure at D
(i)	EB $\cup$ $(S_{22} = 0)$
(ii)	$(S_{22} = 0)$
(iii)	$(S_{22} = 0) \cup$ EMI
(iv)	EB
(v)	EB $\cup$ $(S_{22} = 0) \cup$ EMI
(vi)	EB $\cup$ EMI
(vii)	EMI

TABLE 4.1: Classification of the optimal cycles for equibiaxial load-driven DEGs, according to the relevance of the electric breakdown E_{eb} on the failure at D, cf. Fig. 4.6.

- For *moderate ultimate stretch* (MΛU) materials ($1.468 < \lambda_U < 2.546$), the dimensionless threshold value is:

$$\bar{E}_{eb} = 1.091. \tag{4.14}$$

- For *low ultimate stretch* (LΛU) materials ($1 < \lambda_U \leq 1.468$), the dimensionless threshold value is:

$$\bar{E}_{eb} \cong -56.480\lambda_U^4 + 288.170\lambda_U^3 - 551.541\lambda_U^2 + 470.863\lambda_U - 150.895. \tag{4.15}$$

Equalities (4.13) and (4.15) are obtained by fitting points determined numerically, while equality (4.14) is a rigorous analytical result.

Four values of λ_U that are characteristic of the identified regimes are investigated in next Section. We anticipate that the complete overview of all discussed cases is sketched in Fig. 4.6.

4.2 Numerical results

The numerical analysis demonstrates that large values of λ_U lead to an increase in the amount of harvested energy, but, at the same time, to an efficiency decrease. Moreover, in the cases analysed in this work, the cycle optimising the gained energy H_g also maximises the efficiency η. Specifically, as explained later, the maximal efficiency (43.75%) is obtained through a cycle with a moderate maximal stretch $\lambda_U = 1.563$, out of which the extracted energy is $|H_g| = 0.559$. The maximal harvested energy ($|H_g| = 1.145$) is harvested through a cycle exploiting the highest allowable stretch ($\lambda_U = 3$), but whose efficiency is less than a half of the maximal one (17.2%). This can be understood on account of the fact that, as the ultimate stretch increases, it is necessary to spend more mechanical work to stretch the dielectric elastomer membrane. We also note that, in all the cases examined in this work, it was found that the optimal cycles are achieved when the initial stretching (step A–B) is carried out with zero charge on the electrodes.

4.2.1 High ultimate stretch regime (HΛU): $\lambda_U = 3$

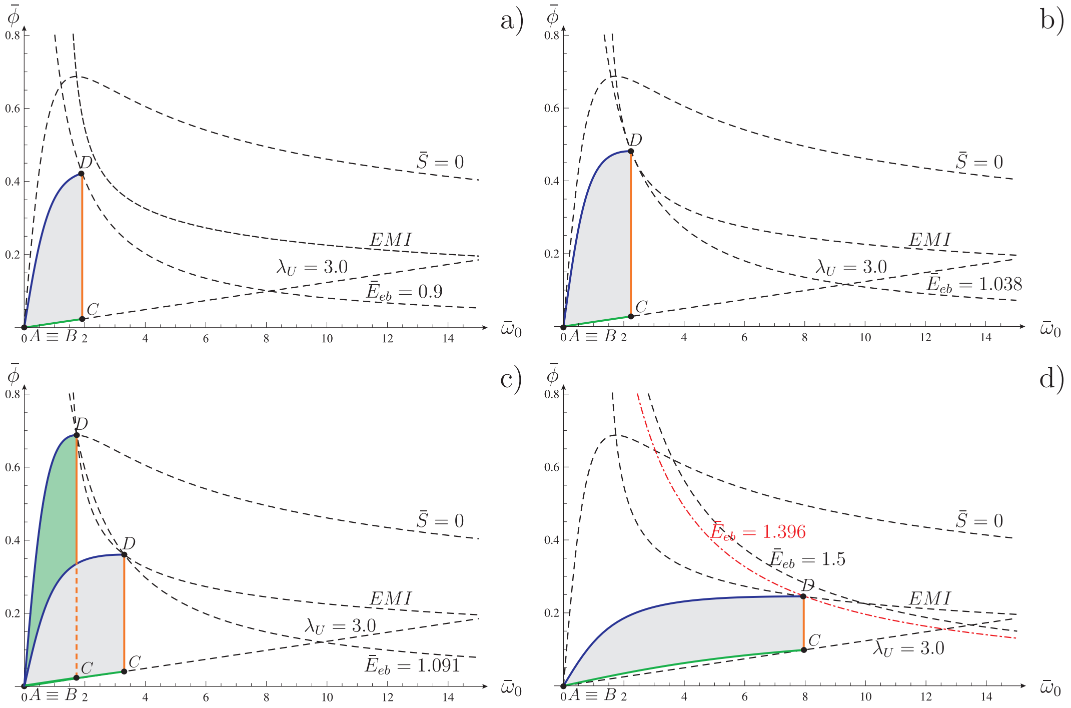

FIGURE 4.3: Optimal cycles for $\lambda_U = 3$ and: a) $\bar{E}_{eb} = 0.9$, b) $\bar{E}_{eb} = 1.038$, c) $\bar{E}_{eb} = 1.091$, and d) $\bar{E}_{eb} \geq 1.396$.

For $\lambda_U = 3$, according to Eq. (4.12c), the electric breakdown is not part of the failure envelope beyond the value 1.739 and, according to inequality (4.13), already beyond the threshold value 1.396 the electric breakdown is irrelevant with respect to the cycle failure.

In Fig. 4.3, four representative harvesting cycles are sketched on the thermodynamic electrical plane, each for a different value of $\bar{E}_{eb}$. In these figures are also shown dashed curves that represent the various failure mechanisms. In all four figures the dashed curves corresponding to the failure modes EMI, $(S = 0)$ and λ_U are identical. Thus, the differences between the optimal cycle are solely due to the different values of E_{eb} assumed in each case.

Complementary numerical quantities for the various optimal cycles are listed in Tab. 4.2. For different dielectric strengths, the stretch λ_D, the absolute value of the dimensionless gained energy $|H_g|$, the efficiency η (2.58), the dimensionless theoretically achievable energy H_{max}, the effectiveness ζ, defined by Eq. (2.61), and the dominating failure modes at point D are presented.

Fig. 4.3a corresponds to $\bar{E}_{eb} = 0.9$ and, since it is a relatively small breakdown field, this is the mode which sets the failure at point D and confines the intensity of the electric

[Ref.]	$\bar{E}_{eb}$	$\lvert H_g \rvert$	η	H_{max}	ζ	Failure at D	
–	≥ 1.738	1.145	17.2%	3.077	37.2%	EMI	(vii)b
Fig. 4.3d	1.5	1.145	17.2%	2.966	38.6%	EMI	(vii)a
Fig. 4.3d	1.396	1.145	17.2%	2.852	40.1%	EB $\cup$ EMI	(vi)a
Fig. 4.3c	1.091	0.863	11.4%	2.303	37.5%	EB $\cup$ EMI $\cup$ $(S = 0)$	(v)a
Fig. 4.3c	1.091	0.869	12.0%	2.303	37.7%	EB $\cup$ EMI	(vi)a
–	1.050	0.803	10.7%	2.192	36.6%	EB $\cup$ EMI high $\bar{\phi}$	(via)
–	1.050	0.809	10.9%	2.192	36.9%	EB $\cup$ EMI low $\bar{\phi}$	(vi)a
Fig. 4.3b	1.038	0.789	10.6%	2.152	36.6%	EB $\cup$ EMI	(vi)a
Fig. 4.3a	0.9	0.551	7.5%	1.661	33.2%	EB	(iv)a

TABLE 4.2: Relevant numerical values for optimal cycles associated with a DEG with $\lambda_U = 3$ and different values of $\bar{E}_{eb}$.

field. However, starting from $\bar{E}_{eb} = 1.038$, which is the case shown in Fig. 4.3b, the electromechanical instability EMI must be accounted for. Thus, the curves corresponding to the failure modes EB and EMI intersect, and the optimal cycle is the one in which point D is at the intersection point. In the range $1.038 < \bar{E}_{eb} \leq 1.091$, the EB curve intersects the EMI curve twice below the loss of tension threshold curve $(S = 0)$. The extremal case $\bar{E}_{eb} = 1.091$ is shown in Fig. 4.3c. In this range of $\bar{E}_{eb}$ there are two possible cycles that are limited by the pair of curves EMI and EB. In Fig. 4.3c, the areas bounded by the two harvesting cycles are represented by two different colours. Remarkably, for any $\bar{E}_{eb}$ sitting in this range the amount of energy harvested from these two cycles is nearly the same, and their efficiencies are almost identical too. When $\bar{E}_{eb} = 1.091$ [Fig. 4.3c], the upper intersection point lies on the curve $(S = 0)$, and point D of the corresponding cycle coincide with this triple intersection point. In comparison, the cycle involving the low intersection point (the light-grey area) provides a similar amount of energy, but its efficiency is slightly lower (see Tab. 4.2). At values of the non-dimensional electric breakdown larger than 1.091, the optimal cycle is governed by a single intersection point of the curves for the EMI and the EB failures. The amount of energy gained monotonically increases with $\bar{E}_{eb}$ up to 1.396. This limiting case is depicted in Fig. 4.3d with the aid of the dashed-dotted red curve. Beyond this limit, the maximal harvested energy is independent of the material electrical breakdown limit, and the failure mode confining the electric field at D is the electromechanical instability. The dashed curve corresponding to $\bar{E}_{eb} = 1.5$ is also shown in this figure to highlight the fact that the optimal cycle is independent of $\bar{E}_{eb}$.

4.2.2 Moderate ultimate stretch regime (MΛU): $\lambda_U = 2.1$ and $\lambda_U = 1.8$

For MΛU materials, the electric breakdown is not part of the failure envelope beyond the value defined by Eq. (4.12c) for $1.759 \leq \lambda_U \leq 2.546$ and by Eq. (4.12b) for $1.468 \leq \lambda_U \leq 1.759$.

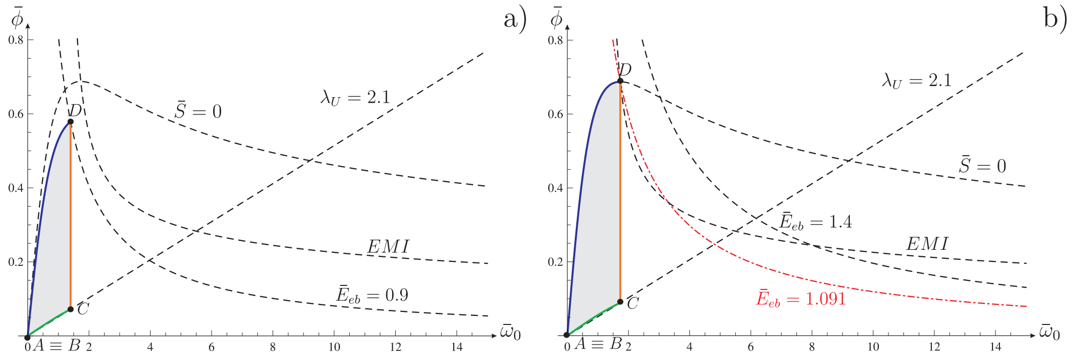

FIGURE 4.4: Optimal cycles for $\lambda_U = 2.1$ and: a) $\bar{E}_{eb} < 1.091$ and b) $\bar{E}_{eb} \geq 1.091$.

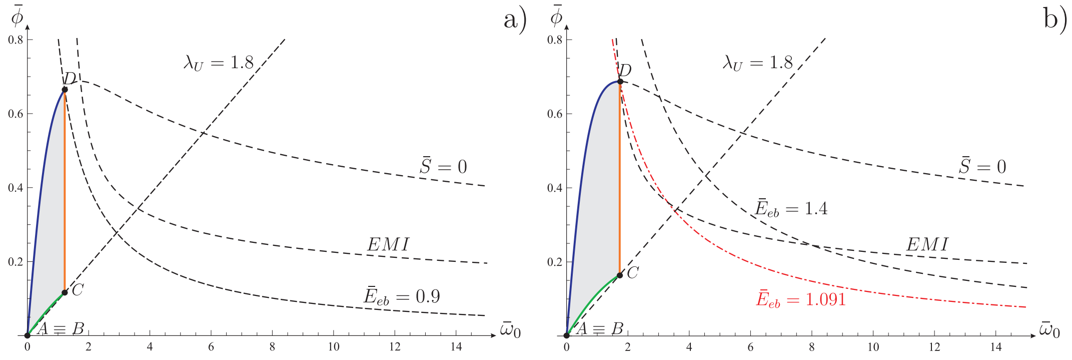

FIGURE 4.5: Optimal cycles for $\lambda_U = 1.8$ and: a) $\bar{E}_{eb} < 1.091$ and b) $\bar{E}_{eb} \geq 1.091$.

We recall that for the class of MΛU materials (i.e., $1.468 < \lambda_U < 2.356$), the optimal cycle is independent of the electric breakdown limit whenever $\bar{E}_{eb} > 1.091$. For materials with $\bar{E}_{eb} < 1.091$ we further distinguish between those with $1.985 \leq \lambda_U < 2.356$ and $1.468 < \lambda_U \leq 1.985$. Accordingly, in Figs. 4.4 and 4.5 four representative optimal harvesting cycles are shown with the corresponding dashed curves associated with the various failure modes. Materials belonging to the first subgroup, with $\lambda_U = 2.1$ and electric breakdown limits $E_{eb} = 0.9$ and 1.4, are shown in Figs. 4.4a and b, respectively. Materials from the second subgroup, with $\lambda_U = 1.8$ and similar electric breakdown limits, are shown in Figs. 4.5a and b. According to Eq. (4.12c), the electric breakdown does not contribute to the definition of the failure envelope beyond the threshold value 1.247 for $\lambda_U = 2.1$ and beyond the value 1.113 for $\lambda_U = 1.8$. In a similar way to the one followed in Subsect. 4.2.1, corresponding relevant numerical values are listed in Tabs. 4.3 and 4.4.

A comparison between Figs. 4.4a and 4.5a reveals that in the former case, where the material ultimate stretch is higher, the electric breakdown limit is the one restricting the intensity of the electric field at point D. In the second case, with a smaller ultimate stretch, point D of the optimal cycle is located at the intersection of the curves for the

[Ref.]	$\bar{E}_{eb}$	$\lvert H_g \rvert$	η	H_{max}	ζ	Failure at D	
Fig. 4.4b	≥ 1.247	0.798	26.5%	1.514	52.7%	EMI $\cup$ ($S = 0$)	(iii)b
Fig. 4.4b	1.091	0.798	26.5%	1.453	54.9%	EB $\cup$ EMI $\cup$ ($S = 0$)	(v)a
Fig. 4.4a	0.9	0.495	16.7%	1.083	45.7%	EB	(iv)a

Table 4.3: Relevant numerical values for optimal cycles associated with a DEG with $\lambda_U = 2.1$ and different values of $\bar{E}_{eb}$.

[Ref.]	$\bar{E}_{eb}$	$\lvert H_g \rvert$	η	H_{max}	ζ	Failure at D	
Fig. 4.5b	≥ 1.113	0.717	37.0%	1.088	65.9%	EMI $\cup$ ($S = 0$)	(iii)b
Fig. 4.5b	1.091	0.717	37.0%	1.086	66.0%	EB $\cup$ EMI $\cup$ ($S = 0$)	(v)a
Fig. 4.5a	0.9	0.456	24.5%	0.833	54.7%	EB $\cup$ ($S = 0$)	(i)a

Table 4.4: Relevant numerical values for optimal cycles associated with a DEG with $\lambda_U = 1.8$ and different values of $\bar{E}_{eb}$.

EB and the ($S = 0$) failure modes. For values of E_{eb} larger than 1.091 the optimal cycles for the MΛU materials are qualitatively identical. This can be perceived from Figs. 4.4b and 4.5b where the curves corresponding to $E_{eb} = 1.091$ (the red dashed-dotted curves) passes through the intersection points of the failure curves EMI and ($S = 0$). Thus, during the optimal cycle, the intensity of the electric field at point D is restricted by electromechanical instability at zero transverse tension in the membrane. The gained energy is therefore independent of the value of $\bar{E}_{eb}$.

4.2.3 Low ultimate stretch regime (LΛU): $\lambda_U = 1.4$

For the class of LΛU materials (i.e., $\lambda_U < 1.468$), the electric breakdown is relevant in the definition of the failure envelope beyond the threshold defined by Eq. (4.12b) for $1.259 \leq \lambda_U \leq 1.468$ and by Eq. (4.12a) for $\lambda_U \leq 1.259$. Moreover, for this class of materials, the optimal cycle is independent of the electric breakdown limit whenever $\bar{E}_{eb}$ is larger than the threshold value given in Eq. (4.15). The plots that correspond to the two classes of materials are qualitatively identical to the ones shown in Fig. 4.5. Thus, at smaller values of $\bar{E}_{eb}$ point D of the optimal cycle is dictated by loss of the tensile state and electric breakdown EB $\cup$ ($S = 0$), while for values of electric breakdown limit that satisfy inequality (4.15) point D of the optimal cycle is limited by the ($S = 0$) failure curve. A few representative numerical values for a material with $\lambda_U = 1.4$ are listed in Tab. 4.5. For this material, according to Eq. (4.12b), the electric breakdown does not contribute to the definition of the failure envelope beyond the threshold value 1.091 and, according to inequality (4.15), the electric breakdown threshold $\bar{E}_{eb}$, beyond which the EB failure mode is irrelevant to the cycle definition, is equal to 1.054.

$\bar{E}_{eb}$	$\lvert H_g \rvert$	η	H_{max}	ζ	Failure at D	
≥ 1.091	0.342	36.8%	0.524	65.2%	$(S=0)$	(ii)b
1.054	0.342	36.8%	0.519	65.9%	EB $\cup (S=0)$	(i)a
0.9	0.297	37.9%	0.426	69.7%	EB $\cup (S=0)$	(i)a

Table 4.5: Relevant numerical values for optimal cycles associated with a DEG with $\lambda_U = 1.4$ and for different values of $\bar{E}_{eb}$.

4.3 A universal plot for equibiaxial load-driven DEGs

The discussion carried so far can be conveniently summarized in the two-dimensional plot introduced in Fig. 4.6. The abscissa and the ordinate of the plot correspond the electromechanical limits of the film λ_U and $\bar{E}_{eb}$, respectively.

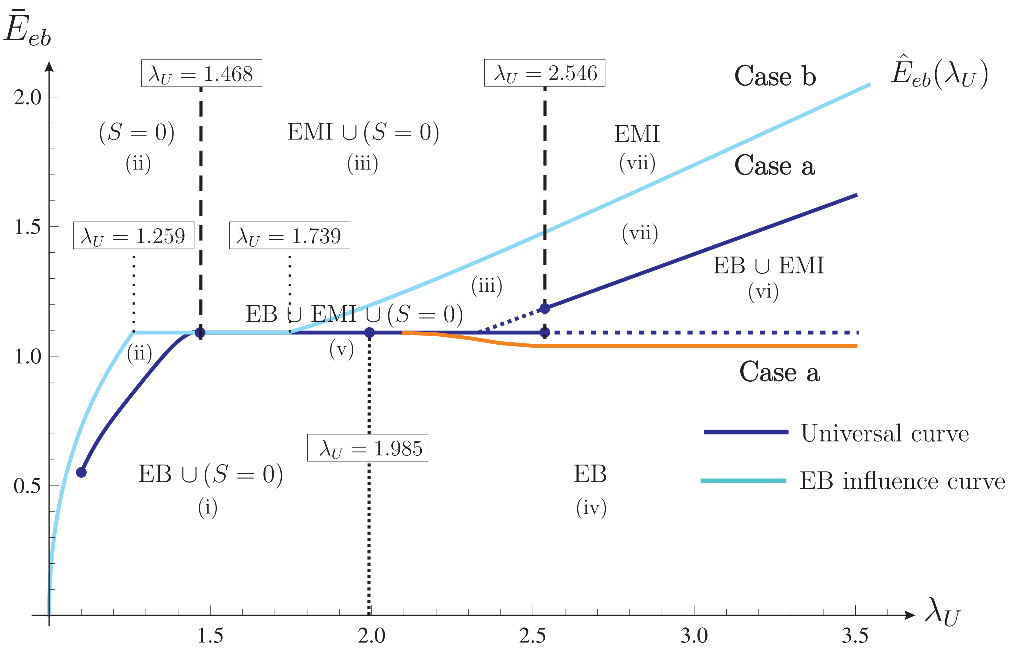

Figure 4.6: A universal plot for planar equibiaxial load-driven DEGs. The abscissa and the ordinate of the plot correspond to the electromechanical limits of the film λ_U and $\bar{E}_{eb}$, respectively. The dark-blue and orange curves divide the space of materials parameters into sections depending on the mode of failure at point D of the optimal harvesting cycle. Along the solid-dotted dark-blue curve we distinguish between the high, the moderate and the low ultimate stretch regions. Uniquely below the dark-blue curve, the failure depends on the electrical breakdown limit. Along the solid light-blue curve we distinguish between Case a and Case b, so that above this curve the electrical breakdown does not participate in the definition of the allowable state region.

In accordance with the qualitative discussion developed at the beginning of this Chapter, see e.g. Subsect. 4.1.3, we observe that the dark-blue solid curve with dots splits the $\bar{E}_{eb}$–λ_U space in two. The points below the curve correspond to materials in which the electrical breakdown limit dominates the failure at point D of the optimal cycle.

The points above the curve are associated with materials in which the optimal cycle is independent of E_{eb}. Thus, at fixed ultimate stretch λ_U, beyond the dark-blue curve the harvested energy H_g and the efficiency η remain constant. The curve is characterised by three regions that correspond to the low, the moderate and the high ultimate stretch ratio. The curves and line segments emanating from the main curve divide the two-dimensional space $(\lambda_U, \bar{E}_{eb})$ into subregions according to the failure mode dominating at point D (cf. Tab. 4.1). In particular, for $1.468 < \lambda_U < 2.546$ (MΛU regime) the dark-blue line itself corresponds to the subregion (v), characterised by the triple intersection among the EB, the EMI and the $(S = 0)$ curves. Furthermore, the orange curve encloses subregion (iv) that corresponds to EB failure. The region between the orange and the dashed blue curves is the one corresponding to the case of two intersections between EB and EMI failure lines. On the dashed blue line itself there is a triple intersection where one of the intersections between the EB and the EMI curves coincide with the $(S = 0)$ curve [the situation discussed in connection with Fig. 4.3c].

In the same way, the light-blue solid curve represents the limit curve $\hat{E}_{eb}(\lambda_U)$, see Eqs. (4.12a), (4.12b) and (4.12c), relative to the influence of the electric breakdown in the definition of the admissible state region. This curve splits the electromechanical plane $(\lambda_U, \bar{E}_{eb})$ in two, distinguishing among Case a and Case b. The points above the light-blue curve are associated with materials in which the allowable state region is independent of E_{eb}. Hence, at fixed ultimate stretch λ_U, beyond the light-blue curve the theoretically achievable energy H_{max} is constant, as well as the effectiveness ζ.

We note that, for any given candidate to be used as a membrane in a DEG in equibiaxial loading mode, the pair $(\lambda_U, \bar{E}_{eb})$ specifies which are the failure mechanisms that limit the optimal cycle. The solid dark-blue curve can be used as a design tool for choosing materials and modes of operations for load driven DEGs. Clearly, an effective design is such that the material parameters lie as close as possible to the dark-blue curve.

4.3.1 Electromechanical properties for the best energy and efficiency cycles

The universal dark-blue curve in Fig. 4.6, as said before, is a design tool for the realization of optimal electromechanical transducers. Among the optimal configurations detected by the curve, it is interesting to individuate the optimal couples of electromechanical properties $(\lambda_U,\ \bar{E}_{eb})$ ensuring the best performance in terms of efficiency, *optimum-efficiency device*, as well as in terms of harvested energy, *optimum-energy device*.

Following the procedure explained at the beginning of this Chapter, we minimise Eq. (4.7) and maximise Eq. (4.11) with respect to the variable set $\{\lambda_A, \lambda_B, \lambda_D, \Delta\bar{\phi}, \bar{E}_U, \bar{E}_{eb}, \lambda_U\}$, imposing the additional constraint $1 < \lambda_U \leq 3$.

The outcome of this procedure is the two pairs of electromechanical properties entailing maximal efficiency and maximal gained energy, see Tab. 4.6.

	λ_U	$\bar{E}_{eb}$	$\lvert H_g \rvert$	η [%]	H_{max}	ζ [%]	Failure
Maximal efficiency	1.563	1.091	0.559	43.7	0.762	73.3	(v)a
Maximal energy	3	1.396	1.145	17.2	2.852	40.1	(vi)a

TABLE 4.6: Electromechanical properties ensuring the best performance in terms of efficiency and harvested energy for an equibiaxial load-driven DEG.

From the comparison of the results, we note that the optimum-efficiency DEG has not only higher efficiency but also higher effectiveness with respect to the optimum-energy one. Moreover, differently from the plane-strain case, the energy harvested by the optimum-energy device is just two times the energy harvested by the optimum-efficiency one. This means that, the optimum-efficiency generator is exploiting the major part of the allowable state region obtaining approximately the 40% of the total invested energy. The optimum-energy generator instead exploits less than a half of the admissible state region harvesting a double amount of energy, which, however, is only 17% of the total invested energy.

Following the same procedure explained in Subsect. 3.3.1, for a given value of the dimensionless breakdown threshold $\bar{E}_{eb}$, we can obtain the current electric breakdown E_{eb} and plot it as a function of the shear modulus μ and of the relative permittivity ϵ_r. The plots of the current electric field relative to the optimum-efficiency and to the optimum-energy ideal equibiaxial DEGs are depicted, respectively, in Figs. 4.7a and 4.7b, for $\mu = 10 \div 1000$ kPa and $\epsilon_r = 2 \div 10$.

These plots show that the current electric field ranges from 12 to 259 MV/m for the optimum-efficiency device at $\lambda_U = 1.563$ (MΛU) and $\bar{E}_{eb} = 1.091$, while it ranges from 15 to 331 MV/m for the optimum-energy device at $\lambda_U = 3$ (HΛU) and $\bar{E}_{eb} = 1.396$. For the plane-strain loading mode, see Sect. 3.3.1, the electric breakdown fields required by the optimum cycles are higher, whereas the ultimate stretches required are nearly the same, cf. Tabs. 3.7 and 4.7. In terms of harvested energy, with respect to the plane-strain loading mode, the equibiaxial one allows a seven-fold and a four-fold increments for the optimum-efficiency and optimum-energy devices, respectively.

The main outcome arising from this analysis is that for a fixed pair of electromechanical properties (λ_U, $\bar{E}_{eb}$), on the one hand, the highest the shear modulus μ, the highest the gained energy H_g and, on the other hand, the lower the relative permittivity ϵ_r,

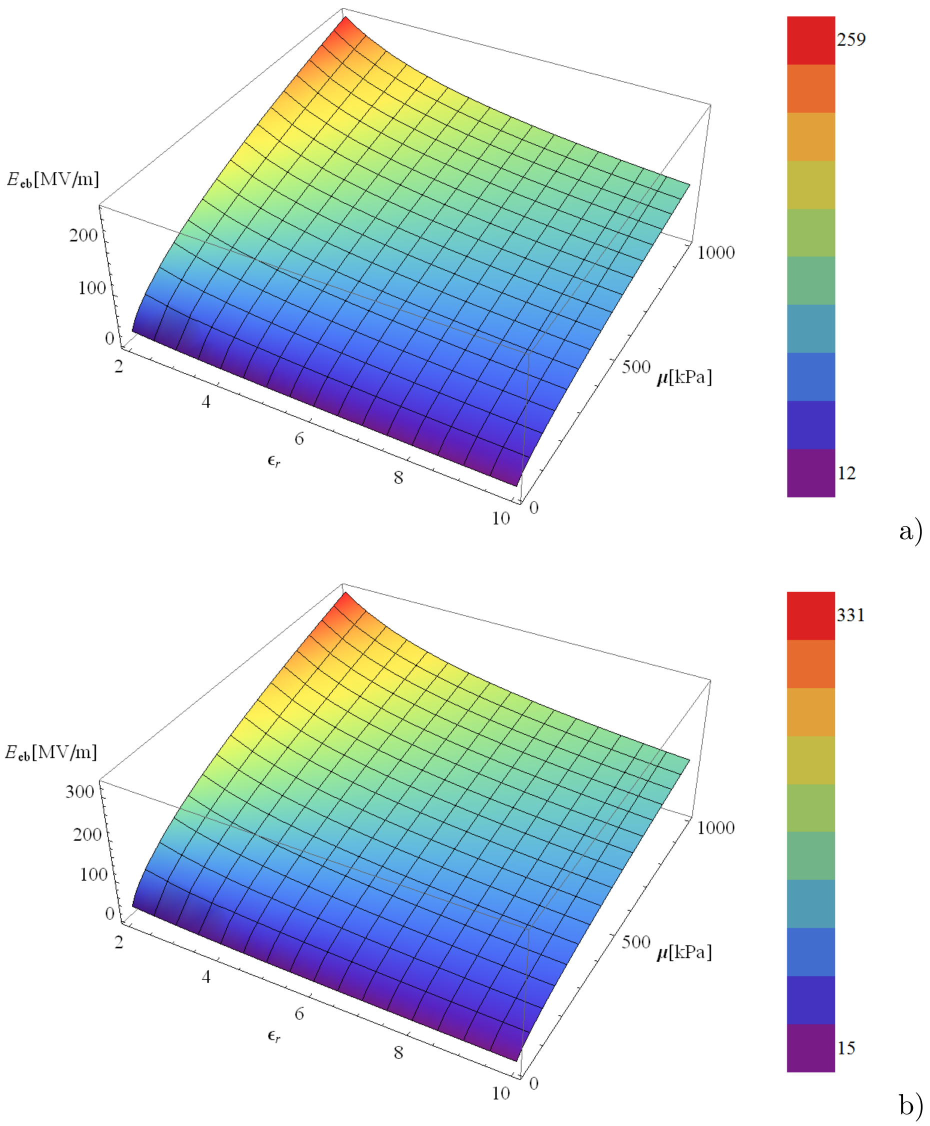

FIGURE 4.7: Values of the electric breakdown strength E_{eb} [MV/m] as a function of the shear modulus μ and of the relative dielectric permittivity ϵ_r for the best performance in terms of: a) efficiency, for $\lambda_U = 1.563$ (MΛU) and $\bar{E}_{eb} = 1.091$ and b) energy, for $\lambda_U = 3$ (HΛU) and $\bar{E}_{eb} = 1.396$.

the higher the current electric breakdown field E_{eb}. For example, focusing on the best efficiency cycle, if the shear modulus is $\mu = 10, 100, 1000$ kPa the gained energy is $H_g = 5.59, 55.90, 559.00$ kJ, independently of the relative permittivity ϵ_r. The current breakdown fields corresponding to these values of shear modulus are, respectively, $E_{eb} = 23.76, 75.15, 237.64$ MV/m if $\epsilon_r = 2$, while are $E_{eb} = 11.88, 37.57, 118.82$ MV/m if $\epsilon_r = 8$.

As a general rule, for a given value of the shear modulus, a four-fold increment in the relative permittivity involves a halving of the current electric breakdown field, whereas, for a given value of the relative permittivity, the energy increases proportionally to the shear modulus of the material.

4.4 Equibiaxial DEGs based on commercially available soft DEs

The analysis previously developed is applied to two specific commercially available DEs, the acrylic VHB-4910 and the natural rubber designated ZruElast A1040. The ZruElast A1040, produced by Zrunek Rubber Technology, is a natural rubber containing 23 wt% of inorganic fillers and 1.19 wt% of carbon. The mechanical and electrical properties of the two materials listed in Tab. 4.7 are taken from [31].

Material	[Ref.]	μ [kPa]	ϵ_r	ρ [kg/m^3]	$E_{eb}(1)$ [MV/m]	$\mathcal{R}$
VHB-4910	[31]	52	4.2	960	68.57	0.54
ZruElast A1040	[31]	917	3.4	945	120.1	0.70

Table 4.7: Physical properties and electric breakdown parameters for the rigid electrode configuration.

	VHB-4910		ZruElast A1040	
λ_U	E_{eb} [MV/m]	$\bar{E}_{eb}$	E_{eb} [MV/m]	$\bar{E}_{eb}$
1.8	94	2.518	181	1.037
2.0	100	2.666	195	1.117
3.0	124	3.318	260	1.483

Table 4.8: Electric breakdown data for the two elastomers at different ultimate stretches λ_U, see [60].

In [60] two experimental configurations for the measurement of the stretch dependence of the electric breakdown strength are reported and the dielectric function (i.e., the dielectric permittivity) and breakdown strength of VHB-4910 and ZruElast are compared. The experimental data are obtained employing both rigid and compliant electrodes and are fitted with the phenomenological relation

$$E_{eb}(\lambda) = E_{eb}(1)\lambda^{\mathcal{R}}, \tag{4.16}$$

where $E_{eb}(1)$ is the electric breakdown field when the membrane is not stretched and $\mathcal{R}$ is the degree of sensitivity of the E_{eb} toward the stretch λ. Herein we take into account the data reported in [60] corresponding to the experiments with rigid electrodes. This configuration suppresses the actuation of the elastomer during the breakdown measurements. The parameters $E_{eb}(1)$ and $\mathcal{R}$ for the rigid electrode configuration are listed in Tab. 4.7, while the electric breakdown data for the two materials at different λ_U are summarized in Tab. 4.8.

Once the dielectric strength is determined, we can compute the theoretically achievable energy (2.59) according to the different choices of the ultimate stretches. Furthermore, we estimate the performance of a generator, or a cycle, by computing both the efficiency (2.58) and the effectiveness (2.61). In facts, the computation of both these parameters allows the comparison of the various optimal cycles for materials with different electromechanical characteristics.

In the central sections of Tabs. 4.9 and 4.10 the performance of generators based on a single membrane of these two materials is compared for $\lambda_U = 1.8$ and 3, respectively. The column ‘M-C’ stands for *material classification* and refers to the failure modes limiting the optimal cycle according to the subregion introduced in Fig. 4.6. A comparison between the two tables reveals that, at the one hand, the total amount of energy extracted from a single HΛU membrane is substantially higher than the one extracted from a similar membrane with a smaller λ_U. At the other hand, the cycles in the MΛU regime ($\lambda_U = 1.8$) exhibit higher efficiencies and effectivenesses than the ones exhibited by the corresponding cycles in the HΛU regime ($\lambda_U = 3$). We also note that for $\lambda_U = 3$ the optimal cycle for both membranes is the same in terms of dimensionless quantities, as both HΛU cycles are independent of the dielectric strengths. Therefore, the efficiency of the two generators is identical. The effectiveness of the two HΛU cycles is slightly different since the theoretically achievable energy for the ZruElast is limited by the electric breakdown limit, while for the VHB-4910 it is independent of this limit. Looking at the theoretically achievable energy per unit mass, [31] reports for a ZruElast-based a value of 3000 J/kg, that is compatible with our finding of 2862.68 J/kg (see Tab. 4.10). Whereas, for a generator made up of VHB-4910, the same paper provides a value of 1200 J/kg calculated employing an extremely high rupture stretch, approximately equal to 8. In our case, the estimated value for $\lambda_U = 3$ is 166.68 J/kg.

	$\lambda_U = 1.8$								
	Single membrane							Multi-membrane	
Material	$S_{\max}$ [kPa]	$\hat{H}_g$ [J/kg]	$\Delta\phi/h_0$ [kV/mm]	η %	M-C	$\hat{H}_{max}$ [J/kg]	ζ %	n [1/kN]	$n\tilde{H}_g$ [J/kN]
VHB-4910	82.59	38.82	6.17	37.1	(iii)b	58.93	65.9	121	45.124
ZruElast	1480	608.46	25.75	32.9	(i)a	1019.17	59.7	7	38.851

Table 4.9: Data for DEGs with two MΛU elastomers and two configurations: $\hat{H}_g = \mu H_g/\rho$, harvested energy density per unit mass, $\Delta\phi/h_0$, activation electric potential per unit referential thickness, η, efficiency, M-C, material classification according to Fig. 4.6, $\hat{H}_{max} = \mu H_{max}/\rho$, theoretically achievable energy, ζ, effectiveness; n, number of 1 mm thick layers required to sustain 1 kN at λ_U, $n\tilde{H}_g$, total harvested energy by the multi-membrane DEG.

As a conclusion, we note that, from a practical viewpoint, a comparison between DEGs based on different materials should take into account their load capacity too. Thus, while the comparison carried so far between the VHB-4910 and the ZruElast based

	$\lambda_U = 3$								
	Single membrane							Multi-membrane	
	$S_{\max}$	$\hat{H}_g$	$\Delta\phi/h_0$	η	M-C	$\hat{H}_{max}$	ζ	n	$n\tilde{H}_g$
Material	[kPa]	[J/kg]	[kV/mm]	%		[J/kg]	%	[1/kN]	[J/kN]
VHB-4910	142.25	62.04	3.67	17.2	(vi)a	166.68	37.2	70	41.878
ZruElast	2508	1111.51	17.14	17.2	(vi)a	2862.62	38.8	4	41.878

Table 4.10: Data for DEGs with two HΛU elastomers and two configurations: $\hat{H}_g = \mu H_g/\rho$, harvested energy density per unit mass, $\Delta\phi/h_0$, activation electric potential per unit referential thickness, η, efficiency, M-C, material classification according to Fig. 4.6, $\hat{H}_{max} = \mu H_{max}/\rho$, theoretically achievable energy, ζ, effectiveness; n, number of 1 mm thick layers required to sustain 1 kN at λ_U, $n\tilde{H}_g$, total harvested energy by the multi-membrane DEG.

DEGs is significant in terms of efficiency and effectiveness, to compare the total amount of harvested energy, DEGs with similar load bearing capacities should be considered. To this end, we examine DEGs based on layered membranes of similar external dimensions which are made up of a number of DE layers with identical thickness. The number of layers is set in such a way that, at a given stretch, the multi-membrane device withstands a lateral force of 1 kN. By way of illustration, if we take the thickness of each layer to be 1 mm, then 121 VHB-4910 layers are required to sustain a 1 kN lateral force at $\lambda_U = 1.8$ for an equibiaxial stress state. For a ZruElast-based layered membrane, due to its relatively higher stiffness, only 7 layers with the same thickness are needed.

The relevant data for MΛU and HΛU DEGs is summarized at the right-hand side sections of Tabs. 4.9 and 4.10, respectively. In terms of the total amount of extractable energy ($n\tilde{H}_g$), the VHB-based DEG performs slightly better at the moderate stretch level ($\lambda_U = 1.8$). At the high stretch regime ($\lambda_U = 3$) the amounts of energy that can be extracted from the two DEGs are the same since in this case the selected optimal cycles for both materials correspond to points in subregion (vi) of Fig. 4.6 (see the M-C column in Tab. 4.10). We note that, from a theoretical point of view, with the right configuration, the performances of DEGs based on the two materials are quite similar in terms of total harvested energy, efficiency and effectiveness. The VHB-based DEG is slightly superior at the low stretching regime, but from a practical viewpoint it is inferior due to its complicated structure that involves a large number of layers. However, we find that the performances of the MΛU DEGs are superior to those of HΛU DEGs in the sense that similar amounts of energy can be extracted at each cycle, but the efficiencies of the MΛU cycles are higher. This implies that, in real-life applications, less heat due to wasted mechanical energy will be dissipated to the environment. The smaller number of layers required for the HΛU DEGs is an advantage from a manufacturing viewpoint.

4.5 Benefits of ceramic filler addition

As we have seen in Sect. 4.3, in order to extract the maximum energy from the DEG, it is important that the pair of electromechanical properties of the material (λ_U, $\bar{E}_{eb}$) lies as close as possible to the universal curve.

To this end, composite materials with improved electromechanical coupling could be employed in the realization of enhanced electromechanical transducers. In facts, it is possible to modify the DEG performance by adding small amount of ceramic fillers to the silicone. As a result of this operation, the electromechanical properties of the material approach the universal curve.

Promising materials, already tested for dielectric elastomer actuators, are random composites, where ceramic fillers with a high dielectric constant are dispersed in a silicone matrix. Three ceramic–polymer composites are here taken into account (see [20], [56] and [51]), all three adopting for the matrix similar commercial formulations based on poly–dimethyl–siloxane (hereafter simply denoted as PDMS), as candidates for the realization of enhanced DEGs. The silicone elastomer is chosen for its suitable mechanical properties (low shear modulus and high stretchability), high dielectric breakdown strength, low dielectric loss, fast response, chemical and biological inertness, easy workability and bonding to the fillers. The filler particles for the three materials consist of the following perovskite–type electroceramics, respectively:

a) PMN–PT powder very finely sized with spherically shaped particles, precisely a mix of 85% lead magnesium niobate $Pb(Mg_{1/3}Nb_{2/3})O_3$ (PMN) and 15% lead titanate $PbTiO_3$ (PT) [20] (density $\rho \simeq 7900$ kg/m^3); PMN–PT belongs to a new generation of piezoelectric ceramics formulated to exhibit very high values of both piezoelectric coefficient and relative permittivity (declared to be 19000 in the product data sheet for the formulation we refer to, [20]) with low dielectric losses. The addition of PT to PMN stabilizes its inclination to assume a perovskite structure, therefore PMN–PT exhibits a dielectric constant higher than PMN. Moreover, the adoption of spherical particles for the filler contributes to limit the increase in stiffness due to the ceramic. While paper [20] compares the behaviour of composites at various filler contents, namely 10%, 20%, 30% in volume, the formulation chosen as material *a*) refers to a percentage of 10% (chosen in order to maximise the DEG harvested energy) and the relevant fundamental parameters are summarized in Tab. 4.11;

b) PZT powder, i.e. lead zirconate–titanate, $Pb[Zr_{1-x}Ti_x]O_3$ [56], one of the most widely used piezoelectric ceramic materials (density $\rho \simeq 7700$ kg/m^3), having a considerable dielectric constant (about 2000). In [56], where the composite is investigated towards the application as a vibration damper, exploiting the increase of the material loss factor

#	Composite	[Ref.]	μ [kPa]	ϵ_r	E_{eb}[MV/m]	$\bar{E}_{eb}$	ρ [kg/m^3]
a)	■PMN–PT	[20]	33.33	10.2	21	1.093	1660
b)	⬟PZT	[56]	42	10	25.208	1.157	1030
c)	●CCTO	[51]	43.5	4.48	37.9	1.144	1955

TABLE 4.11: Sets of parameters for the ceramic–polymer composites analyzed.

allowed by PZT, different volume fractions of the ceramic are considered, ranging from 0 to 32% and great care is devoted to the description of the poling treatment, further enhancing the dielectric constant and the piezoelectric coefficient of the PZT/PDMS composite. The formulation chosen here as material *b*) assumes a percentage of PZT equal to 1% in volume (the poling treatment doesn't affect significantly the performance of the composite at such low concentration) with the relevant parameters summarized in Tab. 4.11.

c) CCTO powder, i.e. calcium copper titanate, $CaCu_3Ti_4O_{12}$ [51], a non-ferroelectric ceramic filler (density $\rho \simeq 5120$ kg/m^3), having a substantial dielectric constant (about 1000 at 0.1 Hz). In [51], the composite is investigated for the realization of an industrially scalable DE actuator. In this paper, different volume fractions of the ceramic dispersed phase are considered, namely 2.3%, 5.1%, 8.4%, and experimental values of the dielectric breakdown strength are reported. The formulation chosen here as material *c*) assumes a percentage of CCTO equal to 2.3% in volume, whose relevant parameters are summarized in Tab. 4.11.

The first two materials considered are both based on lead, while the last one is a non-ferroelectric lead-free ceramic. All the significant parameters for the three composites investigated are reported in Tab. 4.11, namely the shear modulus μ, the relative permittivity ϵ_r, the dielectric strength E_{eb}, its dimensionless version $\bar{E}_{eb}$ and the estimate of the density ρ assuming for PDMS a value of 970 kg/m^3. Actually, the dielectric strength of materials *a*) and *b*), not given in the reference papers, has been evaluated on the basis of equation (6.23) in [9].

As for the relative permittivity, it is interesting to point out that all the data available in [20] for material *a*) have been evaluated using frequencies of 100 Hz and 10 kHz, respectively: unfortunately the data for lower frequencies were not available, so we decided to adopt the values measured for a frequency of 100 Hz. For material *c*), in [51] the data regarding the relative permittivity have been evaluated ranging the frequency from 0.1 Hz up to 1 MHz, however the relative permittivity of this material show a frequency independent behaviour. Whereas for material *b*), the Authors of [56] do not specify the assumed frequency for the measurement of the relative permittivity. It is interesting to observe here that the operating frequencies of DEGs can vary widely, e.g. more than 100 Hz in the case of vibrational energy harvesting systems or less than 1 Hz for ocean wave power harvesting devices. The shear modulus assumed for both materials corresponds to the extrapolation to a frequency of 0 Hz, as the constitutive law adopted does not consider a variability of the mechanical properties with frequency.

The ultimate strength λ_U is not mentioned explicitly in the reference papers [20], [56] and [51]. Nevertheless, Fig. 2 in [20], illustrating the nominal stress–nominal strain curve for material *a*), shows very high extreme values of strain (it is not specified if ultimate), at least 480% and 570% for pure PDMS and for the composite with 10% PMN–PT filler content, respectively. However, in order to maximise the harvested energy of DEGs, moderate maximal strains are considered, therefore it seems that for all the three composites under study λ_U can be assumed quite large (hereafter as large as 3).

For the sake of completeness, the same parameters are reported in Tab. 4.12 for the PDMS formulations used as matrices in the three composites: from a comparison with Tab. 4.11, the enhancement of the relative permittivity, as well as both the increase of the shear modulus and the drop of the dielectric strength, can be appreciated.

#	PDMS	[Ref.]	μ [kPa]	ϵ_r	E_{eb} [MV/m]	$\bar{E}_{eb}$	ρ [kg/m^3]
a)	□PMN–PT	[20]	20.7	7.32	55	3.07	970
b)	⬠PZT	[56]	34	3.5	55	1.66	970
c)	○CCTO	[51]	43	3.13	55.9	1.42	970

TABLE 4.12: Sets of parameters for the three PDMS involved in the ceramic–polymer composites.

For each materials, we can individuate the optimal harvesting cycle by plotting the electromechanical properties of the three composite and of their PDMS matrices on the $\bar{E}_{eb}$–λ_U plane, as depicted in Fig. 4.8. In this way we identify the failure subregion to which each materials belong.

As evident from Fig. 4.8, in the moderate stretch regime (MΛU), the electromechanical properties of the three composites lie closer to the universal curve with respect to those of the silicones.

Concerning the dissipative behaviour of the three composite materials, the only available data regard the dielectric loss (ratio between imaginary and real parts of the complex dielectric constant) for materials *a*) and *c*) and the material loss (ratio between the viscous loss modulus and the storage modulus) for material *b*): in all the three cases it is evident an increase of losses with the filler content, even if for material *b*) the effects are very limited, as the filler content is very low. However the current analysis neglects all the dissipative sources.

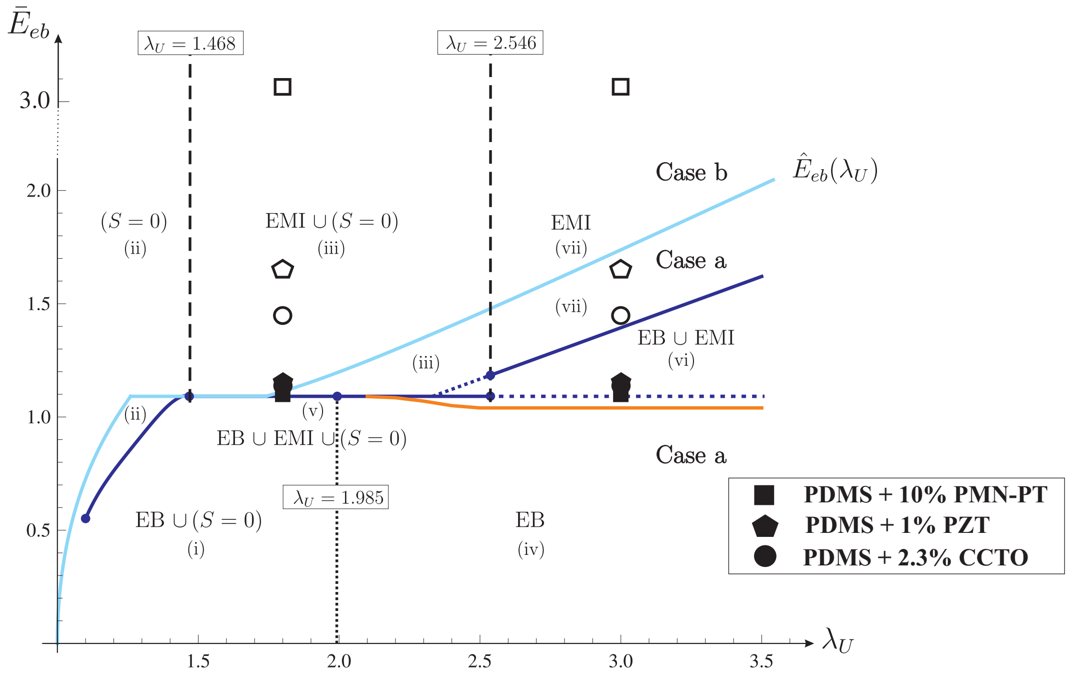

FIGURE 4.8: Universal design curve for planar equibiaxial load-driven DEGs already introduced in Fig. 4.6: electromechanical characteristics of the three composites, black shapes, and of their PDMS matrices, white shapes.

We have to specify that, in this work, we consider the random composite as a homogeneous material at the macroscopic level. However, at the micro-scale, phenomena of stress concentration and interface damage due to the filler inclusions may occur.

4.5.1 Material *a*)

Looking at the dimensionless performance of the composite and the pure PDMS generators, reported in Tab. 4.13, we can advance some preliminary considerations about the substantial behaviour of the two DEGs at MΛU and HΛU. At $\lambda_U = 1.8$ both the generators experience the same failure (iii) characterised by the same energy. Thus, the material with the higher shear modulus, that is the composite, will harvest the larger amount of energy. The increment in the energy produced by the composite DEG will be equal to the increment in the shear modulus of material *a*) with respect to its pure matrix, i.e. 60%. At $\lambda_U = 3.0$ composite and pure PDMS generators undergo different failures, (vi) and (vii) respectively. From a dimensionless viewpoint, the pure PDMS DEG harvests a larger amount of energy with respect to the composite DEG. On the contrary, taking into account the generated energy per unit volume, we have that the energy $\mu_{\mathrm{mat}.a)} H g^{\mathrm{(vi)}}_{\mathrm{mat}.a)}$ produced by the composite DEG is larger than that harvested by the pure PDMS device, $\mu_{\mathrm{PDMS}} H g^{\mathrm{(vii)}}_{\mathrm{PDMS}}$. This is due to the fact that the shear modulus of material $a)$ is larger than an equivalent shear modulus defined as

$$\mu_{\text{mat.}a)} > \mu^{\text{eq}}_{\text{mat.}a)} = \mu_{\text{PDMS}} \frac{{H_g}^{(\text{vii})}_{\text{PDMS}}}{{H_g}^{(\text{vi})}_{\text{mat.}a)}} = 1.3128\, \mu_{\text{PDMS}} = 21.17\ \text{kPa}. \tag{4.17}$$

Since the shear modulus of material $a)$ is equal to 33.33 kPa (see Tab. 4.11), we expect, accordingly, a 22.6% increment in the generated energy with respect to the pure PDMS DEG.

Material *a*)	**Pure PDMS** ☐	**PDMS–10%PMN–PT** ■
	Generated energy-density per unit shear modulus	
$\lambda_U = 1.8$	(iii)b 0.7167	(iii)a 0.7167
$\lambda_U = 3$	(vii)b 1.1454	(vi)a 0.8725

TABLE 4.13: Material classification M-C, according to Fig. 4.8, and generated energy-density per unit shear modulus H_g for the selected harvesting cycles for the composite material $a)$ and its matrix.

Tab. 4.14 reports a comparison between the generated energy per unit volume and the voltage jump $\Delta\phi = \phi_C - \phi_B$ necessary for the activation of the harvesting cycle both for the PDMS material and the PDMS–10%PMN-PT composite: the advantage of material $a)$ over its PDMS formulation is higher than 60% for $\lambda_U = 1.8$, while it is just higher than 20% for $\lambda_U = 3.0$. Fig. 4.8 shows precisely that, for the two values λ_U considered, the composite electromechanical properties lie closer to the universal design curve with respect to the pure PDMS ones. As the content of the ceramic filler is such that the density of the composite is about 70% higher than that of the PDMS (see Tab. 4.11), there is no substantial advantage in using this composite in place of the homogeneous material when the performance is compared in terms of harvested energy per unit mass.

Material *a*)	**Pure PDMS** ☐	**PDMS–10%PMN–PT** ■	**Gain**
	Generated energy per unit volume		
$\lambda_U = 1.8$	(iii)b 14.836 kJ/m^3 [2.95 kV]	(iii)a 23.888 kJ/m^3 [3.15 kV]	61.0%
$\lambda_U = 3$	(vii)b 23.711 kJ/m^3 [1.75 kV]	(vi)a 29.083 kJ/m^3 [0.78 kV]	22.68%

TABLE 4.14: Material classification M-C according to Fig. 4.8, generated energy per unit volume μH_g, required voltage $\Delta\phi$ (inside square brackets) and percentage gain for the selected harvesting cycles allowed by the composite material $a)$ over its matrix.

In respect of the cycles plotted on the mechanical S–λ plane, we also note that the composite requires maximum forces higher than the pure PDMS and this effect becomes more marked for high maximum stretches (see Figs. 4.9A.I and 4.9A.II and, in particular, Figs. 4.10A.I and 4.10A.II). The maximum stresses achieved during the cycle by the pure silicone device are approximately 32 kPa at $\lambda_U = 1.8$ and 56 kPa at $\lambda_U = 3.0$, while those reached by the composite material $a)$ are respectively 53 kPa and 98 kPa.

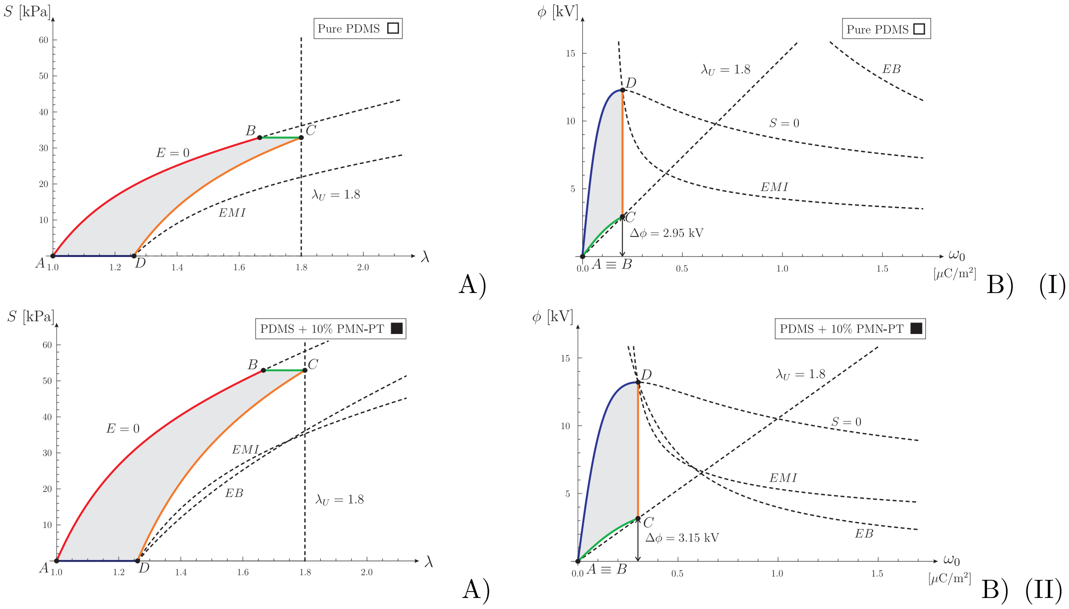

FIGURE 4.9: Optimal cycle for (I) the pure PDMS and (II) the PDMS–%10PMN–PT composite, on the A) mechanical and B) electrical planes, in the case $\lambda_U = 1.8$. With respect to the EB influence on the optimal cycle, both materials appertain to subregion (iii) (cf. e.g. Fig. 4.8). With respect to the EB influence on the admissible state region, the pure PDMS is related to Case b, whereas the composite pertains to Case a.

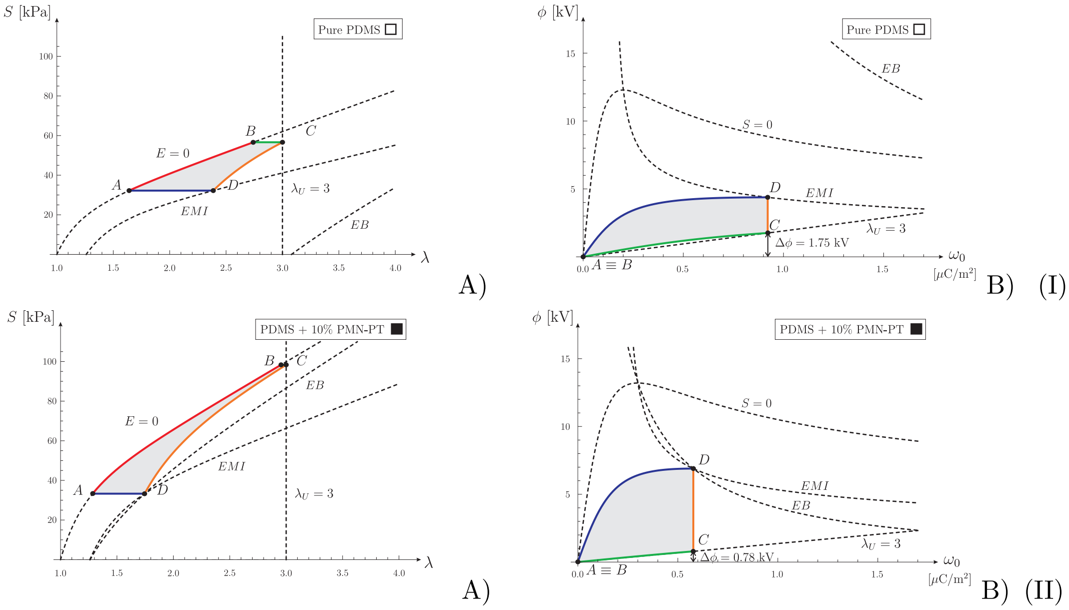

FIGURE 4.10: Optimal cycle for (I) the pure PDMS and (II) the PDMS–%10PMN–PT composite, on the A) mechanical and B) electrical planes, in the case $\lambda_U = 3.0$. With respect to the EB influence on the optimal cycle, the pure PDMS lies on subregion (vii), while the composite belongs to subregion (vi) (cf. e.g. Fig. 4.8). With respect to the EB influence on the admissible state region, the pure PDMS is related to Case b, instead the composite pertains to Case a.

4.5.2 Material *b*)

Looking at the dimensionless performance of the composite and the pure PDMS generators, reported in Tab. 4.15, we can obtain some preliminary informations about the substantial behaviour of the two DEGs at MΛU and HΛU. As for material *a*), at $\lambda_U = 1.8$ both the generators experience the same failure (iii) characterised by constant energy. Thus, the material with the higher shear modulus, i.e. the composite, will harvest the larger amount of energy. As said before, the increment in the energy produced by the composite DEG will be equal to the increment in the shear modulus of material *b*) with respect to its pure matrix, i.e. 23.5%. At $\lambda_U = 3.0$ the composite and pure PDMS generators undergo different failures, (vi) and (vii) respectively. From a dimensionless viewpoint, as for material *a*), the pure PDMS DEG harvests a larger amount of energy with respect to the composite DEG. But, taking into account the generated energy per unit volume, we have that the energy $\mu_{\text{mat.}b)} H_{g_{\text{mat.}b)}}^{(\text{vi})}$ extracted by the composite generator is larger than that harvested by the pure PDMS DEG, $\mu_{\text{PDMS}} H_{g_{\text{PDMS}}}^{(\text{vii})}$. This is due to the fact that, as for material *a*), the shear modulus of composite *b*) is larger than an equivalent shear modulus defined as

$$\mu_{\text{mat.}b)} > \mu_{\text{mat.}b)}^{\text{eq}} = \mu_{\text{PDMS}} \frac{H_{g_{\text{PDMS}}}^{(\text{vii})}}{H_{g_{\text{mat.}b)}}^{(\text{vi})}} = 1.195\,\mu_{\text{PDMS}} = 40.03 \text{ kPa}. \tag{4.18}$$

On account of the fact that the material *b*) has a shear modulus equal to 42 kPa (see Tab. 4.11), we expect just a 3% increment in the generated energy with respect to the pure PDMS DEG.

Material *b*)	**Pure PDMS ⬠**	**PDMS–1%PZT ⬟**
Generated energy-density per unit shear modulus		
$\lambda_U = 1.8$	(iii)b 0.7167	(iii)b 0.7167
$\lambda_U = 3$	(vii)a 1.1454	(vi)a 0.9586

Table 4.15: Material classification M-C, according to Fig. 4.8, and generated energy-density per unit shear modulus H_g for the selected harvesting cycles for the composite material *b*) and its matrix.

Tab. 4.16 reports a comparison between the harvested energy per unit volume and the voltage for the activation of the harvesting cycle for the pure PDMS and for the PDMS–1%PZT composite: at $\lambda_U = 1.8$ the advantage of material *b*) on the corresponding silicone is less evident but still consistent around 23.5%, while at $\lambda_U = 3$ the advantage is only 3.44%. As depicted in Fig. 4.8, for $\lambda_U = 1.8$ the composite electromechanical properties lie closer to the universal curve with respect to the pure PDMS ones, while for $\lambda_U = 3.0$ the electromechanical properties of the two material are approximately equidistant from the universal design curve. As evident from the numerical data listed in Tab. 4.16, at $\lambda_U = 3.0$ material *b*) and its corresponding PDMS harvest nearly the same amount of energy. Moreover, this composite, unlike material *a*), shows also a sensible improvement of the generated energy per unit mass with respect to the pure PDMS for $\lambda_U = 1.8$ and then it is particularly suitable for applications where weight is an important issue to be addressed in the generator design.

Material *b*)	**Pure PDMS ⬠**	**PDMS–1%PZT ⬟**	**Gain**
	Generated energy per unit volume		
$\lambda_U = 1.8$	(iii)b 24.368 kJ/m^3 [5.46 kV]	(iii)b 30.102 kJ/m^3 [3.59 kV]	23.5%
$\lambda_U = 3$	(vii)a 38.945 kJ/m^3 [3.25 kV]	(vi)a 40.261 kJ/m^3 [1.13 kV]	3.44%
	Generated energy per unit mass		
$\lambda_U = 1.8$	(iii)b 25.12 J/kg	(iii)b 29.22 J/kg	16.3%
$\lambda_U = 3$	(vii)a 40.14 J/kg	(vi)a 39.09 J/kg	-2.64%

TABLE 4.16: Material classification M-C according to Fig. 4.8, generated energy per unit volume μH_g and per unit mass $\hat{H}_g$, required voltage $\Delta\phi$ for the selected harvesting cycles (inside square brackets) and percentage gain allowed by the composite material *b*) over its matrix.

Also in this case we note that the composite requires maximum forces higher than the pure silicone, particularly for high maximum stretches. The maximum stresses achieved during the cycle by the pure PDMS DEG are approximately 54 kPa at $\lambda_U = 1.8$ and 93 kPa at $\lambda_U = 3.0$, while those reached by the composite *b*) are respectively 66 kPa and 122 kPa.

4.5.3 Material *c*)

Looking at the dimensionless performance of the composite and the pure PDMS generators, reported in Tab. 4.17, we can acquire some basic informations about the substantial behaviour of the two DEGs at MΛU and HΛU. As for material *a*) and *b*), at $\lambda_U = 1.8$ both the generators experience the same failure (iii) characterised by constant energy. Thus, the material with the higher shear modulus, i.e. the composite, will harvest the larger amount of energy. As said before, the increment in the energy produced by the composite DEG will be equal to the increment in the shear modulus of material *c*) with respect to its pure matrix, i.e. 1.16%. At $\lambda_U = 3.0$, as for the other two materials, the composite and pure PDMS generators undergo different failures, (vi) and (vii) respectively. The pure PDMS DEG harvests a larger amount of energy with respect to the composite DEG and in this case not only from a dimensionless viewpoint, but also taking into account the generated energy per unit volume μH_g. Actually, we have that the energy $\mu_{\text{mat}.c)} H_{g_{\text{mat}.c)}}^{(\text{vi})}$ harvested by the composite DEG is smaller than that produced by the pure PDMS device, $\mu_{\text{PDMS}} H_{g_{\text{PDMS}}}^{(\text{vii})}$. This is due to the fact that the shear modulus of material $c)$ is larger than an equivalent shear modulus defined as

$$\mu_{\mathrm{mat}.c)} < \mu^{\mathrm{eq}}_{\mathrm{mat}.c)} = \mu_{\mathrm{PDMS}} \frac{H_{g_{\mathrm{PDMS}}}^{(\mathrm{vii})}}{H_{g_{\mathrm{mat}.c)}}^{(\mathrm{vi})}} = 1.216\,\mu_{\mathrm{PDMS}} = 52.29 \text{ kPa}. \tag{4.19}$$

In view of the fact that the shear modulus of material $c)$ is equal to 43.5 kPa (see Tab. 4.11), we expect a 16.8% decrement.

Material *c*)	**Pure PDMS ○**	**PDMS–2.3%CCTO ●**
Generated energy-density per unit shear modulus		
$\lambda_U = 1.8$	(iii)b 0.7167	(iii)b 0.7167
$\lambda_U = 3$	(vii)a 1.1454	(vi)a 0.9418

TABLE 4.17: Material classification M-C, according to Fig. 4.8, and generated energy-density per unit shear modulus H_g for the selected harvesting cycles for the composite material $c)$ and its matrix.

Tab. 4.18 reports a comparison between the harvested energy per unit volume and the voltage for the activation of the harvesting cycle for the pure PDMS and for the PDMS–2.3%CCTO composite: the advantage of material $c)$ over its PDMS formulation is less than 2% at $\lambda_U = 1.8$. This is due to the fact that both the composite and the pure PDMS electromechanical properties lie very close to the universal curve, see Fig. 4.8. Moreover, the increment in the harvested energy entailed by the composite DEG is proportional to the increment in the shear modulus with respect to its PDMS formulation. In this case, the shear modulus increment is exactly 1.16%. The PDMS–2.3%CCTO composite entails an advantage only at $\lambda_U = 1.8$, since in the high stretch regime HΛU the electromechanical properties of the pure silicone lie closer to the universal curve.

Material *c*)	**Pure PDMS ○**	**PDMS–2.3%CCTO ●**	**Gain**
Generated energy per unit volume			
$\lambda_U = 1.8$	(iii)b 30.818 kJ/m^3 [6.50 kV]	(iii)b 31.176 kJ/m^3 [5.46 kV]	1.16%
$\lambda_U = 3.0$	(vii)a *49.254 kJ/m*^{3} *[3.86 kV]*	(vi)a *40.969 kJ/m*^{3} *[1.65 kV]*	-16.8%

TABLE 4.18: Material classification M-C according to Fig. 4.8, generated energy per unit volume μH_g, required voltage $\Delta\phi$ for the selected harvesting cycles (inside square brackets) and percentage gain allowed by the composite material $c)$ over its matrix.

In this case, we note that the composite and the pure PDMS require nearly the same maximum forces and this is due to the fact that the shear modulus of the two materials is fairly the same. The maximum stresses achieved during the cycle by the pure PDMS device are approximately 68 kPa at $\lambda_U = 1.8$ and 128 kPa at $\lambda_U = 3.0$, while those reached by the composite material $c)$ are respectively 69 kPa and 127 kPa.

Chapter 5

Optimisation of an ideal DEG in out-of-plane loading mode

In a real harvesting field, we can think that the mechanical action be outlined as an oscillating force, or pressure, that stretches and releases periodically the soft capacitor at a frequency on the order of the Hz. Therefore, electrical energy can be collected after the four-stroke cycle, presented in Sect. 2.5, where (i) an initial, relatively slow, stretching of the material induced by the growing force is followed by (ii) a fast charging phase; then, (iii) the slow decrease of the force will relax the capacitor at constant charge and, finally, (iv) the charge is harvested at high electric potential at low force. The same cycle has been already considered to determine optimal working ranges for homogeneous conservative planar generators deforming in uniaxial plane-strain, see Chap. 3, and equibiaxially, see Chap. 4 (cf. also [6, 57]).

In this part we assume that the external source deforms a circular DE membrane non-homogeneously out-of-plane, a layout preliminary investigated in [24] as an actuator and in [64] as a generator. Regarding the latter, however, it is important to point out that the analysis is partial, as many of the fundamental features necessary to evaluate the effectiveness of this configuration (prestretch influence, failure modes, maximum load, etc.) as a DEG are not considered. We aim at filling the gap, providing a complete analysis of this harvester layout along the lines traced in the previous Chapters. The adoption of the same methodology will also enable us to compare the different configurations on a common ground, offering the possibility to reflect on the best coupling between geometry and materials for a particular application.

The analysed deformation mode of the DE annular membrane is particularly interesting for sea-wave energy conversion as it can constitute the base power take-off element of a floating harvesting system based on a Gough/Stewart platform moored to the sea bottom by metallic legs, which are formed by a hollow cylinder constrained to the sea bed and a concentric small cylinder anchored to the buoy [11]. A number of membranes can be placed between the two elements to exploit their relative motion and producing electrical energy (Fig. 5.1c). A preliminary design performed in [11] on a prototype proposed for the Mediterranean Sea has indicated that each leg bears a total force of approximately 34 kN and this value will be adopted for the comparisons between materials and generator layouts presented in the last part of the paper. The application described above highlights one of the advantages of this generator configuration: the membrane deformation can take place on both sides of the film, being potentially capable to fully exploit an oscillating source of mechanical work.

Driven by the above motivations, and aiming at completing the research program on optimal design of load-driven DE energy harvesters within the hypothesis of energy conservation, we intend to investigate the nonlinear behaviour of the annular membrane generator with the following goals:

- determine the initial prestretch of the film that ensure the best performance of the device;
- define the ratio between inner and external radii of the annular membrane that maximise efficiency and/or harvested energy per unit mass;
- compare the performance of different soft materials (acrylic elastomer and natural rubber) for the same device and
- compare different prototype devices.

The above objectives are addressed in Sects. 5.3 and 5.4. Interestingly, the comparison of different DEG layouts, reported in Sect. 5.4, demonstrates that the annular DEG can compete with the equibiaxial planar generator, in terms not only of efficiency, but also of harvested energy.

5.1 Governing equations and material modelling of the annular DE membrane

In this Section we introduce the theoretical background of an annular membrane deforming non-homogeneously out-of-plane, by briefly recalling the governing equations and the constitutive assumptions for this coupled electromechanical problem in finite elasticity. The standard notation of continuum electromechanics is adopted and quasi-static electromechanical conditions are considered [15, 24, 45].

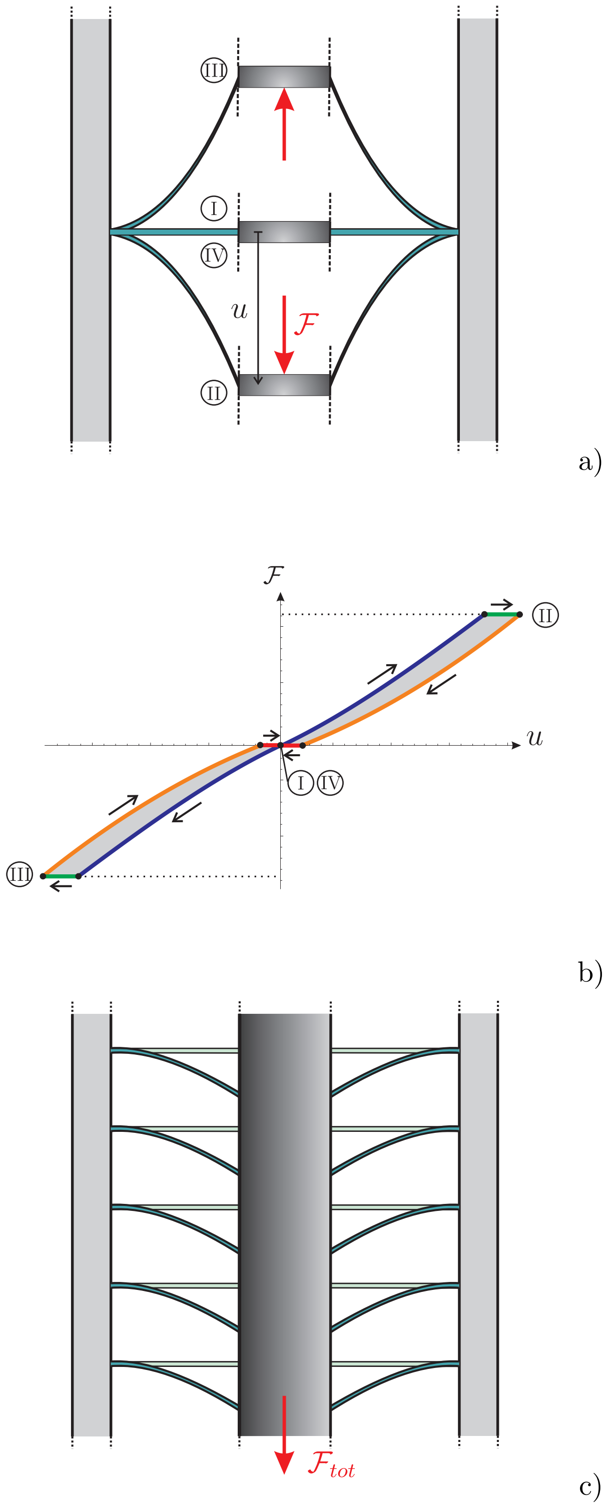

FIGURE 5.1: Sketch of the periodic four-phase cycle for the investigated electroactive membrane generator (phases IV and I coincide): a) membrane configurations; b) mechanical force ($\mathcal{F}$)–out-of-plane displacement (u) plane; c) multi-membrane device subjected to a total force $\mathcal{F}_{tot}$.

In the undeformed configuration the membrane, of initial thickness h_0, inner radius r_0^i, and outer radius r_0^e, is stress-free and unconstrained. Then the elastomeric film is radially and homogeneously prestretched of a quantity $\lambda_{pre}(\geq 1)$ and constrained at the outer boundary to a rigid ring of radius $\lambda_{pre}r_0^e$ and at the inner boundary to a rigid circular plate of radius $\lambda_{pre}r_0^i$; the plate can move out-of-plane relatively to the outer ring because of the application of an external force $\mathcal{F}$ (Fig. 5.2). The surfaces of the dielectric elastomer membrane are coated with a pair of compliant electrodes, between which an electric potential difference ϕ can be applied, then producing an electric field through the membrane thickness. Due to the electromechanical loading, the membrane deforms non-homogeneously out-of-plane, as shown in Fig. 5.1a and in Fig. 5.2c.

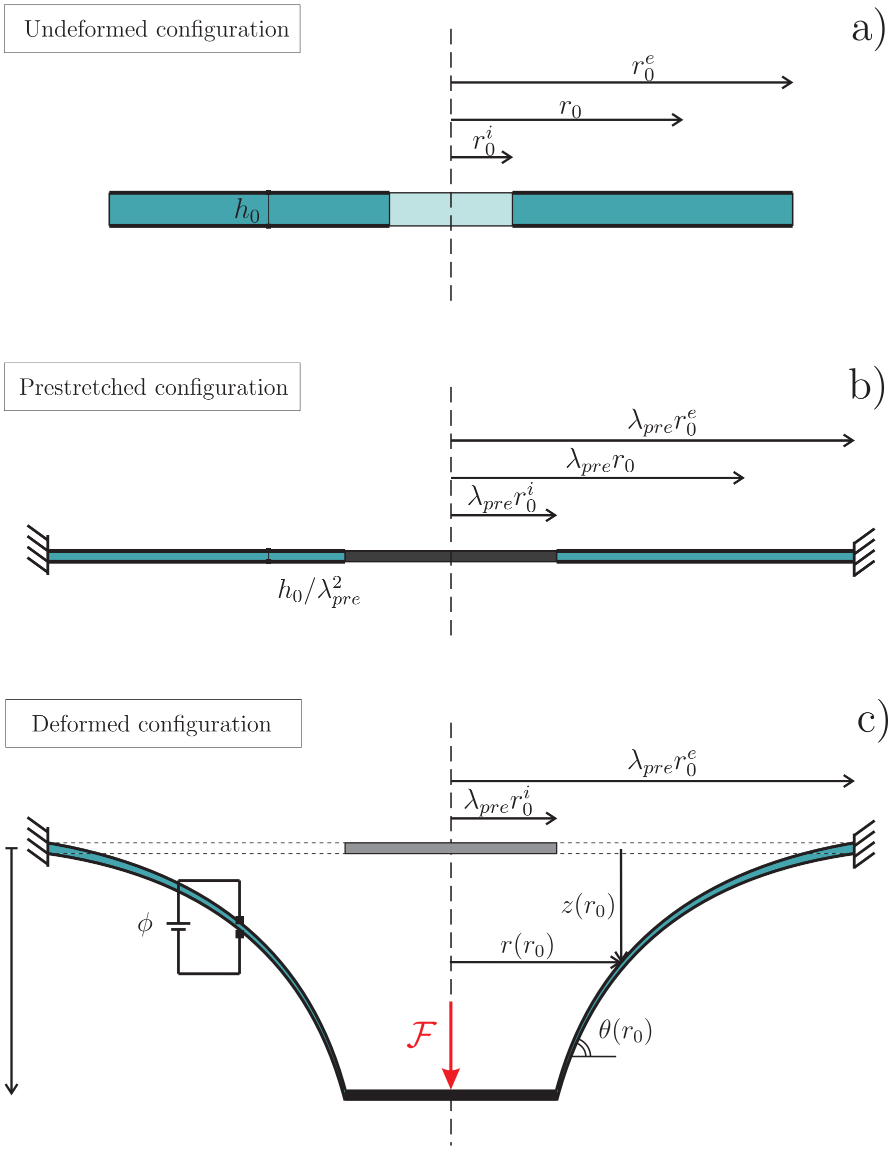
Undeformed configuration
a)
r_0^e
r_0
r_0^i
h_0
Prestretched configuration
b)
$\lambda_{pre}r_0^e$
$\lambda_{pre}r_0$
$\lambda_{pre}r_0^i$
h_0/λ_{pre}^2
Deformed configuration
c)
$\lambda_{pre}r_0^e$
$\lambda_{pre}r_0^i$
ϕ
u
$z(r_0)$
$r(r_0)$
$\mathcal{F}$
$\theta(r_0)$

FIGURE 5.2: Configurations of the annular membrane generator: a) undeformed, b) prestretched and c) deformed.

In the deformed configuration, the material point with initial position at a generic r_0 has coordinates $r(r_0)$ and $z(r_0)$, see Fig. 5.2. They have to fulfill the boundary conditions

$$r(r_0^i) = \lambda_{pre} r_0^i, \quad r(r_0^e) = \lambda_{pre} r_0^e, \quad z(r_0^e) = 0, \quad z(r_0^i) = u, \tag{5.1}$$

where u is the maximum transverse displacement. Denoting by $\mathrm{d}l$ the distance between two adjacent points in the deformed configuration and by $\theta(r_0)$ the slope of the vector connecting them, on the basis of simple trigonometric relations we can write $(\mathrm{d}l)^2 = (\mathrm{d}r)^2 + (\mathrm{d}z)^2$, where $\mathrm{d}r = \cos\theta\,\mathrm{d}l$ and $\mathrm{d}z = -\sin\theta\,\mathrm{d}l$. The longitudinal stretch at r_0 $\lambda_1(r_0)$ is defined as $\lambda_1 = \mathrm{d}l/\mathrm{d}r_0$ or, alternatively,

$$\lambda_1 = \frac{\mathrm{d}l}{\mathrm{d}r_0} = \sqrt{(r')^2 + (z')^2}, \tag{5.2}$$

where the notation $\bullet'$ indicates the first derivative of the quantity $\bullet$ with respect to R, i.e. $\bullet' = \mathrm{d}\bullet/\mathrm{d}R$. Due to the axisymmetry inherent in the problem, the circumferential stretch $\lambda_2(r_0)$ simply writes as $\lambda_2 = r/r_0$. The material is assumed to be incompressible, i.e. $J = \lambda_1\lambda_2\lambda_3 = 1$, and, as a consequence, the stretch in the thickness direction λ_3 of the membrane is given by

$$\lambda_3 = 1/(\lambda_1\lambda_2). \tag{5.3}$$

In the prestretched configuration, the membrane in-plane deformed is subjected to an homogeneous state of deformation, that is $\lambda_1 = \lambda_2 = \lambda_{pre}$ (see Fig. 5.2b).

As the membrane is thin, we assume that along the deformation electric displacement and electric fields remain always orthogonal to the membrane middle-plane. In the deformed configuration the total charge Q on the electrodes is

$$Q = 2\pi \int_{r_0^i}^{r_0^e} D^0(r_0) r_0 \,\mathrm{d}r_0, \tag{5.4}$$

where $D^0(r_0)$ is the nominal electric displacement, defined as the charge density per unit undeformed area.

It is convenient to choose the nominal electric displacement $\boldsymbol{D}^0$ as independent electrical variable, therefore, the material is assumed to be governed by an isotropic energy-density function $\mathcal{W}(\boldsymbol{F}, \boldsymbol{D}^0)$, cf. Sect. 2.2. In order to obtain the constitutive equations we can write the principle of energy conservation, as already done in Chap. 2 considering as free electrical variable the nominal electric field $\boldsymbol{E}^0$. Analogously to Eq. (2.12), we obtain

$$\left[\boldsymbol{S} - \frac{\partial\mathcal{W}}{\partial\boldsymbol{F}} + p\boldsymbol{F}^{-T}\right] \cdot \dot{\boldsymbol{F}} + \left[\boldsymbol{E}^0 - \frac{\partial\mathcal{W}}{\partial\boldsymbol{D}^0}\right] \cdot \dot{\boldsymbol{D}}^0 = 0\,. \tag{5.5}$$

A sufficient condition for (5.5) to be fulfilled is that

$$\boldsymbol{S} = \frac{\partial \mathcal{W}}{\partial \boldsymbol{F}} - p\boldsymbol{F}^{-T}\,, \qquad \boldsymbol{E}^0 = \frac{\partial \mathcal{W}}{\partial \boldsymbol{D}^0}\,, \tag{5.6}$$

where p is the indeterminate hydrostatic pressure. Recalling that, as a consequence of the incompressibility, λ_3 is a function of the longitudinal and circumferential stretches, from Eq. (5.3) and Eq. $(5.6)_1$ we can compute the hydrostatic pressure p by requiring the through-thickness stress S_{33} to be zero.

As a result of the incompressibility requirement (5.3), the state of a membrane element is fully described by the three functions $\lambda_1(r_0)$, $\lambda_2(r_0)$ and $D^0(r_0)$. Therefore, we can express the isotropic energy-density function as $\mathcal{W}(\lambda_1, \lambda_2, D^0)$. In this way, the incompressibility constraint is directly incorporated in the strain-energy function and we can explicit the constitutive equations as

$$S_{11} = \frac{\partial \mathcal{W}(\lambda_1, \lambda_2, D^0)}{\partial \lambda_1}, \qquad S_{22} = \frac{\partial \mathcal{W}(\lambda_1, \lambda_2, D^0)}{\partial \lambda_2}, \qquad E^0 = \frac{\partial \mathcal{W}(\lambda_1, \lambda_2, D^0)}{\partial D^0}. \tag{5.7}$$

From the balance of forces along z and the circumferential direction, see [59], we obtain the equilibrium equations for the membrane, namely

$$2\pi r_0 h_0 S_{11} \sin\theta = \mathcal{F}, \tag{5.8}$$

$$\frac{\mathrm{d}(r_0 S_{11}\cos\theta)}{\mathrm{d}r_0} = S_{22}. \tag{5.9}$$

In addition to the previous equations, the definition of nominal electric field gives

$$E^0 = \phi/h_0. \tag{5.10}$$

An explicit form of the free-energy function $\mathcal{W}(\lambda_1, \lambda_2, D^0)$ can be formulated assuming the material as an ideal dielectric. Under this assumption, the dielectric behaviour of the elastomer is unaffected by the deformation, i.e. $\boldsymbol{D} = \epsilon \boldsymbol{E}$, with the strain independent permittivity $\epsilon = \epsilon_r \epsilon_0$ (cf. Sect. 2.3).

To illustrate the main features of the load-driven out-of-plane DEG, we adopt the extended neo-Hookean energy-density function

$$\mathcal{W} = \frac{\mu}{2}[I_1 - 3] + \frac{1}{2\epsilon}K_5 = \frac{\mu}{2}\left(\lambda_1^2 + \lambda_2^2 + \frac{1}{\lambda_1^2\lambda_2^2} - 3\right) + \frac{1}{2\epsilon}\frac{D^{0^2}}{\lambda_1^2\lambda_2^2}, \tag{5.11}$$

where μ is the shear modulus of the material and where the invariants I_1 and K_5 are defined by Eqs. $(2.8)_1$ and $(2.11)_2$, respectively.

Substituting (5.11) in (5.7), we obtain the explicit form of the constitutive equations as

$$S_{11} = \mu\lambda_1 - \left(\mu + \frac{{D^0}^2}{\epsilon}\right)\frac{1}{\lambda_1^3\lambda_2^2}, \quad S_{22} = \mu\lambda_2 - \left(\mu + \frac{{D^0}^2}{\epsilon}\right)\frac{1}{\lambda_1^2\lambda_2^3}, \quad E^0 = \frac{D^0}{\epsilon}\frac{1}{\lambda_1^2\lambda_2^2}. \tag{5.12}$$

The same results cn be achieved using Eq. $(5.6)_1$, Eq. (5.3). The hydrostatic pressure p results to be

$$p = \left(\mu + \frac{{D^0}^2}{\epsilon}\right)\frac{1}{\lambda_1^2\lambda_2^2}. \tag{5.13}$$

From $(5.12)_3$ and (5.10), we can obtain the expression of the nominal dielectric displacement $D^0(r_0)$ as a function of the applied voltage

$$D^0(r_0) = \epsilon E^0 \lambda_1(r_0)^2\lambda_2(r_0)^2 = \epsilon\frac{\phi}{h_0}\lambda_1(r_0)^2\lambda_2(r_0)^2. \tag{5.14}$$

Substituting (5.14) into (5.4), we obtain the explicit expression of the total charge

$$Q = 2\pi\epsilon\frac{\phi}{h_0}\int_{r_0^i}^{r_0^e}\lambda_1(r_0)^2\lambda_2(r_0)^2 r_0\,\mathrm{d}r_0. \tag{5.15}$$

The equations of equilibrium along with the boundary conditions constitute a system of non-linear differential algebraic equations that can be numerically solved by employing the shooting method (Appendix C shows in detail the solving procedure).

5.2 The load-driven harvesting cycle for an out-of-plane DEG

The DE annular membrane undergoes a load-driven harvesting cycle, analogous to that delineated in Sect. 2.5, deforming non-homogeneously out-of-plane. In this case, the cycle is described in electrical terms by the total charge on the electrodes Q and by the voltage ϕ, while in mechanical terms it is characterised by the applied load $\mathcal{F}$ and by the maximum transverse displacement u. We concentrate now on the analysis of the I–II–I path on the right-hand side of Fig. 5.1b. In this four-stroke cycle, shown in more detail in Fig. 5.3, the load $\mathcal{F}$ and the total charge Q are alternately held constant. Specifically, it is composed by:

1. stroke A-B: the membrane is stretched by increasing the applied load from $\mathcal{F}^A = 0$ to $\mathcal{F}^B = \mathcal{F}_{max}$ under the open circuit condition. During this stage the total charge on the electrodes is fixed, so that $Q^A = Q^B = 0$;

2. stroke B-C: at the stretched configuration the total charge Q on the electrodes increases from $Q^B = 0$ to Q^C by applying a potential jump $\Delta\phi$. During this stage the load is held fixed, so that $\mathcal{F}^B = \mathcal{F}^C = \mathcal{F}_{max}$;
3. stroke C-D: the elastomer is open-circuit released by decreasing the load from $\mathcal{F}^C = \mathcal{F}_{max}$ to $\mathcal{F}^D = 0$. The charge is then kept constant, $Q^D = Q^C$. Note that during this phase both the potential between the two electrodes and the electric field increase, attaining their maximal values at the end of this stroke. The obtained potential jump during this phase is $\phi^D - \phi^C$.
4. stroke D-A: the surplus charge $Q^D - Q^A$ is harvested at high potential to the storage battery, while the load is held constant so that $\mathcal{F}^D = \mathcal{F}^A = 0$.

The cycle is presented on the thermodynamical planes shown in Fig. 5.3 and the measure of the area of the cycle on both planes is equal to the harvested energy H_g. The first plot of Fig. 5.3b corresponds to the electrical ϕ–Q plane and the second one to the mechanical $\mathcal{F}$–u plane. We note that, in practice, strokes B–C and D–A are substantially shorter than the mechanical loading and unloading steps. Thus, as explained in Sect. 2.5, the applied external force should be regarded as a continuously oscillating force such that appropriate electrical circuits are temporarily connected to the electrodes when it attains its maximal and minimal values.

We recall that the process here presented is ideal, since we assume instantaneous charging and lossless behaviour of the DE membrane, the electrodes and of the electric circuits.

The feasible working cycle is constrained by the several failure modes of which DEs are susceptible, as explained in Sect. 2.6. In the following analysis we will take into account the electric breakdown EB, the ultimate stretch λ_U, the loss of the tensile stress state ($S_{22} = 0$) and the electromechanical instability EMI.

5.3 Harvested energy, efficiency, and performance evaluation

The performance of the device is evaluated on the basis of (i) the harvested energy H_g along the cycle and (ii) of the efficiency η. Eq. (2.58) defines the latter as the modulus of the ratio of H_g on the total invested energy H_i from step A to step C, which is composed of two contributions: mechanical work, W_{mech}, and electrical work, W_{el}. Therefore, we can rewrite Eq. (2.58) as

$$\eta = \left|\frac{H_g}{H_i}\right| = \left|\frac{H_g}{W_{mech} + W_{el}}\right|. \tag{5.16}$$

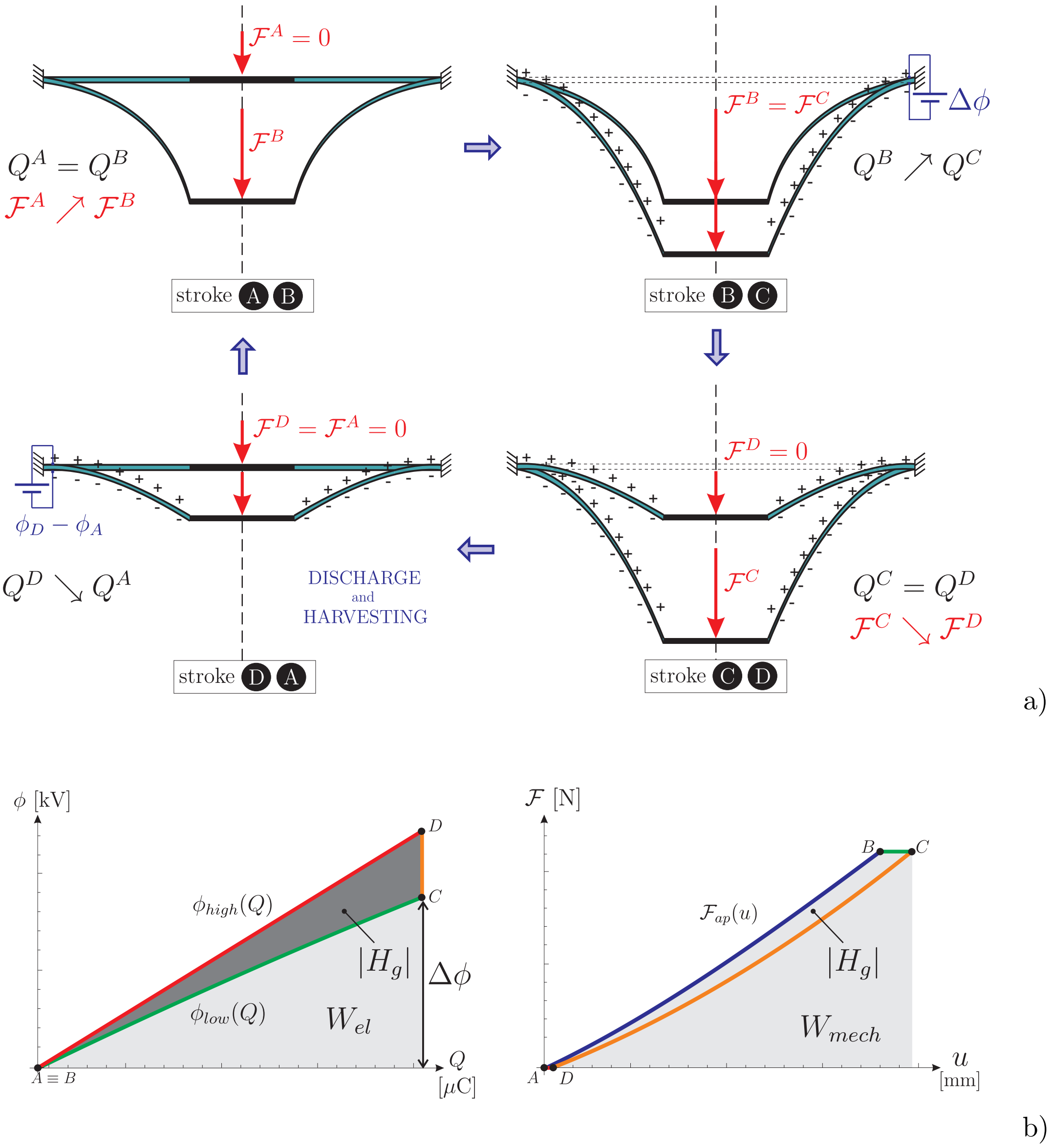

$\mathcal{F}^A = 0$
$\mathcal{F}^B$
$Q^A = Q^B$
$\mathcal{F}^A \nearrow \mathcal{F}^B$
stroke A B
$\mathcal{F}^B = \mathcal{F}^C$
$\Delta\phi$
$Q^B \nearrow Q^C$
stroke B C
$\mathcal{F}^D = \mathcal{F}^A = 0$
$\phi_D - \phi_A$
$Q^D \searrow Q^A$
DISCHARGE
and
HARVESTING
stroke D A
$\mathcal{F}^D = 0$
$\mathcal{F}^C$
$Q^C = Q^D$
$\mathcal{F}^C \searrow \mathcal{F}^D$
stroke C D
a)
ϕ [kV]
D
C
$\phi_{high}(Q)$
$|H_g|$
$\Delta\phi$
$\phi_{low}(Q)$
W_{el}
Q
[μC]
$A \equiv B$
$\mathcal{F}$ [N]
B
C
$\mathcal{F}_{ap}(u)$
$|H_g|$
W_{mech}
u
[mm]
A
D
b)

FIGURE 5.3: The investigated harvesting cycle: a) illustration of the four strokes along the I–II–I path with a service battery at the right and a storage battery at the left b) plot of the cycle on the electrical Q–ϕ plane and on the mechanical $\mathcal{F}$–u plane. The measure of the area of the cycle, on both planes, is equal to the modulus of the harvested energy, $|H_g|$. The light-grey shaded areas represent the electrical and the mechanical work invested into the conversion process.

On both the mechanical and the electrical plane, the measure of the area of the cycle equates $|H_g|$ (Fig. 5.3b). Hence, we can simply compute numerically H_g evaluating the following integrals

$$H_g = \int_0^{Q_{max}} \phi_{low}(Q) \mathrm{d}Q + \int_{Q_{max}}^0 \phi_{high}(Q) \mathrm{d}Q, \tag{5.17}$$

VHB-4910			
μ [kPa]	ϵ_r	ρ [kg/m^3]	E_{eb} [kV/mm]
35	4.5	960	50

TABLE 5.1: Electromechanical properties of VHB-4910.

where $\phi_{high}(Q)$ and $\phi_{low}(Q)$ are the functions on the electrical plane relative to strokes D–A and B–C, respectively; moreover, $Q_{max} = Q^C = Q^D$ is the maximum total charge reached in the cycle. Note that the energy is extracted from the system and thus H_g is negative.

The mechanical work W_{mech} invested in the cycle from A to C corresponds to

$$W_{mech} = \int_0^{u^B} \mathcal{F}_{ap}(u)\,\mathrm{d}u + \mathcal{F}_{max}(u^C - u^B), \tag{5.18}$$

where $\mathcal{F}_{max} = \mathcal{F}^B = \mathcal{F}^C$, and the applied load $\mathcal{F}_{ap}(u)$ in stroke A–B is numerically evaluated. In the computations, to avoid the planar configuration where the governing equation (5.8) loose meaning, we assume that in A a small force of 1 N is applied.

Finally, the electrical work W_{el} provided to the cycle along B–C is given by the integral

$$W_{el} = \int_0^{Q_{max}} \phi_{low}(Q)\,\mathrm{d}Q. \tag{5.19}$$

In the simulations, we adopt typical parameters of VHB-4910 whose electromechanical properties are reported in Tab. 5.1. This choice will allow us a performance comparison among generators analysed in Chap. 3 and Chap. 4 (see also [6, 57]), made up of the same material, but with different geometries, all mechanically activated by the same principle: an external oscillating driving force able to reach a maximum value.

The undeformed thickness h_0 of the membrane is taken equal to 1 mm in all the examined cases. Moreover, in order to integrate the governing equations and solve the electromechanical boundary-value problem, we fix the value of the undeformed external radius r_0^e at 500 mm. The gained energy will be always referred to the unit mass of the polymer, then, according to Eq. $(2.62)_1$, we introduce the variable

$$\hat{H}_g = \frac{|H_g|}{\rho\pi({r_0^e}^2 - {r_0^i}^2)h_0}.$$

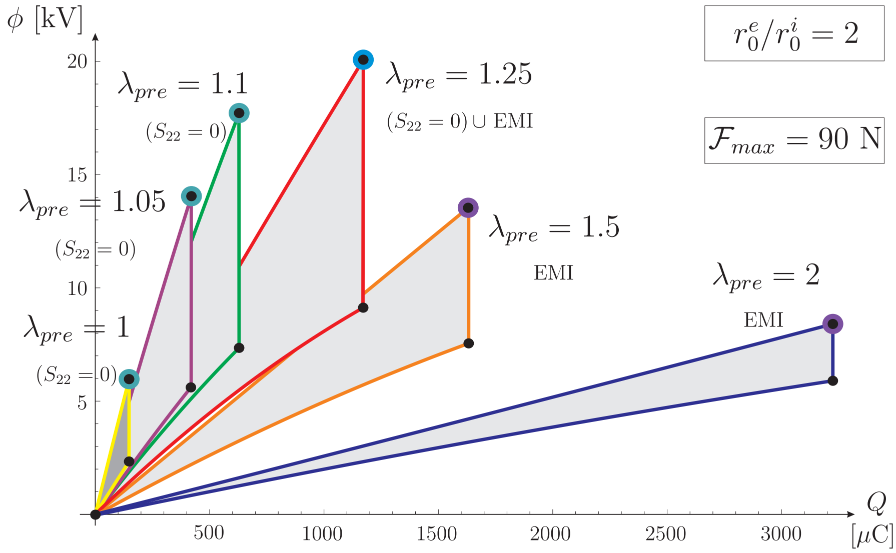

FIGURE 5.4: Influence of the prestretch on the performance of a generator with $r_0^e/r_0^i = 2$. Plot on the electrical ϕ–Q plane of the optimal cycle for different prestretch values, namely $\lambda_{pre} = 1$, 1.05, 1.1, 1.25, 1.5 and 2, and $\mathcal{F}_{max} = 90$ N. The relevant failure mode is indicated below the prestretch label.

5.3.1 Influence of the prestretch

In electroactive devices, VHB films are usually prestretched before being electrically activated. Then, we firstly focus our attention on the influence of the prestretch λ_{pre}, at constant $\mathcal{F}_{max}$, on the generator performance. We consider a configuration characterised by a radius ratio equal to two, $r_0^i = r_0^e/2$. This value is justified as we will show that it corresponds to one of the more efficient configurations, moreover this radius ratio has been investigated in previous works dealing with electroactive annular membrane devices [24, 63, 64].

After a careful inspection, we decided to set the maximum applied force $\mathcal{F}_{max} = 90$ N, so that, in the unprestretched configuration ($\lambda_{pre} = 1$), the maximum stretch attained during the cycle is approximately equal to two ($\lambda_{max}|_{\lambda_{pre}=1} \approx 2$). Then, we have increased the prestretch and subjected the membrane to a combination of electromechanical loadings to reach one of the possible failure listed in the previous Section. Later on, the change in the applied maximum force at a given prestretch will be analysed.

Fig. 5.4 reports an effective sketch of the cycle evolution at increasing λ_{pre} onto the electrical ϕ–Q plane. Six representative values of the prestretch are analysed in the range $1 \leq \lambda_{pre} \leq 2$. Increasing this parameter, the area of the cycle enlarges, due to the rise of both the charge and the maximum voltage ϕ_D, till $\lambda_{pre} = 1.25$, then decreases monotonically. The leading failure takes always place at point D (see the marked spots

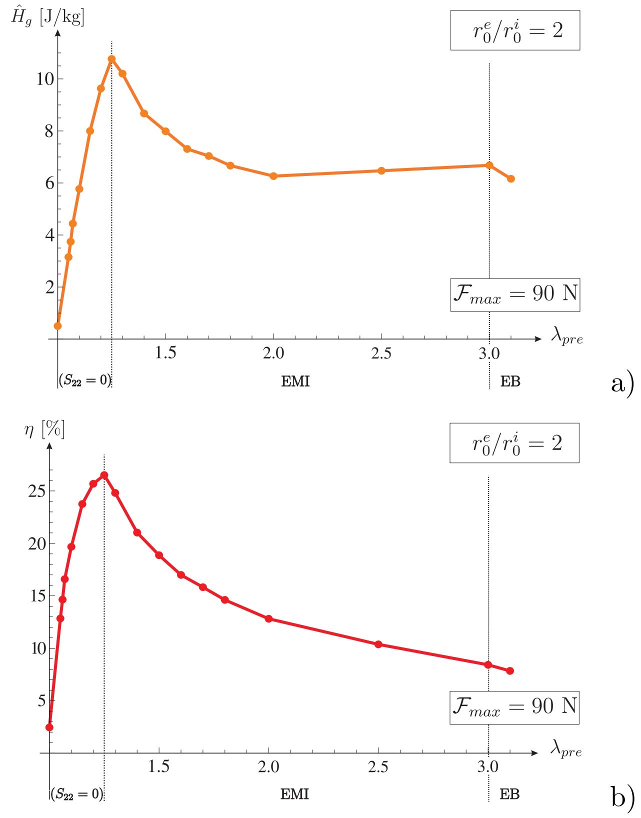

FIGURE 5.5: Influence of the prestretch λ_{pre} on the performance of a generator with $r^e_0/r^i_0 = 2$, $\mathcal{F}_{max} = 90$ N: a) gained energy per unit mass $\hat{H}_g$ and b) efficiency η. The failure mode in the relevant prestretch range is reported below the horizontal axis.

in Fig. 5.4): at low prestretches, it is due to loss of the tensile stress state ($S_{22} = 0$), whereas at a higher prestretch the crisis is associated with electromechanical instability EMI at a point of a membrane on the inner boundary ($r_0 = r^i_0$). These two failures occur simultaneously at the threshold $\lambda_{pre} = 1.25$.

This failure change is a clear sign of the existence of different working regimes for the generator. For $\lambda_{pre} < 1.25$, the device works at low charge and high voltage, while for high prestretches the working regime is characterised by high charge and low voltage. Numerical data reported in Tab. 5.2 shows that cycles at $\lambda_{pre} = 2$ and 1.1 are nearly equivalent with respect to the amount of harvested energy, but the working regime of the devices is markedly different and this fact is reflected in a strong efficiency difference.

Fig. 5.5 summarises the main performance indicators ($\hat{H}_g$ and η) for the investigated generator, extending the analysis up to $\lambda_{pre} = 3.1$. It can be noticed that EB failure comes into play for $\lambda_{pre} \geq 3$ at the state C, at the inner boundary. In these cases, the harvested energy per unit mass $\hat{H}_g$ drops down at constant maximum current electric field E_{max}. In any case, $\lambda_{pre} = 1.25$ represents the optimal value both in terms of

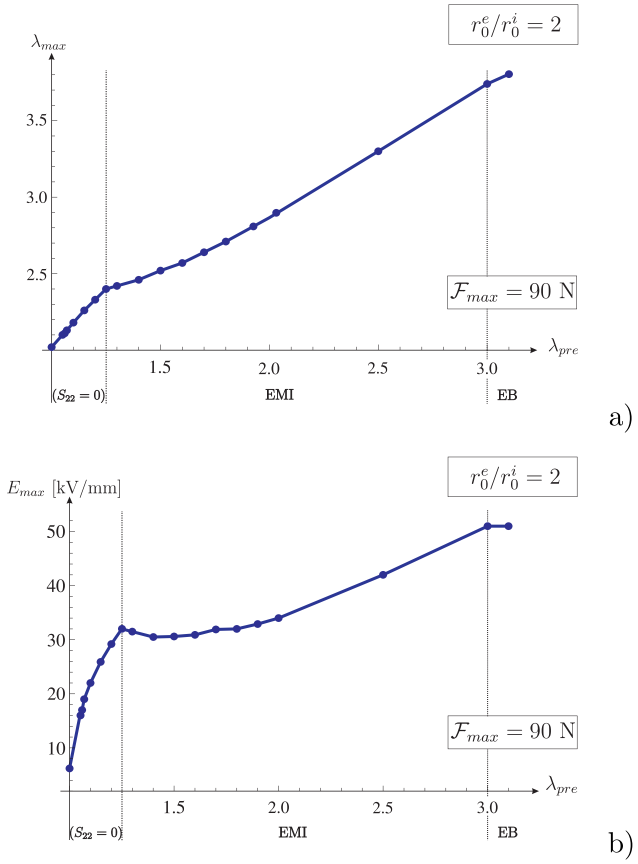

FIGURE 5.6: Influence of the prestretch λ_{pre} on the performance of a generator with $r_0^e/r_0^i = 2$, $\mathcal{F}_{max} = 90$ N: a) maximum stretch λ_{max} and b) maximum current electric field E_{max}. The failure mode in the relevant prestretch range is reported below the horizontal axis.

harvesting energy (part a of the figure) and efficiency (part b), being, for $\lambda_{pre} > 1.25$, the efficiency drop more pronounced than that of the energy.

Fig. 5.6 reports the maximum stretch and maximum electric field experienced by the generator, where the three working regimes are still evident. It is important to remark that at the optimal prestretch value the electrical/mechanical stresses are definitely not severe ($\lambda_{max} = 2.399 \approx 2.4$, $E_{max} = 32$ kV/mm) and this suggests the possibility to exploit the same DEG configuration for higher driving force $\mathcal{F}_{max}$.

Thus, as a partial conclusion, the initial prestretch of the plane membrane is a crucial issue in the design of an enhanced annular DEG working out-of-plane. Tab. 5.2 collects the main physical quantities for the cycles considered in Fig. 5.4. We note that higher values of the obtained voltage jump $(\phi^D - \phi^C)$ correspond to higher efficiency values.

$r_0^e/r_0^i = 2$							
λ_{pre}	$\hat{H}_g$ [J/kg]	$\delta\hat{H}_g$	η [%]	$\delta\eta$	$\Delta\phi$ [kV]	$\phi^D - \phi^C$ [kV]	Failure mode
1	0.487	—	2.45	—	2.345	3.65	$(S_{22} = 0)$
1.05	3.150	6.5	12.84	5.2	5.650	8.35	$(S_{22} = 0)$
1.1	5.768	11.8	19.67	8.0	7.340	10.16	$(S_{22} = 0)$
1.25	10.767	22.1	26.51	10.8	9.015	10.78	$(S_{22} = 0) \cup$ EMI
1.5	7.987	16.4	18.87	7.7	7.520	6.08	EMI
2	6.264	12.9	12.81	2.5	5.878	2.62	EMI

Table 5.2: Influence of the prestretch λ_{pre} on the performance of a generator with $r_0^e/r_0^i = 2$. Gained energy per unit mass $\hat{H}_g$, efficiency η, supplied voltage $\Delta\phi$ and obtained voltage jump $\phi^D - \phi^C$ are reported. For each examined prestretch the failure mode experienced by the device is listed. Furthermore, the improvement in the gained energy $\delta\hat{H}_g$ and in the efficiency $\delta\eta$ with respect to the unprestretched case ($\lambda_{pre} = 1$) are quantified.

5.3.2 Influence of the radius ratio

We draw now the attention on the relative dimensions of the annular membrane by analysing generators characterised by different radius ratios, namely $r_0^e/r_0^i = 1.5$, 2, 2.5 and 4 (still $r_0^e = 500$ mm). In order to investigate a comparable range of prestretch values, we set for each device the maximum applied load so that, in the unprestretched configuration, the maximum stretch attained in the cycle is the same for all ($\lambda_{max} \approx 2$).

DEGs characterised by radius ratios of 1.5, 2 and 2.5 show a similar behaviour, at least in terms of optimal prestretch (i.e. $\lambda_{pre} = 1.25$) and efficiency (see Fig. 5.7b and Tab. 5.3). At the optimal prestretch, the energy per unit mass harvested by these three devices is almost inversely proportional to the radius ratio (Fig. 5.7a), and the best performance is entailed by that with the smaller radius ratio (1.5). For high prestretches, instead, the generators with $r_0^e/r_0^i = 2$ and 2.5 convert nearly the same amount of energy, while that with r_0^e/r_0^i =1.5 performs better.

With the ratio $r_0^e/r_0^i = 4$, the behaviour of the generator changes markedly. The peak in the efficiency and in the harvested energy takes place at 12.5% of initial stretch, i.e. half of the optimal prestretch for the other cases. Moreover, for $\lambda_{pre} > 1.125$ the failure is still due to electromechanical instability EMI, but the crisis is anticipated at state C of the cycle, hence at the most deformed configuration of the generator.

Furthermore, in the optimal configuration, numerical data shows that the generators with radius ratio close to 2 allow a higher voltage jump against a smaller applied voltage (or equal in the case $r_0^e = 2.5r_0^i$), while the generator with the radius ratio equal to 4 requires a higher applied voltage against a lower obtained voltage jump (see Tab. 5.3).

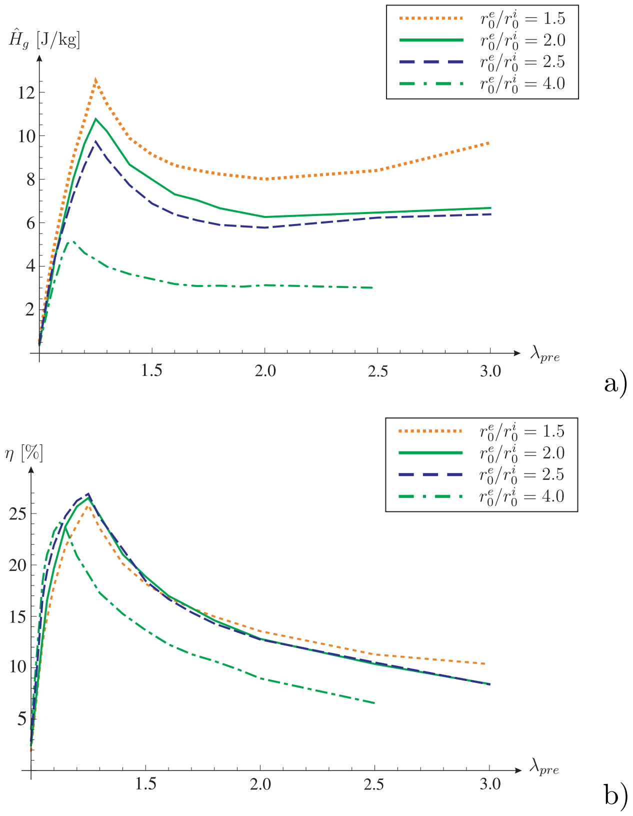

FIGURE 5.7: Influence of the radius ratio r_0^e/r_0^i on the performance of the generator for different prestretches: a) gained energy per unit mass $\hat{H}_g$ and b) efficiency η.

r_0^e/r_0^i	r_0^i [mm]	$\mathcal{F}_{max}$ [N]	λ_{pre}	$\hat{H}_g$ [J/kg]	η [%]	$\Delta\phi$ [kV]	$\phi^D - \phi^C$ [kV]
1.5	333	120	1.25	12.515	25.84	8.02	11.88
2.0	250	90	1.25	10.767	26.51	9.05	10.79
2.5	200	72	1.25	9.723	26.91	9.85	9.85
4.0	125	45	1.125	5.051	24.12	10.58	7.92

TABLE 5.3: Influence of the radius ratio on the generator performance: internal radius r_0^i ($r_0^e = 500$ mm), and maximum applied load $\mathcal{F}_{max}$. For the best performance of the generator, the prestretch λ_{pre}, the gained energy per unit mass $\hat{H}_g$, the efficiency η, the applied voltage $\Delta\phi$ and the obtained voltage jump $\phi^D - \phi^C$ are reported.

5.3.3 Influence of the maximum applied load

The previous analysis has clarified that a radius ratio equal to 2 allows to leverage the material obtaining a good performance in terms of both gained energy and efficiency.

In order to identify the optimal maximum applied load for this configuration, we compute both the efficiency and the harvested energy as a function of the applied load for different prestretches, namely $\lambda_{pre} = 1.15$, 1.25, 1.5 and 2.5. The load is increased until the maximum stretch λ_{max} reaches the ultimate value $\lambda_U = 4$.

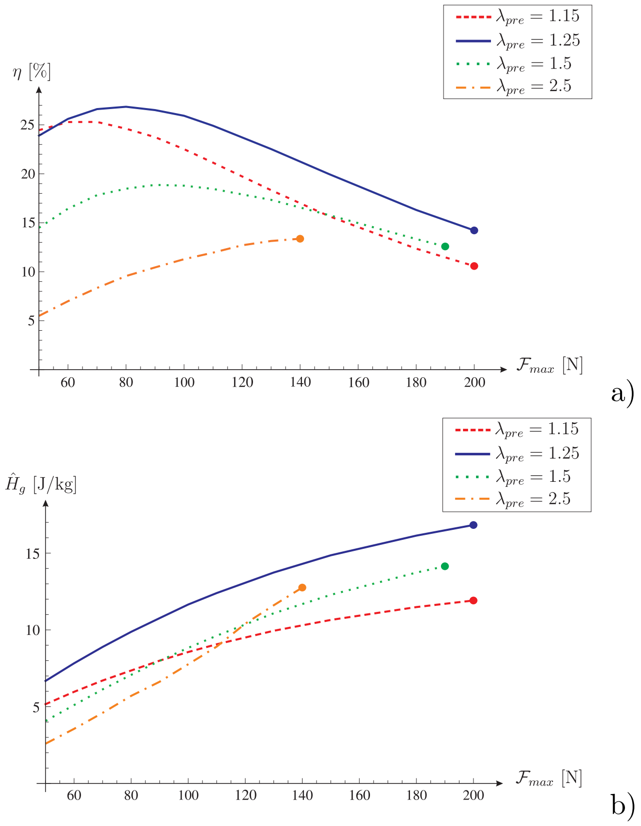

FIGURE 5.8: Influence of the maximum applied load $\mathcal{F}_{max}$ on a) the efficiency η and b) the gained energy per unit mass $\hat{H}_g$ of a generator with $r_0^e/r_0^i = 2$. A dot at the end of a curve indicates that one stretch in the membrane has reached the ultimate value $\lambda_{max} = \lambda_U = 4$ (in all cases $\lambda_1 = \lambda_{max}$).

The data, obtained varying the maximum applied load in the range between 50 N and 200 N, shows that, on the one hand, prestretch $\lambda_{pre} = 1.25$ ensures a overall higher efficiency with a peak (26.85%) for a value of $\mathcal{F}_{max} = 80$ N, see Fig. 5.8a, where the attainment of the failure associated with maximum stretch ($\lambda_{max} = \lambda_U = 4$) is indicated by a dot terminating the relevant curve. On the other hand, the prestretch $\lambda_{pre} = 1.25$ ensures the highest amount of specific gained energy with respect to the other prestretches, but the harvested energy increases almost proportionally to the maximum applied load, as depicted in Fig. 5.8b.

Hence, in the selection of the maximum applied load for a given membrane, it is important to find a good compromise among high harvested energy and high efficiency. For the generator with $r_0^e/r_0^i = 2$ and $\lambda_{pre} = 1.25$, in the light of results displayed in Fig. 5.8a, the anticipated choice of setting the maximum load at 90 N showed to be reasonable.

5.4 Comparison of different DEG materials and configurations

The energy harvesting technique based on soft dielectric elastomers is not yet an established technology and further investigation is needed in order to select the best suitable material and configuration for each design. This Section is aimed at comparing the behaviours of two different materials for the annular membrane (the acrylic VHB and a type of natural rubber already employed in the literature) and, only for the VHB material, the performance of the same geometry with that of a planar membrane deforming both in plane-strain and equibiaxially.

5.4.1 Comparison of different DEG materials

For an annular membrane generator with a radius ratio of two and $h_0 = 1$ mm it is interesting to compare, on the basis of the best performance in terms of both (*i*) efficiency η and (*ii*) gained energy per unit mass $\hat{H}_g$, a VHB device with a generator made up of natural rubber (ZruElast A1040), whose mechanical properties are recalled in Tab. 5.4 [31]. See Sect. 4.4 for details on the ZruElast A1040.

ZruElast A1040			
μ [kPa]	ϵ_r	ρ [kg/m^3]	E_{eb} [kV/mm]
917	3.4	945	120

TABLE 5.4: Electromechanical properties of the natural rubber ZruElast A1040 [31].

Following the same procedure employed in the performance analysis of the VHB generator (see Sect. 5.3), we can determine, for the natural rubber, the couples $(\mathcal{F}_{max}, \lambda_{pre})$ providing the best efficiency and the maximum harvested energy, the latter still imposing $\lambda_{max} = \lambda_U = 4$. These are reported in left-hand sides of Tabs. 5.5a and 5.5b, respectively, and correspond to (1500 N, 1.10) and to (5000 N, 1.10), respectively. It is worth noting that for this material, differently from VHB, the optimal prestretch separates two failure ranges associated with EB and $(S_{22} = 0)$ – loss of the tensile stress state in the circumferential direction.

Data summarising the performance of the two DEGs at ***maximum efficiency*** are shown in the central part of Tab. 5.5a. The efficiency of the natural rubber system is slightly lower than that of the acrylic one (approximately -5.8%), while the gained energy per unit mass $\tilde{H}_g$ is markedly higher, as it is well known that the harvested energy is proportional to the shear modulus of the material at the same maximum stretch (in turn, this requires a considerably higher driving force, i.e. $\mathcal{F}_{max}$), see also [6, 31, 37].

Maximum efficiency η							
Material	$\mathcal{F}_{max}$ [N]	λ_{pre}	λ_{max}	η [%]	$\hat{H}_g$ [J/kg]	n	$n\|H_g\|$ [kJ]
VHB-4910	80	1.25	2.4	26.85	9.87	425	2.73
ZruElast	1500	1.10	1.7	21.06	95.04	23	1.24

Table 5.5a: Performance comparison of devices made up of two different materials working at maximum efficiency. Left-hand and central parts of the table refer to the behaviour of a single membrane. The right-hand side of the table reports the performance of multi-membrane systems subjected to a total maximum force $\mathcal{F}_{tot} = 34$ kN: n, number of layers required; $n|H_g|$, total energy harvested.

Maximum energy $\hat{H}_g$							
Material	$\mathcal{F}_{max}$ [N]	λ_{pre}	λ_{max}	η [%]	$\hat{H}_g$ [J/kg]	n	$n\|H_g\|$ [kJ]
VHB-4910	200	1.25	4	14.22	16.83	170	1.62
ZruElast	5000	1.10	4	7.22	187.34	7	0.75

Table 5.5b: Performance comparison of devices made up of two different materials working at maximum energy. Left-hand and central parts of the table refer to the behaviour of a single membrane. The right-hand side of the table reports the performance of multi-membrane systems subjected to a total maximum force $\mathcal{F}_{tot} = 34$ kN: n, number of layers required; $n|H_g|$, total energy harvested.

A fair method to compare the two materials is to compute the amount of energy that a certain number n of annular membranes (to be determined) connected in parallel are able to harvest at a given external force $\mathcal{F}_{tot}$, as depicted in Fig. 5.1c. The comparison of the systems (for $\mathcal{F}_{tot} = 34$ kN) designed employing the two materials is summarised in the right-hand side of Tab. 5.5a. Due to the values of $\hat{H}_g$ of the single membranes, the number n of required acrylic layers is extremely higher with respect to that of the ZruElast. However, the total energy harvested by the multi-layer device $n|H_g|$ is higher for the VHB generator. The reason lays in the different maximum stretch λ_{max} reached by the two materials: the one attained by an acrylic membrane is approximately 1.5 times the one reached by a rubber film, cf. Tab. 5.5a. As it has been demonstrated in the previous Chapters, the energy increases proportionally to the maximum stretch attained by the DE membrane during the cycle, see also [6].

The comparison with respect to the ***maximum gained energy*** is reported in the left-hand side of Tab. 5.5b. The VHB generator entails a higher efficiency, but an extremely lower gained energy with respect to the ZruElast one. Analogously to the previous case, if we think to equally distribute a total acting force $\mathcal{F}_{tot}$ of 34 kN on a number of layers, due to the relatively higher stiffness of the natural rubber, the ZruElast generator requires 7 membranes, while the VHB device 170. However, even in this case, the total energy harvested by the multi-layer device is higher for the latter generator.

The choice of the material depends on a number of factors, such as operational conditions and durability. For instance, VHB displays a higher viscoelastic response than the natural rubber, however the latter, being an organic compound, exhibits a marked ageing and degradation due to chemical interaction with the environment [18].

Focusing on the total energy harvested by the multi-layer devices based on the two different design strategies, those maximising the efficiency allow to harvest the highest total energy $n|H_g|$, contrary to what happen for a plate DEG (see [6]), even if the energy gained by the single membrane is lower with respect to the single-membrane DEGs optimised with respect to the energy. This is due to the fact that the maximum load required by the energy–optimum membrane is approximately $2.5 \div 3$ times that needed by the efficiency–optimum cycle. As a consequence the number of layers n (and thus also the total harvested energy) required by the energy–optimum multi-membrane device is $1/2.5 \div 1/3$ that required by the efficiency–optimum multi–membrane DEG.

5.4.2 Comparison of different DEG configurations

$\lambda_{max} = 2.4$		
DEG loading conditions	$\hat{H}_g$ [J/kg]	η [%]
Out-of-plane	10.767	26.5
Plane-strain, ref. [57]	7.645	11.0
Equibiaxial, ref. [6]	27.804	18.8

Table 5.6a: Performance comparison at $\lambda_{max} = 2.4$ for different prototype generator configurations, acrylic material properties (VHB-4910)

$S_{max} = 70$ kPa		
DEG loading conditions	$\hat{H}_g$ [J/kg]	η [%]
Out-of-plane	10.767	26.5
Plane-strain, ref. [57]	6.770	12.0
Equibiaxial, ref. [6]	24.769	19.2

Table 5.6b: Performance comparison at $S_{max} = 70$ kPa for different prototype generator configurations, acrylic material properties (VHB-4910)

We focus now on the comparison between different generator prototype configurations, based on the acrylic material (VHB-4910)(properties listed in Tab. 5.1). We examine: (i) an annular membrane as investigated in Sect. 5.3 ($r_0^e/r_0^i = 2$, $r_0^e = 500$ mm, $h_0 = 1$ mm, $\lambda_{pre} = 1.25$, $\mathcal{F}_{max} = 90$ N) following a I–II–I path; (ii) a planar membrane DEG following an optimised cycle deforming under plane-strain conditions (see Chap. 3 and [57] for all details); (iii) a planar membrane DEG deforming equibiaxially (cf. Chap. 4 and [6]). In particular comparisons between energy per unit mass are made with respect to two limit conditions set by the operational characteristics of the optimised out-of-plane DEG: (A) all devices reach the maximum stretch $\lambda_{max} = 2.4$ along the relevant cycle (see data in Tab. 5.6a); (B) all devices reach the maximum nominal stress $S_{max} =$

$\max\{S_{11}, S_{22}\} = 70$ kPa along the relevant cycle (Tab. 5.6b). In both cases the highest energy per unit mass is provided by the planar membrane deforming equibiaxially, but the best performance in terms of efficiency is attained by the out-of-plane DEG. The membrane deforming under plane-strain conditions always exhibits inferior performance, however this configuration can be definitely enhanced by a transverse prestretch. It is important to underline that in the comparison between the two best geometries, the annular generator can follow a complete path I–IV along the same range of forces (Fig. 5.1b), therefore the energy that is potentially able to collect is two times the amount listed in the table (equal to 21.534 J/kg).

Chapter 6

Viscoelastic DEG operating in an electric circuit for energy harvesting

Recalling some fundamental concepts introduced in the previous Chapters, a soft dielectric generator, in its basic configuration, consists of a block of thin soft dielectric elastomer with dimensions $l_0 \times l_0 \times h_0$ in the reference configuration $\mathcal{B}_0$. In the case analysed in this Chapter, the device is assumed to deform homogeneously and is loaded by in-plane external oscillating forces represented by the nominal stress components $S_{11}(t)$ and $S_{22}(t)$, as depicted in Fig. 6.1a. The two opposite surfaces are treated so as to act like compliant electrodes inducing, neglecting fringing effects, a nominal time-dependent electric field $E^0(t)$ directed along $\boldsymbol{e}_3$-direction. Related to the deformation history the dimensions of the elastomer vary as a function of the time-dependent principal stretches $\lambda_i(t)$, with $i = 1, 2, 3$, to reach, at a certain time t, the current dimensions $l_1 = l_0\,\lambda_1(t)$, $l_2 = l_0\,\lambda_2(t)$ and $h = h_0\,\lambda_3(t)$.

This generator can generally be modelled as a stretch-dependent variable plane capacitor, the capacitance C of which is defined as

$$C(t) = \epsilon\,\frac{A}{h} = \epsilon\,\frac{l_0^2}{h_0}\,\frac{\lambda_1(t)\lambda_2(t)}{\lambda_3(t)}\,. \tag{6.1}$$

In a real device, however, the dielectric material shows a certain conducting current, also denoted as leakage current i_{Ri}, while the electrodes have a non-negligible resistance. Hence, a more realistic electrical model of the generator is a variable capacitor connected in parallel to a resistor R_i, representing the electrical resistance of the dielectric film, and

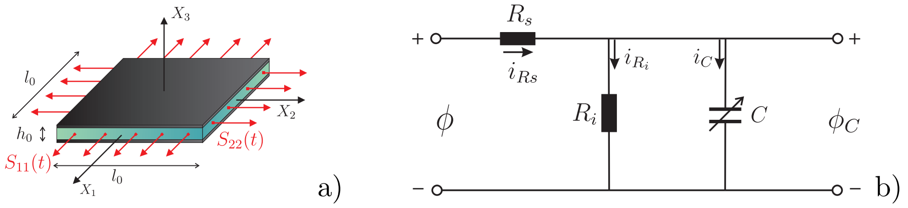

FIGURE 6.1: Soft dielectric elastomer generator: a) reference configuration and b) scheme of the equivalent circuit diagram.

connected in series to a resistor R_s, representing the electrical resistance of electrodes and wires, as shown in Fig. 6.1b, see [54].

Furthermore, the charge Q exchanged by the system is given by the sum of the time-integral of the leakage current and the product of capacitance and voltage of the soft variable capacitor,

$$Q(t) = \int_0^t i_{Ri}(\tau)\,\mathrm{d}\tau + C(t)\phi_C(t)\,. \tag{6.2}$$

6.1 A simple real harvesting circuit

In a real energy harvesting application, the generator operates in an electrical circuit achieved by connecting the dielectric elastomer generator in parallel to a battery through a diode and to an electrical load, as illustrated in Fig. 6.2. The battery supplies the circuit with a difference in the electric potential $\phi_o(t)$. In the analysis of the circuit, we assume that the voltage supplied by the battery is zero at the initial time $t = 0$ and then increases linearly during the semi-period $T/2$ of the stretch oscillation up to the value ϕ_o, namely

$$\phi_o(t) = t\,\frac{\phi_o}{T/2} \quad \text{for} \quad 0 < t < T/2\,. \tag{6.3}$$

Thereafter, for $t > T/2$, the supplied voltage is kept constant, i.e.

$$\phi_o(t) = \phi_o \quad \text{for} \quad t > T/2\,.$$

The electrical load is represented by the external resistor R_{ext}. The impedance of the load has to be sufficiently high so that the charge is maintained constant during the release of the elastomer and, as a consequence, the voltage on the dielectric elastomer is increased with respect to the constant value ϕ_o supplied by the battery.

The diode prevents the charge from flowing from the generator to the battery during the release phase. Its current $i_D(t)$ is modelled according to the classical Shockley diode

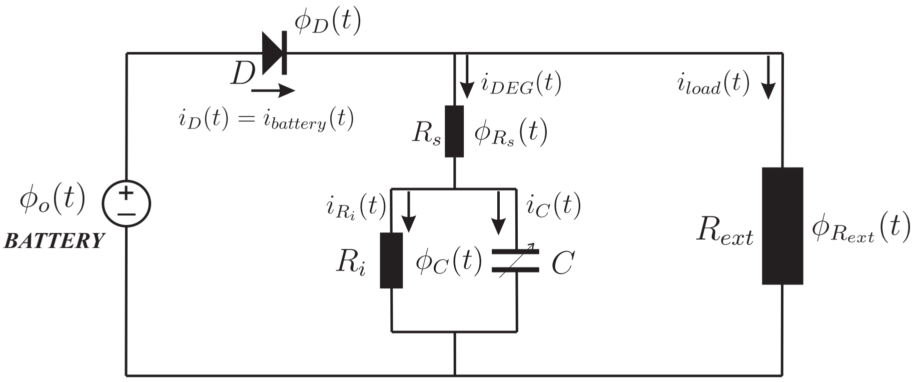

FIGURE 6.2: Scheme of the electrical circuit in which the dielectric elastomer generator operates.

equation

$$i_D(t) = I_s \left[\exp\left(\frac{\phi_D(t)}{n\, v_{\mathcal{T}}} \right) - 1 \right], \tag{6.4}$$

where I_s is its saturation current, $v_{\mathcal{T}}$ the thermal voltage, n the ideality factor with $1 < n < 2$, and $\phi_D(t)$ the diode voltage. The thermal voltage depends on the Boltzmann constant K, the temperature $\mathcal{T}$ and on the elementary charge $q_e = 1.60217653 \times 10^{-19}$ C, as $v_{\mathcal{T}} = K\mathcal{T}/q_e$.

In the case where the components of a circuit are connected in series, the total voltage is equal to the sum of the voltage on each of the components. By applying Kirchhoff's voltage law to the circuit one obtains

$$\phi_o(t) = \phi_D(t) + \phi_{Rs}(t) + \phi_C(t)\,, \tag{6.5}$$

$$\phi_o(t) = \phi_D(t) + \phi_{Rext}(t)\,, \tag{6.6}$$

where $\phi_C(t)$ is the voltage on the generator and the parallel resistor R_i, while $\phi_{Rext}(t)$ is the voltage on the electric load, here represented by the external resistor with impedance R_{ext}. The combination of relations (6.5) and (6.6) results in the voltage relation for a parallel connection, that is

$$\phi_o(t) - \phi_D(t) = \phi_{Rs}(t) + \phi_C(t) = \phi_{Rext}(t)\,.$$

Recalling that series-connected circuit elements carry the same current, while parallel-connected circuit elements share the same voltage so that the overall current is the sum of the currents on each element, we can describe the circuit by using Kirchhoff's current law

$$i_D(t) = i_{battery}(t) = i_{DEG}(t) + i_{load}(t)\,. \tag{6.7}$$

Experiments on acrylic elastomers [14] have shown that the response of resistors R_i and R_s is ohmic if the electric field in the material will not exceed a threshold value in the range between 20 and 40 MV/m, beyond which the resistance will decrease exponentially. In our simulations we take the voltage ϕ_o supplied by the battery at constant regime as 1 kV and therefore the intensity of the electric field in the generator remains bounded to 20 MV/m. As a consequence, we assume Ohm's laws $i_{_{DEG}}(t) = \phi_{_{Rs}}(t)/R_s$ and $i_{_{Ri}}(t) = \phi_{_C}(t)/R_i$ to complete the formulation.

Therefore, Eq. (6.7) together with Eqs. (6.5) and (6.6) constitute a non-linear differential algebraic system of four equations

$$\begin{cases} \phi_o(t) - \phi_{_D}(t) = \phi_{_{Rs}}(t) + \phi_{_C}(t)\,, \\[2ex] \phi_{_{Rs}}(t) + \phi_{_C}(t) = \phi_{_{Rext}}(t)\,, \\[1ex] I_s \left[\exp\left(\dfrac{\phi_{_D}(t)}{n\, v_T} \right) - 1 \right] = \dfrac{\phi_{_{Rs}}(t)}{R_s} + \dfrac{\phi_{_{Rext}}(t)}{R_{ext}}\,, \\[2ex] \dfrac{\phi_{_{Rs}}(t)}{R_s} = C(\lambda(t))\, \dot{\phi}_{_C}(t) + \dot{C}(\lambda(t))\, \phi_{_C}(t) + \dfrac{\phi_{_C}(t)}{R_i}\,, \end{cases} \tag{6.8}$$

where the voltages $\phi_{_D}(t)$, $\phi_{_{Rs}}(t)$, $\phi_{_C}(t)$ and $\phi_{_{Rext}}(t)$ are the four unknowns. The non-linear system (6.8) can be solved numerically, e.g. by using a DAE solver. Schuster [55] presented the recourse to differential algebraic equation solvers in the analysis of nonlinear electric networks. Regarding the values of resistances in the circuit, on one hand, a review of the literature [23, 32, 42] has led us to set $R_i = 100$ GΩ and $R_s = 70$ kΩ as a reasonable choice. On the other, as we aim at comparing the behaviour of the generator for different end users, we select a quite large range for R_{ext}, namely $R_{ext} \in [0.001, 1000]$ GΩ.

For the description of the characteristic parameters of the diode, we refer to the commercial type designated as NTE517 produced by NTE Electronics Inc. In agreement with [28], we estimate that the saturation current I_s is $\simeq 0.1$ μA and that the thermal voltage v_T is $\simeq 25$ mV at room temperature. In the computations, we will assume a unitary value $n = 1$ for the ideality factor of the diode.

From an electro-mechanical point of view, the soft dielectric generator consists of an incompressible electroactive polymer (EAP) to be modelled by employing the large-strain electro-viscoelasticity, as introduced in Sect. 2.4.

6.2 Calibration of the electro-viscoelastic model

The material taken into consideration is the polyacrylate dielectric elastomer VHB-4910 assumed to show incompressible behaviour, i.e. $J = 1$. Using the energy function (2.25) and the constitutive equations $(2.13)_{1,2}$, we obtain the following expressions

$$\boldsymbol{S} = -p\,\boldsymbol{F}^{-T} + \mu\,\boldsymbol{F} + \sum_{\alpha} \beta_\alpha\,\mu\,\boldsymbol{F}\,\boldsymbol{C}_{v\alpha}^{-1} + \epsilon\,\boldsymbol{F}^{-T}\boldsymbol{E}^0 \otimes \boldsymbol{C}^{-1}\boldsymbol{E}^0\,, \tag{6.9}$$

$$\boldsymbol{D}^0 = \epsilon\,\boldsymbol{C}^{-1}\boldsymbol{E}^0\,, \tag{6.10}$$

for the nominal stress $\boldsymbol{S}$ and for the nominal electric displacement $\boldsymbol{D}^0$. Furthermore, the Mandel-type referential stress tensor defined in Eq. (2.27) is given by

$$\boldsymbol{M}_{v\alpha} = \frac{1}{2}\,\beta_\alpha\,\mu\,\boldsymbol{C}\,\boldsymbol{C}_{v\alpha}^{-1}\,, \tag{6.11}$$

so that the evolution equations (2.29) result in

$$\dot{\boldsymbol{C}}_{v\alpha} = \frac{1}{2}\,\beta_\alpha\,\mu\,\dot{\Gamma}_\alpha \left[\boldsymbol{C} - \frac{1}{3}\,[\boldsymbol{C}\cdot\boldsymbol{C}_{v\alpha}^{-1}]\,\boldsymbol{C}_{v\alpha}\right]. \tag{6.12}$$

The material parameters are identified by separating mechanical and electrical behaviour. Experimental data by Tagarielli et al. [58] is used for the calibration of the electro-viscoelastic model.

6.2.1 Calibration of the mechanical behaviour

The mechanical response of the model is calibrated with experimental data based on a uniaxial tensile loading test. In the absence of electrical effects, i.e. $\boldsymbol{E}^0 = \boldsymbol{0}$, for a uniaxial stress state – where the Cartesian base vectors $\{\boldsymbol{e}_1, \boldsymbol{e}_2, \boldsymbol{e}_3\}$ are assumed to coincide with the principal directions such that $\lambda_1 = \lambda(t)\,,\ \lambda_2 = \lambda_3 = 1/\sqrt{\lambda(t)}$ – the viscoelastic stress in the loading direction can be computed using Eq. (6.9),

$$S = \mu\,\lambda + \sum_{\alpha} \beta_\alpha\,\mu\,\frac{\lambda}{\lambda_{v\alpha}^2} - \sum_{\alpha} \mu\,\frac{\beta_\alpha\,\lambda_{v\alpha} + 1}{\lambda^2}\,, \tag{6.13}$$

cf. [2]. Here $\lambda_{v\alpha}$ are the internal variables formally defined as the square root of the eigenvalues of the respective $\boldsymbol{C}_{v\alpha} = \lambda_{v\alpha}^2\,\boldsymbol{e}_1 \otimes \boldsymbol{e}_1 + \lambda_{v\alpha}^{-1}\,[\boldsymbol{I} - \boldsymbol{e}_1 \otimes \boldsymbol{e}_1]$.

In [58] three different strain rates $\dot{\delta}_m$ are considered, namely $\dot{\delta}_1 = 7 \times 10^{-3}$ s^{-1}, $\dot{\delta}_2 = 1.5 \times 10^{-2}$ s^{-1} and $\dot{\delta}_3 = 3 \times 10^{-2}$ s^{-1}. The strain rate is held constant during the measurements, displacing the cross-head of the testing machine at a variable velocity

$\dot{u}_m$ such that

$$\dot{\delta}_m = \frac{\dot{u}_m}{l} = \frac{\dot{u}_m}{l_0 + u_m(t)} = \text{const}\,, \tag{6.14}$$

where l_0 is the initial length of the sample and where l is the current length. From equation (6.14), the displacement of the cross-head $u_m(t)$ can be computed by solving the ordinary differential equation $\dot{u}_m = \dot{\delta}_m\,[l_0 + u_m(t)]$ under the condition $u_m(0) = 0$, namely

$$u_m(t) = l_0\,[\exp{(\dot{\delta}_m\, t)} - 1]\,.$$

This leads to the stretch ratio

$$\lambda(t) = \frac{l_0 + u_m(t)}{l_0} = \exp{(\dot{\delta}_m\, t)}\,.$$

The response of the model is compared to the experimental data obtained at discrete time points (i, j, k) for the three strain rates $\dot{\delta}_m$. The aim is to find the set of parameters $\{\mu, \beta_\alpha, \dot{\mathit{\Gamma}}_\alpha\}$ by minimising, for all measured data points, the difference between the stress S^{exp} determined experimentally and S^{sim} predicted by the model. In particular, the error to be minimised is computed using the L_2-norm as

$$\text{Error}(\mu, \beta_\alpha, \dot{\mathit{\Gamma}}_\alpha) = \sqrt{\sum_i [\Delta S_i(\dot{\delta}_1)]^2 + \sum_j [\Delta S_j(\dot{\delta}_2)]^2 + \sum_k [\Delta S_k(\dot{\delta}_3)]^2}\,, \tag{6.15}$$

where $\Delta S_i(\dot{\delta}_1)$, $\Delta S_j(\dot{\delta}_2)$ and $\Delta S_k(\dot{\delta}_3)$ denote the differences $[S_i^{exp}(\dot{\delta}_1) - S_i^{sim}(\dot{\delta}_1)]$, $[S_j^{exp}(\dot{\delta}_2) - S_j^{sim}(\dot{\delta}_2)]$ and $[S_k^{exp}(\dot{\delta}_3) - S_k^{sim}(\dot{\delta}_3)]$, respectively.

We use a simplex search method, i.e. the Nelder-Mead algorithm for numerical minimisation (see Appendix A for more details on the minimisation algorithm). Only one Maxwell element is used in the calibration, so that $\alpha = 1$. Indeed, for the experimental data considered, adding more Maxwell elements does not substantially improve the fitting. Fig. 6.3 shows the comparison between simulated and experimental data. The solid lines represent the simulated data, whereas the dots correspond to the experimental data, cf. [58]. The obtained material parameters are shown in Tab. 6.1.

The relaxation time for the Maxwell's rheological element can be computed according to the following relation

$$\tau = \frac{1}{\frac{1}{2}\,\beta\,\mu\,\dot{\mathit{\Gamma}}}\,. \tag{6.16}$$

With the calibrated material parameters, this equation renders τ approximately equal to 45 seconds. For a similar material, namely VHB-F9473PC, a relaxation time comparable with the value resulting from our calibration is found in [46].

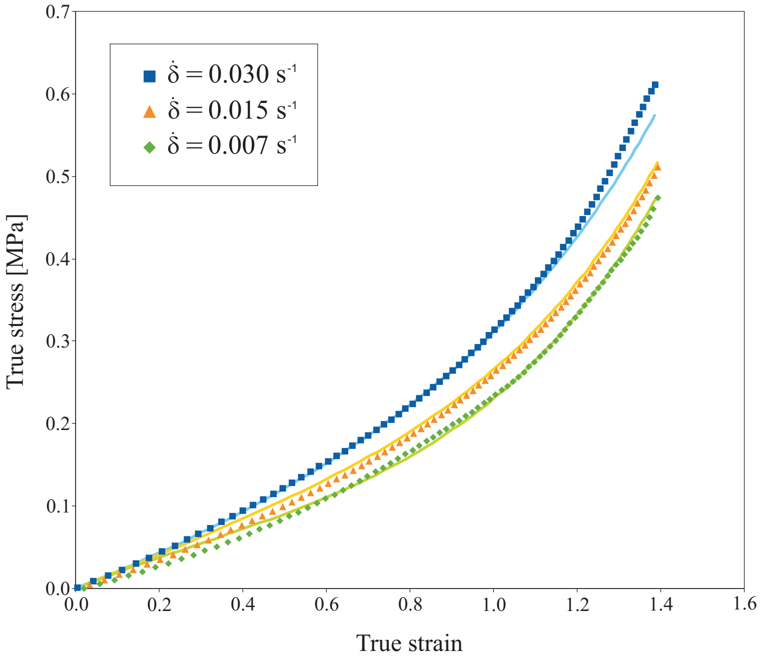

FIGURE 6.3: Viscoelastic behaviour of VHB-4910: stress response at different strain rates as obtained from parameter identification. Dots: experimental data based on experiments by Tagarielli et al. [58]; solid lines: simulated data.

μ [MPa]	β	$\dot{\Gamma}$ [s^{-1} MPa^{-1}]
0.02746	1.46846	1.10174

TABLE 6.1: Mechanical material parameters.

6.2.2 Calibration of the electrical behaviour

In order to calibrate the electrical response of the model and to assess the electrostrictive behaviour of VHB-4910, experimental data is used for the relative dielectric permittivity at different equibiaxial stretches. In [58] two different frequencies $\bar{f}$ are considered, namely 10^{-3} Hz and 200 kHz. The experimental data, see Fig. 6.4, shows that $\epsilon^0_{r,10^{-3}\mathrm{Hz}} = 6.4$ and $\epsilon^0_{r,200\mathrm{kHz}} = 3.8$ and suggests to model the dependency of the relative dielectric permittivity ϵ_r on the mechanical deformation through the first invariant I_1 according to the following relation

$$\epsilon_r(\lambda_1, \lambda_2, \lambda_3) = \frac{A}{\alpha_0 + \alpha_1 \arctan(\alpha_2 + \alpha_3(I_1(\lambda_1, \lambda_2, \lambda_3) - 3))}\,, \tag{6.17}$$

where A, α_0, α_1, α_2, α_3 are dimensionless constant parameters. The response of the model is compared to the experimental data at different stretch levels, with the aim to find the set $\{A, \alpha_0, \alpha_1, \alpha_2, \alpha_3\}$ that minimises the difference. Similarly to the previous case, the error is computed as the L_2-norm and is then minimised by using a simplex search method (for further details see Appendix A). Fig. 6.4 shows the comparison with experimental data. The solid lines represent the prediction of the model, while the dots indicate the measured permittivity, cf. [58]. The obtained material parameters for the relative dielectric permittivity are summarised in Tab. 6.2.

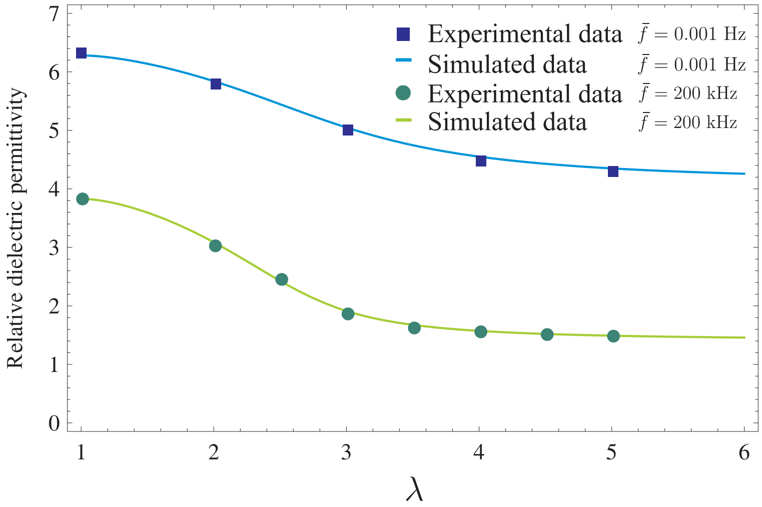

FIGURE 6.4: Dielectric permittivity of VHB-4910 at different equibiaxial stretches for two representative frequencies $\bar{f}$ as obtained from parameter identification based on experiments by Tagarielli et al. [58].

	A	α_0	α_1	α_2	α_3
10^{-3} Hz	4.67636	0.85362	– 0.18891	0.62074	– 0.07079
200 kHz	0.88568	0.37447	– 0.16267	1.20897	– 0.12075

TABLE 6.2: Electrical and coupling material parameters.

The analysis of the DEGs presented in the next Sections will be based on values of the dielectric permittivity which follow the experimental data acquired at a frequency of 10^{-3} Hz.

6.3 Generator operating in the electrical circuit

The performance of a soft viscoelastic dielectric elastomer generator operating in the electrical circuit is analysed. The dielectric elastomer material is acrylic VHB-4910 as presented above. We assume that the initial side length l_0 and thickness h_0 are equal to 100 mm and 1 mm, respectively.

We postulate that the elastomer film is initially prestretched up to a minimum value $\lambda_{min} = \lambda_o - \Lambda$, that is maintained for a sufficiently long time to allow for full relaxation. Therefore, the dielectric elastomer is connected to a source of mechanical work that stretches it periodically up to a maximum value $\lambda_{max} = \lambda_o + \Lambda$ according to the cosinusoidal relation

$$\lambda(t) = -\Lambda \cos(\psi\, t) + \lambda_o, \tag{6.18}$$

where Λ represents the amplitude of the stretch oscillation. In addition, $\psi = 2\,\pi f$ is the angular frequency, f is the frequency of the oscillation and $\lambda_o > 1$ is the mean value of the stretch.

We solve the system of differential algebraic equations given by the electric circuit (6.8), the nominal stress $\boldsymbol{S}(t)$ (6.9) and the evolution equation (6.12) for given loading (6.18) using a DAE-solver. With all relevant quantities at hand, it is possible to determine the energies in order to evaluate the generator performance. The input electrical energy E_{in} is the integral over a cycle of the input power P_{in}, defined as the product of the current through the battery $i_{battery}(t)$ and the voltage ϕ_o of the battery itself

$$E_{in} = \int_{\text{cycle}} P_{in}(t)\,\mathrm{d}t = \int_{\text{cycle}} i_{battery}(t)\,\phi_o\,\mathrm{d}t\,. \tag{6.19}$$

Similarly, we can calculate the total output electrical energy E_{out} as the integral over a cycle of the output power P_{out}, defined as the product of the current through the external resistor $i_{load}(t)$ and its voltage $\phi_{Rext}(t)$

$$E_{out} = \int_{\text{cycle}} P_{out}(t)\,\mathrm{d}t = \int_{\text{cycle}} i_{load}(t)\,\phi_{Rext}(t)\,\mathrm{d}t\,. \tag{6.20}$$

Hence, the electrical energy produced by the generator $\Delta E = E_{out} - E_{in}$ is the difference between the electrical energy input and output. Obviously, if ΔE is positive the generator produces energy in the sense that mechanical energy is converted to electrical energy. If ΔE is negative, the generator dissipates energy, while if it is zero the generator does not convert mechanical to electrical energy.

The same net energy can be attained by subtracting the energy dissipated in the circuit ($\mathcal{D}$) from the amount of energy in the capacitor generated by the dielectric elastomer (E_C), i.e.

$$\Delta E = E_{out} - E_{in} = E_C - \mathcal{D}\,, \tag{6.21}$$

where

$$E_C = \int_{\text{cycle}} P_C(t)\,\mathrm{d}t = \int_{\text{cycle}} i_C(t)\,\phi_C(t)\,\mathrm{d}t\,. \tag{6.22}$$

The energy dissipated throughout the circuit is the sum of the energy dissipated over the diode, and the two resistances R_s and R_i, namely,

$$\mathcal{D} = \mathcal{D}_D + \mathcal{D}_{R_s} + \mathcal{D}_{R_i}\,, \tag{6.23}$$

given by

$$\begin{aligned}\mathcal{D}_D &= \int_{\text{cycle}} P_D(t)\,\mathrm{d}t = \int_{\text{cycle}} i_D(t)\,\phi_D(t)\,\mathrm{d}t\,,\\ \mathcal{D}_{R_s} &= \int_{\text{cycle}} P_{R_s}(t)\,\mathrm{d}t = \int_{\text{cycle}} i_{DEG}(t)\,\phi_{R_s}(t)\,\mathrm{d}t\,,\\ \mathcal{D}_{R_i} &= \int_{\text{cycle}} P_{R_i}(t)\,\mathrm{d}t = \int_{\text{cycle}} i_{R_i}(t)\,\phi_{R_i}(t)\,\mathrm{d}t\,.\end{aligned} \tag{6.24}$$

The mechanical work performed by periodically stretching the dielectric elastomer can be determined as

$$\begin{aligned}W_{mech} &= \int_{\text{cycle}} \Big[S_{11}(t)\,l_0\,h_0\,\dot{X}_1(t) + S_{22}(t)\,l_0\,h_0\,\dot{X}_2(t)\Big]\,\mathrm{d}t\\ &= \int_{\text{cycle}} \Big[S_{11}(t)\,l_0^2\,h_0\,\dot{\lambda}_1(t) + S_{22}(t)\,l_0^2\,h_0\,\dot{\lambda}_2(t)\Big]\,\mathrm{d}t\,.\end{aligned} \tag{6.25}$$

As we have already seen, a measure of the performance of the generator is given by the efficiency η (2.58). In this case, the efficiency is given by ratio of the electrical energy produced by the generator ΔE over the total input energy invested, that is the sum of mechanical work W_{mech} and electrical input energy E_{in}. Eq. (2.58) turns to

$$\eta = \frac{\Delta E}{E_{in} + W_{mech}}\,. \tag{6.26}$$

For different values of the characteristic parameters of the oscillation (λ_o, $\mathit{\Lambda}$) we analyse the performance of the generator by varying the excitation frequency f in the range from 0.1 Hz to 10 Hz, and, as previously mentioned, the resistance of the external resistor R_{ext} in the range from 0.001 GΩ to 1000 GΩ. Regarding the former range, we notice that having disregarded the inertia effects will not affect the outcome of the investigation, as an estimate of the kinetic energy involved in the motion reveals that its maximum value in the more severe case (f=10 Hz, $\lambda_o = 3$, $\mathit{\Lambda} = 0.50$) is only about 5×10^{-3} the amount of change of elastic part of the strain energy in the material along the oscillations.

To calculate the kinetic energy in the DEG we assume a homogeneous deformation in the plate with no superimposed rigid body motion, i.e. the center of mass stays at a fixed point, see Fig. 6.1. This leads us to deformation map components $\varphi_i(\boldsymbol{X}, t) = \lambda_i(t)\,X_i$ with $i = 1, 2, 3$. The kinetic energy is given by $\mathcal{K} = \int_{\mathcal{B}_0} 1/2\,\rho_0\,\dot{\boldsymbol{\varphi}} \cdot \dot{\boldsymbol{\varphi}}\,\mathrm{d}V$ and can be calculated, e.g., for the equibiaxial load case defined as $\lambda_1(t) = \lambda_2(t) = \lambda(t)$ and $\lambda_3(t) = 1/\lambda^2(t)$, see next section, together with equation (6.18). Afterwards, its maximum value, $\max(\mathcal{K})$, is compared with the maximum of the change of the elastic part of the total strain energy, $\max(\int_{\mathcal{B}_0} W_{el}(\lambda(t)) - W_{el}(\lambda_{min})\,\mathrm{d}V)$, during one load cycle.

As the relaxation time is approximately 45 seconds, see Sect. 6.2, the generator efficiency η is computed for one cycle after 200 seconds from the beginning of the stretch oscillation. In this context the viscous effects can be considered to be fully stabilised.

In the analysis, we compare the behaviour of the generator modelled with three constitutive responses:

1. hyperelastic (HYP), with constant dielectric permittivity: the energy corresponds to (2.14) with $\epsilon_r^0 = 6.4$;
2. viscoelastic, with constant dielectric permittivity (VC): the energy refers to (2.25) with $\epsilon_r^0 = 6.4$;
3. viscoelastic, with electrostriction (VE): the energy is determined by (2.25) with deformation-dependent relative dielectric permittivity $\epsilon_r(\lambda_1, \lambda_2, \lambda_3)$, as discussed in Eq. (6.17).

In the following the performance of the generator is evaluated for different loading conditions.

6.4 Equibiaxial loading

We assume that the generator is subjected to equibiaxial loading in the $\boldsymbol{e}_1$- and $\boldsymbol{e}_2$-directions, i.e. $S_{33} = 0$. Imposing the incompressibility constraint, the principal stretches are $\lambda_1(t) = \lambda_2(t) = \lambda(t)$ and $\lambda_3(t) = 1/\lambda^2(t)$ with $\lambda(t)$ given by Eq. (6.18). Hence, the deformation gradient tensor becomes $\boldsymbol{F} = \lambda(t)\,[\boldsymbol{I} - \boldsymbol{e}_3 \otimes \boldsymbol{e}_3] + \lambda^{-2}(t)\,\boldsymbol{e}_3 \otimes \boldsymbol{e}_3$. In this case the capacitance, as defined in Eq. (6.1), takes the following form

$$C = \epsilon\,\frac{l_0^2}{h_0}\,\lambda^4(t) \tag{6.27}$$

and is thus proportional to the fourth power of the stretch.

Bearing in mind that $\boldsymbol{E}^0 = E^0(t)\,\boldsymbol{e}_3$, with $E^0(t) = \phi_C(t)/h_0$, and using expressions (6.9) and (6.10), we can write the nominal electric displacement and the nominal stress in the loading directions as

$$D^0(t) = \epsilon\,\frac{\phi_C(t)}{h_0}\,\lambda^4(t), \tag{6.28}$$

$$S_{11}(t) = S_{22}(t) = \mu\left[\lambda(t) - \frac{1}{\lambda^5(t)}\right] + \beta\,\mu\left[\frac{\lambda(t)}{\lambda_v^2(t)} - \frac{\lambda_v^4(t)}{\lambda^5(t)}\right] - \epsilon\,\frac{\phi_C^2(t)}{h_0^2}\,\lambda^3(t)\,. \tag{6.29}$$

The internal variable $\lambda_v(t)$, with $\boldsymbol{C}_v(t) = \lambda_v^2(t)\,[\boldsymbol{I} - \boldsymbol{e}_3 \otimes \boldsymbol{e}_3] + \lambda_v^{-4}(t)\,\boldsymbol{e}_3 \otimes \boldsymbol{e}_3$, is computed for the case $\alpha = 1$ and by using (6.12) which results in the differential equation

$$\dot{\lambda}_v(t) = 2\,\dot{\varGamma}\,\beta\,\mu\,\lambda_v(t)\left[\frac{\lambda^2(t)}{2\,\lambda_v^2(t)} - \frac{1}{3}\left[\frac{\lambda^2(t)}{\lambda_v^2(t)} + \frac{\lambda_v^2(t)}{2\,\lambda^2(t)}\right]\right] \tag{6.30}$$

with the initial condition $\lambda_v(0) = \lambda_{min}$.

6.4.1 Cycle characterisation of a viscoelastic DEG

The evolution with time of the mechanical and electrical quantities of the generator is best captured by plotting conjugated quantities for one loading cycle, like nominal stress S – stretch λ and voltage $\phi_C + \phi_{R_s}$ – charge Q. These are illustrated in Figs. 6.5 and 6.6 for two different frequencies, i.e. $f = 0.1$ Hz and $f = 1$ Hz, for a viscoelastic material following model VC, assuming a prestretch $\lambda_o = 3.0$, $\varLambda = 0.50$ and $R_{ext} = 0.1$ GΩ.

In Figs. 6.5a and 6.6a cycles starting at different times $t_i = 10, 50, 100$ and 200s are sketched in the $\lambda - S$ diagram. The times t_i are computed relative to the full-charge of the battery occurring at $0.5\,T$. The viscous behaviour causes a perceptible hysteresis with a stabilisation occurring after almost 200 seconds. The downward shifting of the stress is also highlighted by the crossing point in the first depicted cycle in Fig. 6.5a, starting at $t_i = 10$ s. This crossing point results from the fact that, under cyclic loading, the resulting nominal stress S is not periodical at the beginning of the loading until the above mentioned stabilisation occurs. In contrast, the electrical quantities, see Figs. 6.5b and 6.6b, show almost no change over the number of loading cycles.

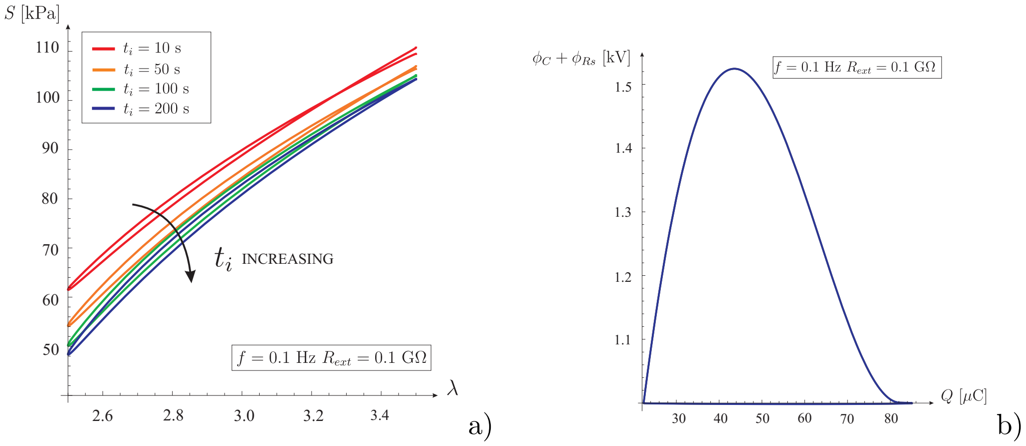

FIGURE 6.5: Plot of loading cycles of a DEG a) in the mechanical S–λ and b) in the electrical $\phi_C + \phi_{R_s}$–Q planes at different initial times t_i, namely 10, 50, 100 and 200 seconds. Model VC, $\lambda_o = 3.0$, $\varLambda = 0.50$, $f = 0.1$ Hz, $R_{ext} = 0.1$ GΩ.

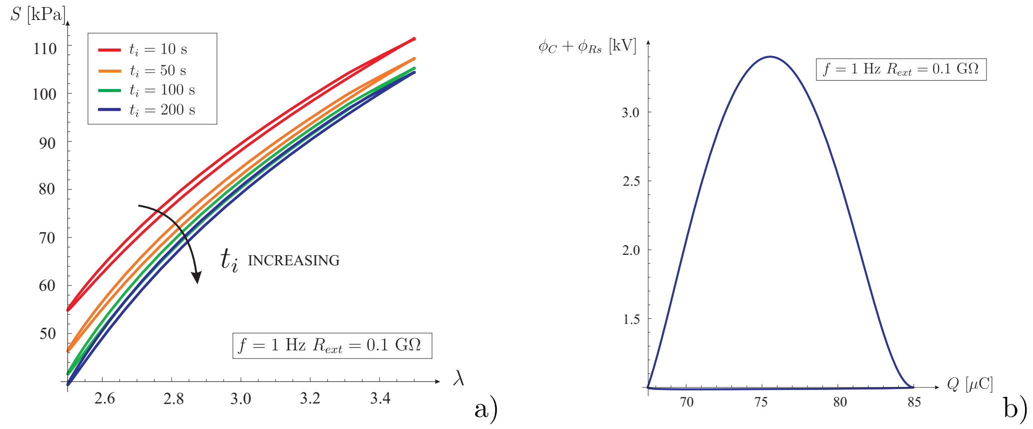

FIGURE 6.6: Plot of loading cycles of a DEG a) in the mechanical S–λ and b) in the electrical $\phi_C + \phi_{R_s}$–Q planes at different initial times t_i, namely 10, 50, 100 and 200 seconds. Model VC, $\lambda_o = 3.0$, $\Lambda = 0.50$, $f = 1$ Hz, $R_{ext} = 0.1$ GΩ.

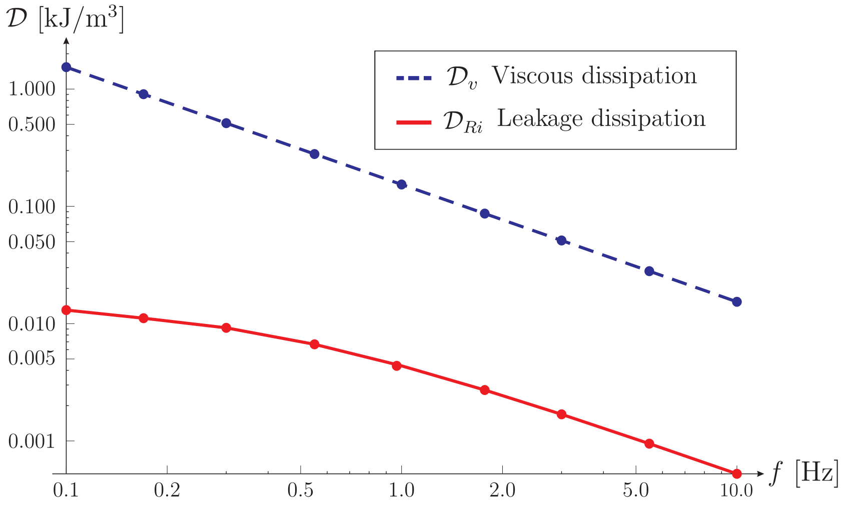

FIGURE 6.7: Plot of the viscous dissipation $\mathcal{D}_v$ and the leakage dissipation $\mathcal{D}_{R_i}$ at different frequencies f. Model VC, $\lambda_o = 3.0$, $\Lambda = 0.50$, $R_{ext} = 0.1$ GΩ.

The analysis of the dissipation in the generator is depicted in Fig. 6.7. We computed during one loading cycle at time $t = 200$ s for different excitation frequencies the specific viscous dissipation $\mathcal{D}_v$ and the dissipation $\mathcal{D}_{R_i}$ due to the leakage current i_{R_i}. Contrary to [19], and due to the low voltage applied to the circuit, we observe that dissipation due to viscosity is always dominant in comparison to the dissipation resulting from the leakage current in the investigated range of frequencies.

In view of the energy performance of the investigated DEGs, Tab. 6.3 summarises the net energy, the mechanical work and the efficiency. All values are computed for one load cycle at $t = 200$ s. We note that the net converted energy turns out to be identical for HYP and VC models as, for both, the electric permittivity is independent of the stretch, even though it is necessary for the viscoelastic DEG to carry out more mechanical work.

Clearly, the VE model predicts a strong reduction in the produced energy due to the decrease of the permittivity with the stretch. More specific comments on the efficiency η are made in section 6.4.2.

$\lambda_o = 3.0$, $\Lambda = 0.5$, $R_{ext} = 0.1$ GΩ				
	f [Hz]	$\Delta E/V_0$ [kJ/m^3]	W_{mech}/V_0 [kJ/m^3]	η
HYP	0.1	1.763	1.792	13.48 %
	1.0	2.456	2.482	55.95 %
VC	0.1	1.763	3.419	11.99 %
	1.0	2.456	2.645	53.94 %
VE	0.1	0.374	2.068	3.01 %
	1.0	1.661	2.032	44.32 %

TABLE 6.3: Energy produced by the generator and mechanical work invested at two different frequencies, $f = 0.1$ Hz and $f = 1$ Hz, computed after 200 s for the three material models considered: $\lambda_o = 3$, $\Lambda = 0.50$, $\epsilon_r^0 = 6.4$, $R_{ext} = 0.1$ GΩ. The reference volume V_0 is given by $l_0^2\, h_0$.

We close this Subsection with a comment on the maximum admissible amplitude of the oscillation Λ. Once an initial prestretch is applied, followed by an in-plane tensile stress imposed in the dielectric elastomer film, a sufficient requirement along the cosinusoidal cycles is that the stress should always remain positive at any time of the loading history in order to avoid any kind of buckling or wrinkling instability. For a hyperelastic formulation, this is achieved by simply controlling that $\lambda > 1$, whereas, for a viscoelastic material, the maximum amplitude Λ_{max} must be computed carefully for the selected material, depending on the mean stretch λ_o, the excitation frequency f and the external resistance R_{ext} characterising the electrical load. For VHB-4910 a numerical estimation is reported in Tab. 6.4 for $R_{ext} = 0.1$ GΩ and $f = 1$ Hz using model VC. At a given λ_o, the corresponding Λ_{max} was obtained by letting the system oscillate until stabilisation of the cycle and then taking the value at which $\min_t\{S_{ii}(t)\} \approx 0$. The values summarised in Tab. 6.4 clearly show the influence of viscoelasticity on the limitation of the admissible oscillation width.

λ_o	1.8	2.0	3.0	4.0
Λ_{max}	0.30	0.38	0.69	0.88

TABLE 6.4: Maximal oscillation amplitude Λ_{max} achievable in an equibiaxial test without inducing in-plane negative stresses. Model VC, $R_{ext} = 0.1$ GΩ, $f = 1$ Hz.

6.4.2 Efficiency analysis

The generator efficiency η, calculated by means of Eq. (6.26) and by using relation (6.25) along with Eq. (6.29), is now investigated in terms of the imposed frequency and the external electrical resistance. Plots of $\eta(f, R_{ext})$ for the three considered constitutive models and $\lambda_o = 3$ are shown in Fig. 6.8. Three amplitudes Λ are analysed in every chart, namely $\Lambda = 0.50$, $\Lambda = 0.25$ and $\Lambda = 0.10$. The frequency is examined up to 10 Hz, even though the maximum operational frequency for DEG devices of the type analysed here is usually in the order of a few Hz.

Firstly, we note that the efficiency η could be either positive or negative depending on the values of the external resistance R_{ext}. Negative values for η are observed for R_{ext} taking values greater than 30 GΩ in the case of small oscillation amplitudes Λ. An evident outcome of the data is that the hyperelastic (HYP) model always predicts higher efficiency in comparison to both viscoelastic models. Moreover, larger amplitudes are always associated with larger efficiency, irrespective of the material model. The reason for this is that the capacitance of the generator depends on the stretch to the power of four which results in considerable increase of the output electrical energy. On the contrary, the energy supplied to the system shows a less than proportional increase in the oscillation amplitude Λ.

Tab. 6.5 shows these energy figures for the three selected amplitudes. In addition, we observe that the difference between the three material models is more pronounced for high values of Λ, as shown in Figs. 6.9a and 6.9b.

$\lambda_o = 3.0$, $f = 1$ Hz, $R_{ext} = 0.1$ GΩ, VC model					
Λ	E_{in}/V_0 [kJ/m^3]	E_{out}/V_0 [kJ/m^3]	$\Delta E/V_0$ [kJ/m^3]	W_{mech}/V_0 [kJ/m^3]	η
0.10	1.067	1.142	0.075	0.085	6.49 %
0.25	1.303	1.771	0.468	0.516	25.74 %
0.50	1.906	4.362	2.465	2.645	53.94 %

TABLE 6.5: Energy produced by the generator and mechanical work invested for the three selected amplitudes $\Lambda = 0.10$, $\Lambda = 0.25$ and $\Lambda = 0.50$, computed after 200 s for the VC model: $\lambda_o = 3$, $f = 1$ Hz, $\epsilon_r^0 = 6.4$, $R_{ext} = 0.1$ GΩ. The reference volume V_0 is given by $l_0^2\, h_0$.

Fig. 6.9a displays the efficiency comparison for the three constitutive models in the case of $\lambda_o = 3$ and $R_{ext} = 1\,$GΩ, as data show that the highest efficiency values lie close to this value, cf. Fig. 6.8. For $\Lambda = 0.5$ the efficiency difference between models HYP and VC is around 15%, while that between HYP and VE is approximately 23%. This difference reduces respectively to 5.3% and 9.5% for $\Lambda = 0.25$, and to 0.6% and 2.4% for $\Lambda = 0.1$. The stretch dependency of the permittivity accounted in model VE reduces η to approximately 8% (2%) with respect to the efficiency of the classical electro-viscoelastic model VC for $\Lambda = 0.5$ ($\Lambda = 0.1$).

The same comparison for $\lambda_o = 3$ and $f = 1$ Hz in terms of the external resistance R_{ext} is depicted in Fig. 6.9.b. As already observed, η is negative for high values of the

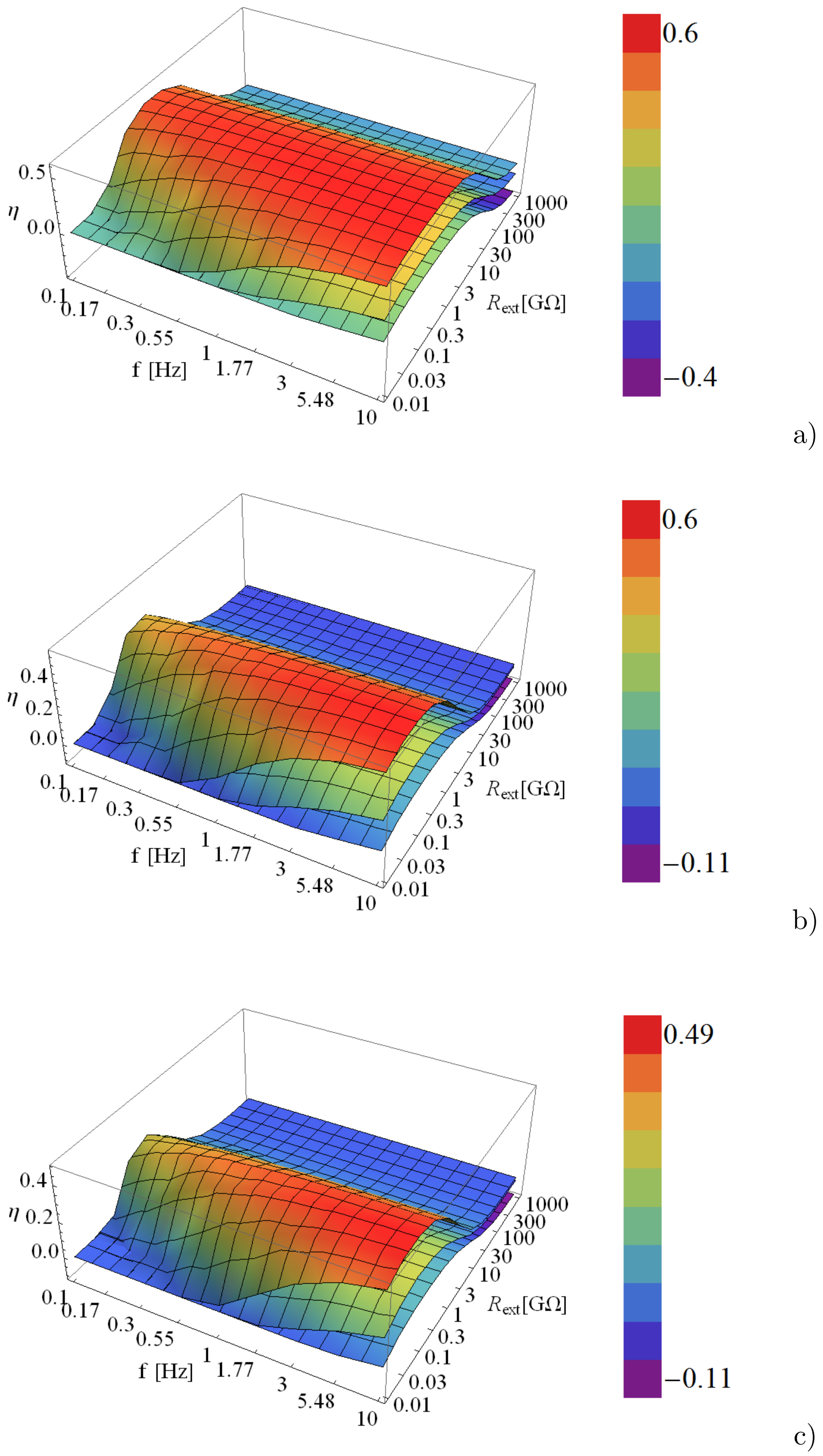

FIGURE 6.8: Plot of the efficiency $\eta(R_{ext}, f)$ for the three different material models: a) hyperelastic, HYP, b) viscoelastic, VC, and c) electrostrictive viscoelastic, VE. Equi-biaxial loading conditions with $\lambda_o = 3.0$; $\varLambda = 0.50$, $\varLambda = 0.25$ and $\varLambda = 0.10$.

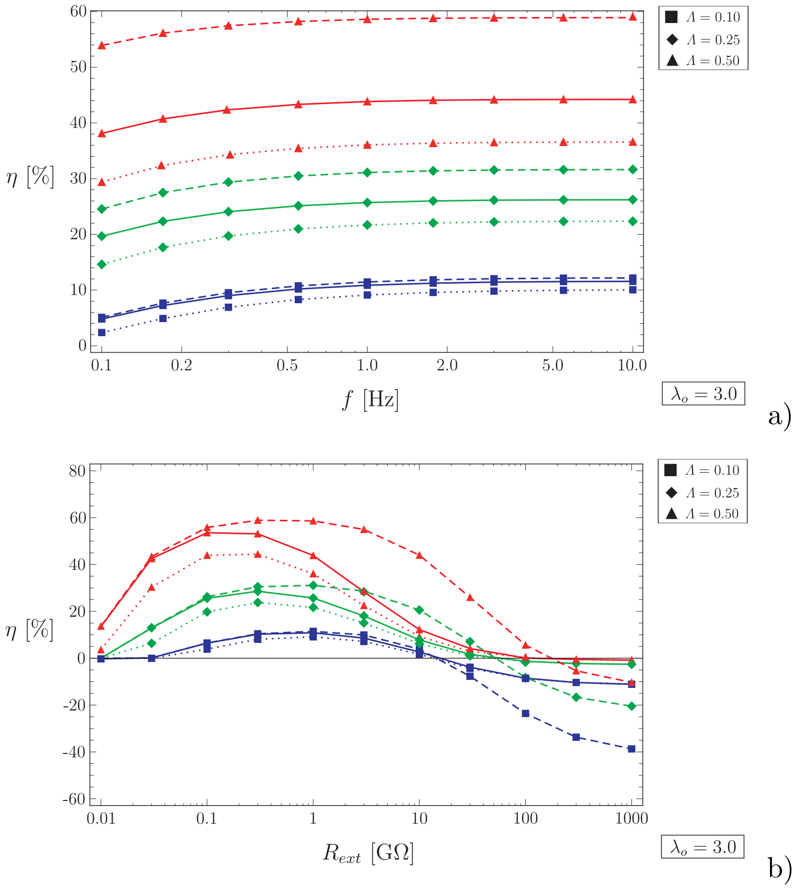

FIGURE 6.9: Plot of the efficiency η versus a) frequency f at $R_{ext} = 1$ GΩ, and b) external resistance R_{ext} at $f = 1$ Hz. Equi-biaxial loading conditions with $\lambda_o = 3.0$; $\Lambda = 0.50,\ 0.25,\ 0.10$. Dashed, continuous and dotted lines are referred respectively to HYP, VC and VE models.

external resistance R_{ext}, depending on the value of the oscillation amplitude Λ, in the range between 30 and 300 GΩ (increasing values for increasing Λ's).

In these cases, the output electrical energy is lower than the input one. An explanation is that the voltage of the connected battery, ϕ_o=1 kV, is not sufficient to power the mechanical energy conversion. As a result, the charge exchanged by the generator at every cycle is relatively low and inadequate to feed the external resistor. For a battery operating at a higher voltage, the threshold value of R_{ext}, beyond which $\eta < 0$, increases accordingly.

Among the three models, hyperelasticity predicts a wider range where the efficiency is positive. For small values of R_{ext}, the VC model behaves similarly to the hyperelastic one up to a peak value, which occurs at lower values of the external resistance R_{ext} increasing the amplitude Λ. Moreover, it is noted that, for the model with electrostriction (VE), the values of the efficiency are always lower in comparison to the hyperelastic model within the whole considered range of R_{ext}.

The influence of the mean stretch λ_o on the efficiency in terms of the external frequency f is outlined in Fig. 6.10 for $R_{ext} = 1$ GΩ and for a generator based on the viscoelastic (VC) constitutive assumption. When λ_o is equal to 1.8 the behaviour of the generator is noticeably different between frequencies lower and higher than 1 Hz: the change in η through the frequency range is approximately 19% for $\mathit{\Lambda} = 0.1$ raising to 33% for $\mathit{\Lambda} = 0.25$. On the contrary, for a higher mean stretch ($\lambda_o = 3$), the behaviour of the generator is more stable, the efficiency variation is up to 6% for the considered values of the amplitude. Hence, for a viscoelastic DEG, when the average value of the oscillation λ_o increases, the behaviour of the generator becomes more stable and less dependent on the other electrical and mechanical parameters.

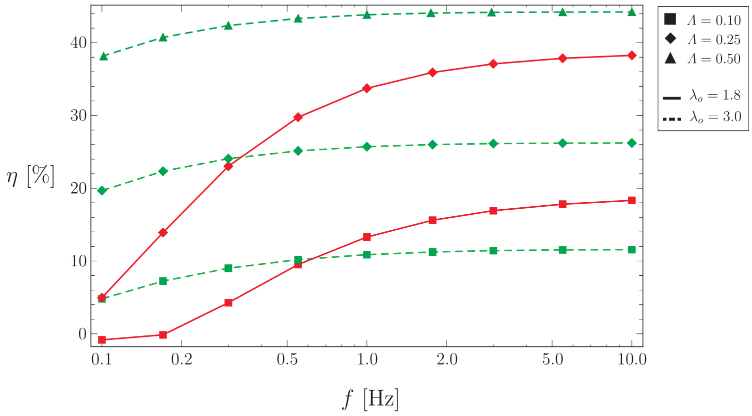

FIGURE 6.10: Plot of the efficiency η versus frequency f for two values of the mean value of the oscillation stretch $\lambda_o = 1.8$ and $\lambda_o = 3$. Equi-biaxial loading conditions with $R_{ext} = 1$ GΩ, VC model.

6.4.3 Failure envelope at regime conditions

At regime conditions, the in-plane viscous stretches tend to the mean stretch λ_o, namely

$$t \to \infty \qquad \lambda_v(t) \to \lambda_o.$$

Precisely, the in-plane viscous stretches experience a small oscillation around a value approximately equal to $98\%\lambda_o$. Hence, we can assume as the most severe case that, at regime, the principal viscous stretches $\{\lambda_{v1}(t), \lambda_{v2}(t), \lambda_{v3}(t)\}$ are equal to $\{\lambda_o, \lambda_o, 1/\lambda_o^2\}$. Under this assumption, for an ideal dielectric (i.e. $\boldsymbol{D} = \epsilon \boldsymbol{E}$), we can obtain the expression of the failure curves for the generator in terms of the dimensionless variables (2.17) adopting the model VC. In the following, we employ the same procedure illustrated in Subsect. 2.6.2 for the ideal hyperelastic DEG under equibiaxial loading conditions (i.e. HYP model).

In the electrical plane, the curves relative to the **stretches limiting the oscillation**, i.e. $\lambda_{min} = \lambda_o - \mathit{\Lambda}$ and $\lambda_{max} = \lambda_o + \mathit{\Lambda}$, are simply prescribed by the following equations

$$\bar{\phi} = \frac{\bar{\omega}_0}{\lambda_{min}^4}, \qquad \bar{\phi} = \frac{\bar{\omega}_o}{\lambda_{max}^4}. \tag{6.31}$$

Analogously, in the electrical plane, the curve related to the **mean value of the stretch oscillation** is characterised by this expression

$$\bar{\phi} = \frac{\bar{\omega}_0}{\lambda_o^4}. \tag{6.32}$$

The **electric breakdown** failure is outlined by two curves, which surround the region of admissible states in the mechanical and in the electric planes, respectively prescribed as

$$\bar{S} = \lambda\left(1 + \beta\frac{1}{\lambda_o^2}\right) - \frac{4}{\lambda^5}(1 + \beta\lambda_o^4) - \frac{\bar{E}_{eb}^2}{\lambda}, \qquad \bar{\phi} = \frac{\bar{E}_{eb}^2}{\bar{\omega}_o}, \tag{6.33}$$

where $\bar{E}_{eb}$ is the dimensionless breakdown strength (2.33). The electric breakdown strength of VHB-4910 is assumed to be 100 MV/m, hence its dimensionless value is $\bar{E}_{eb} = 4.54\,$.

The **loss of the tensile state** ($S = 0$), in the electric plane, is characterised by the expression

$$\bar{\phi} = \frac{\bar{\omega}_0}{\left[\frac{\bar{\omega}_0^2 + 1 + \beta\lambda_o^4}{1 + \beta\frac{1}{\lambda_o^2}}\right]^{2/3}}. \tag{6.34}$$

Finally, the curves corresponding to the **electromechanical instability** in the two thermodynamic planes are

$$\bar{S} = \frac{2}{3}\left[\lambda(1 + \beta\lambda_o^2) - \frac{4}{\lambda^5}(1 + \beta\lambda_o^4)\right], \quad \bar{\phi} = \frac{\bar{\omega}_0}{\left[\frac{3\bar{\omega}_0^2 - 5(1 + \beta\lambda_o^4)}{1 + \beta\frac{1}{\lambda_o^2}}\right]^{2/3}}. \tag{6.35}$$

In Figs. 6.11a, 6.11b and 6.11c are depicted the failure curves relative to VC model for three different values of the mean stretch, namely $\lambda_o = 1.8, 3, 4$. In the same figures, the dashed lines represent the failure curves referred to HYP model (see Subsect. 2.6.2). Comparing the failure curves obtained by employing HYP and VC models, it is evident that the limit stretches and the electric breakdown curves are not modified by viscous effects, whereas the electromechanical instability and the loss of tensile stress state

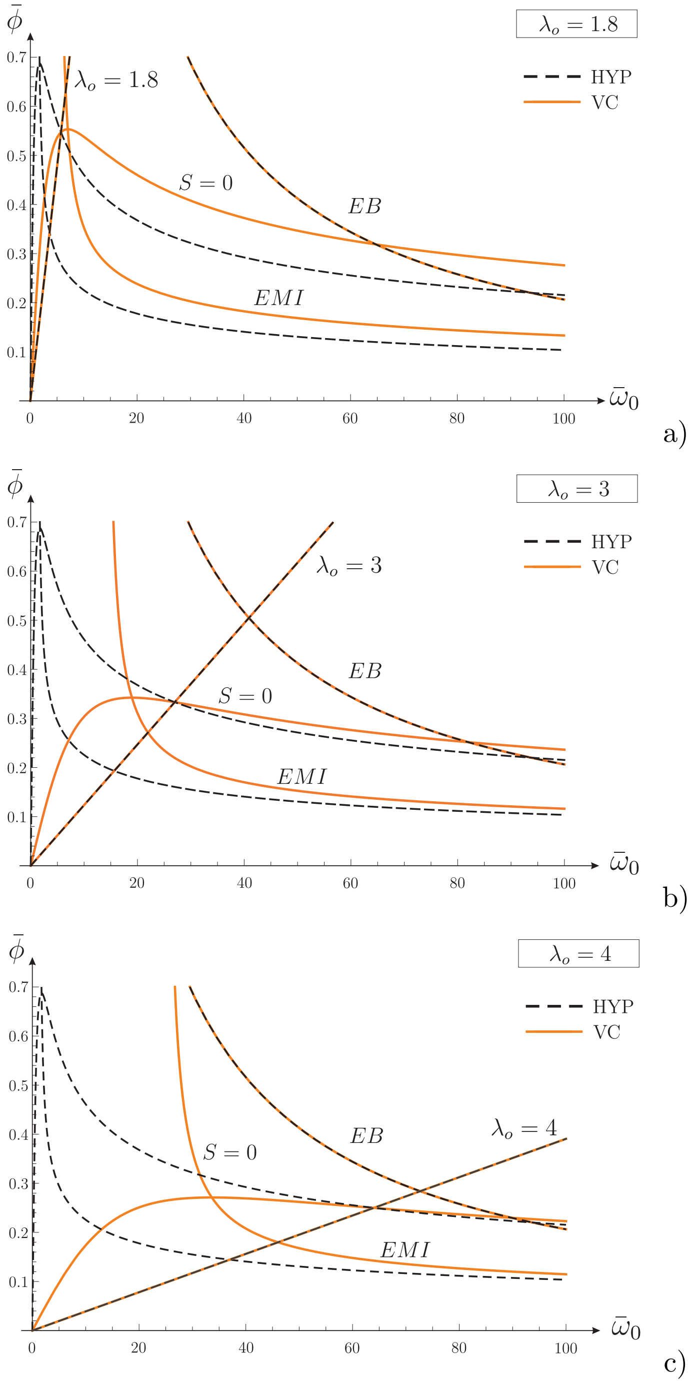

FIGURE 6.11: Plot on the electrical $\bar{\phi}$–$\bar{\omega}_0$ plane of the failure envelope for different values of the mean stretch λ_o. Solid lines are referred to the VC model, dashed lines to the HYP model.

curves are strongly modified when the viscosity of the polymer is taken into account in the analysis.

When the mean stretch λ_o increases, the admissible state region not only becomes smaller but also changes shape, as can be deduced from Fig. 6.11. Furthermore, the failure curves

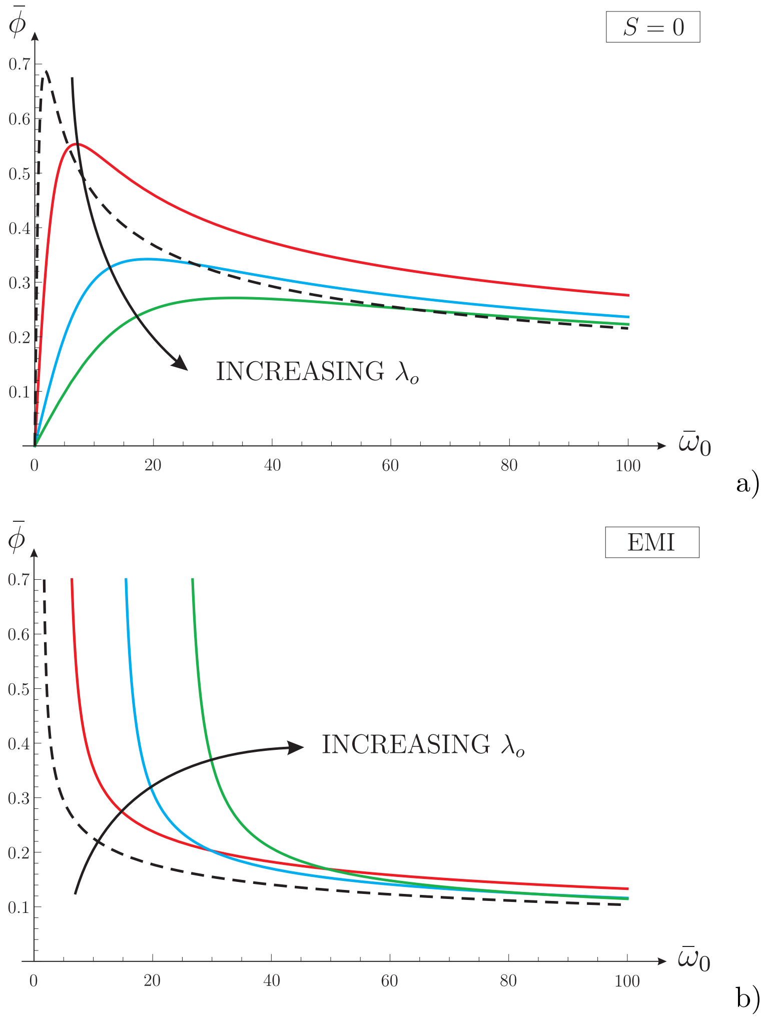

FIGURE 6.12: Plot on the electrical $\bar{\phi}$–$\bar{\omega}_0$ plane of the a) loss of tensile state and b) electromechanical instability curves for different values of the mean stretch, namely $\lambda_o = 1.8, 3, 4$. Solid lines are referred to the VC model, dashed lines to the HYP model.

relative to loss of tension and electromechanical instability differ increasingly from the hyperelastic case. The peak of the loss of tensile state curve occurs for lower value of the voltage $\bar{\phi}$ and higher value of the charge density $\bar{\omega}_0$, as shown in Fig. 6.12a. As a consequence, the electromechanical instability curve is shifted right-hand side, as depicted in Fig. 6.12b.

As a result of the modification of the generator admissible state region, the natural configuration (i.e. $\lambda = 1$) is a not-allowed state for VC model. Thus, there is an upper bound on the maximal amplitude of the stretch oscillation Λ_{max}, as anticipated in Subsect. 6.4.1. This value depends on the frequency f of the mechanical excitation and on the external resistance value R_{ext}.

Varying the external resistance of the circuit at fixed frequency (or vice versa changing the frequency of the excitation at fixed external resistance) in such a way that the product of the two is held constant, we obtain the same cycle on the electrical plane, see Fig. 6.13. Thus, the cycle is uniquely identified for a given value of the product of the mechanical excitation frequency f and the external resistance R_{ext}.

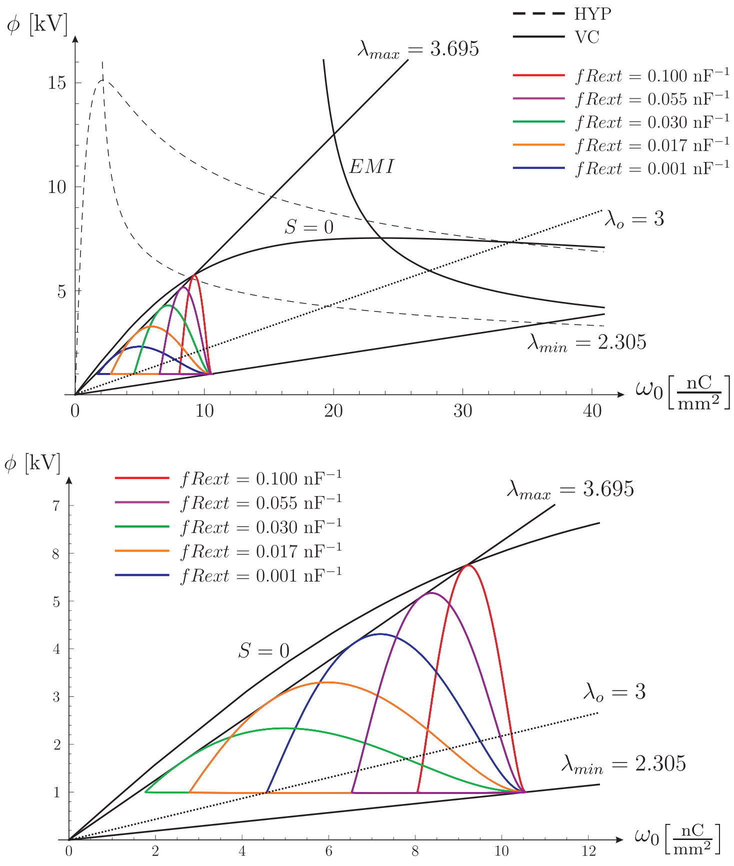

FIGURE 6.13: Plot of the cycle on the electrical plane for different values of the product fR_{ext}, at $\lambda_o = 3$ and $\Lambda = 0.695$. The failure curves are represented by dashed black lines for the HYP model and by solid black lines for the VC model.

This product is in fact equal to the ratio of the maximum voltage and the maximal current over the external resistor

$$fR_{ext} = \frac{\max(\phi_{Rext}(t))}{\max(i_{load}(t))}. \tag{6.36}$$

From a dimensional analysis of Eq. (6.36), it can be found that the product fR_{ext} is the inverse of a capacitance. This means that the external resistance is equal to the capacitative reactance of an equivalent capacitor whose working frequency is equal to that of the mechanical excitation

$$R_{ext} = \frac{1}{2\pi f C^{\circ}}. \tag{6.37}$$

Inverting Eq. (6.37) we can easily obtain the capacitance of the capacitor equivalent to the external resistor as $C^\circ = 1/(2\pi f R_{ext})$. Finally, multiplying Eq. (6.37) by the frequency f, we can derive that the product of the stretch oscillation frequency and the external resistance is actually equal to the inverse of the equivalent capacitance

$$f R_{ext} = \frac{1}{2\pi C^\circ}. \tag{6.38}$$

In the light of this fact, we can determine the maximal amplitude of the stretch oscillation as a function of the product $f R_{ext}$. In Fig. 6.14 the values of the maximal amplitude Λ_{max} for a mean stretch $\lambda_o = 3$ as a function of the product $f R_{ext}$ are reported.

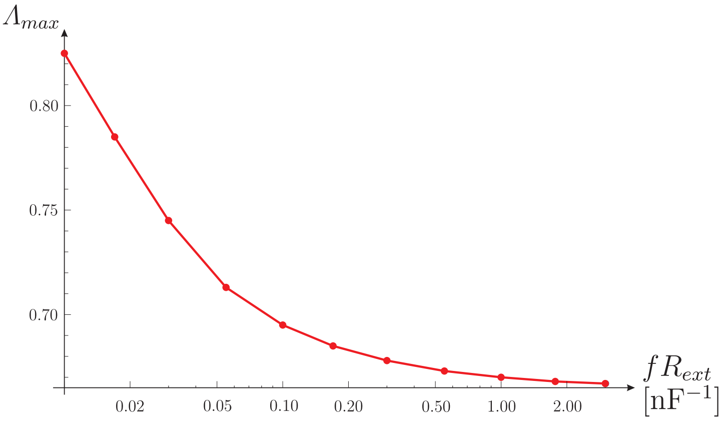

FIGURE 6.14: Plot of the maximal oscillation amplitude Λ_{max} as a function of the product $f R_{ext}$ for $\lambda_o = 3$.

6.5 Uniaxial loading

The soft dielectric elastomer here is subjected to uniaxial loading conditions in the direction $\boldsymbol{e}_1$ so that $S_{22} = S_{33} = 0$. Imposing the incompressibility constraint, the principal stretches are $\lambda_1(t) = \lambda(t)$ and $\lambda_2(t) = \lambda_3(t) = 1/\sqrt{\lambda(t)}$. Hence, the deformation gradient tensor becomes $\boldsymbol{F} = \lambda(t)\, \boldsymbol{e}_1 \otimes \boldsymbol{e}_1 + 1/\sqrt{\lambda(t)}\, [\boldsymbol{I} - \boldsymbol{e}_1 \otimes \boldsymbol{e}_1]$. Compared with the equibiaxial case, the capacitance is lower as it shows only a direct proportionality to the axial stretch, i.e.

$$C = \epsilon \, \frac{l_0^2}{h_0} \, \lambda(t) \, . \tag{6.39}$$

Bearing in mind that $\boldsymbol{E}^0 = E^0(t)\, \boldsymbol{e}_3$, with $E^0(t) = \phi_C(t)/h_0$, we can write the nominal electric displacement and the nominal stress in the loading direction as

$$D^0(t) = \epsilon \, \frac{\phi_C(t)}{h_0} \, \lambda(t) \, , \tag{6.40}$$

while the relation between stress, stretch and voltage turns out to be

$$S_{11}(t) = \mu \left[\lambda(t) - \frac{1}{\lambda(t)^2} \right] + \beta\, \mu \left[\frac{\lambda(t)}{\lambda_v(t)^2} - \frac{\lambda_v(t)}{\lambda(t)^2} \right] - \epsilon\, \frac{\phi_C(t)^2}{h_0^2} \,. \tag{6.41}$$

The internal variable $\lambda_v(t)$ is computed by integrating the evolution equation (6.12) which, in the incompressible uniaxial case, reduces to

$$\dot{\lambda}_v(t) = \frac{1}{4}\, \dot{\Gamma}\, \beta\, \mu\, \lambda_v(t) \left[\frac{\lambda(t)^2}{\lambda_v(t)^2} - \frac{1}{3} \left[\frac{\lambda(t)^2}{\lambda_v(t)^2} + 2\, \frac{\lambda_v(t)}{\lambda(t)} \right] \right] , \tag{6.42}$$

with the initial condition $\lambda_v(0) = \lambda_{min}$.

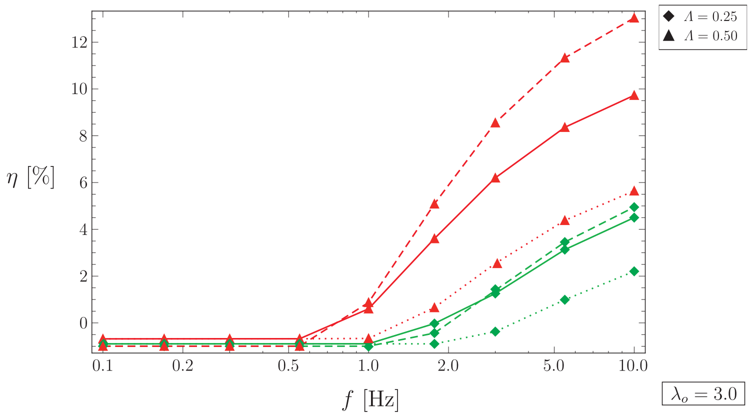

FIGURE 6.15: Plot of the efficiency $\eta(R_{ext}, f)$ for an external resistance R_{ext} =1 GΩ and $\lambda_o = 3.0$, $\Lambda = 0.50$ and $\Lambda = 0.25$. Dashed, continuous and dotted lines are referred respectively to HYP, VC and VE models.

Three-dimensional plots of the efficiency, i.e. graphical representations of the function $\eta(f, R_{ext})$, are not given here for conciseness. But it is found that at the same supplied voltage ϕ_o and compared with the equibiaxial loading, the uniaxial excitation leads to overall lower values of the efficiency. Additionally, the range of points (f, R_{ext}) with positive efficiency is more limited. As in the case of equibiaxial loading, the HYP constitutive model always predicts higher values of the efficiency with respect to the two kinds of viscoelasticities. However, in this uniaxial loading case, the efficiency of the generator is greater than zero only for few values of the variables f and R_{ext}. When the amplitude of the oscillation Λ is small, i.e. $\Lambda = 0.10$, the efficiency is always lower or equal to zero, i.e. $\eta \leq 0$, even in the case of hyperelasticity.

Fig. 6.15, obtained for $\lambda_o = 3$ and $R_{ext} = 1\text{G}\Omega$ with $\Lambda = 0.25$ and $\Lambda = 0.50$, shows negative values of efficiency at low frequencies. As in the case of equibiaxial loading, the efficiency computed with the HYP model is greater than the predicted by VC and VE models. The difference between the three different models decreases for decreasing values of the oscillation amplitude $\varLambda$. For $\varLambda = 0.5$, the difference in efficiency between HYP and VC models is approximately 1.3%, while the difference between HYP and VE models is approx. 3.1%. For $\varLambda = 0.25$ we obtained 0.2% and 0.9%, respectively. As mentioned before, the analysis clearly demonstrates that, by applying the same oscillation conditions $\varLambda$ and λ_o the uniaxial loaded generator shows a considerably lower efficiency than the equibiaxially loaded generator.

To relate the two loading conditions we investigate the DEG performance when the capacitance changes during a cycle are equal. As a reference, we choose the hyperelastic (HYP) model under equibiaxial loading with $\lambda_o = 1.8$ and $\varLambda = 0.1$. An equal capacitance change is observed in a DEG subjected to the uniaxial loading for $\lambda_o = 10.621$ and $\varLambda = 2.34$. The computed efficiency with $R_{ext} = 1$ GΩ and $f = 1$ Hz are $\eta = 15.16\%$ for equibiaxial and $\eta = 13.04\%$ for uniaxial loading.

Chapter 7

Conclusions

The performance optimisation of Dielectric Elastomer Generators has been investigated in the framework of the nonlinear electro-elasticity.

The analysed load-driven DEG is made up of a dielectric film coated with compliant electrodes at both sides, undergoing a Carnot-type electromechanical cycle formed by a sequence of four strokes, during which charge and load are alternately held constant. Overall, a net amount of electric energy is released over a single cycle.

In the first part of this work, two in-plane loading mode have been considered, namely plane-strain and equibiaxial. In order to identify the best cycle out of which maximum energy can be harvested, a constraint optimisation problem has been formulated accounting for possible failure modes of the DEG, namely electric breakdown, mechanical rupture due to over-stretching of the polymeric film, buckling-like instabilities due to loss of tension and electromechanical instability.

First of all, the threshold for the dielectric strength of the material, stating the limit of the electric breakdown influence on the definition of the allowable state region for the generator, has been identified. This dielectric strength threshold detects the maximal energy theoretically extractable by the generator.

Within the framework of conservative electro-elasticity, a numerical constraint optimisation procedure has been employed to determine the optimal cycle that resides within the failure envelop. Both the total amount of harvested energy per unit volume and the efficiency of the DEG were optimised. Particular attention has been paid to the influence of the electric breakdown on the optimal cycle failure.

The performance of a DEG crucially depends on the stretchability of the elastic dielectric. This is due to the fact that the mechanical work produced by the external force can be larger if the film can reach large reversible stretch ratios.

The main outcome of the optimisation process is a universal curve, relating the attainable stretch ratio and the dielectric strength of the material. Clearly, the larger the dielectric strength of materials, the more energy can be harvested from the DEG. However, if the dielectric strength of the film is larger than the threshold limit represented by this curve, the maximal electric field that develops during the optimal cycle does not reach the electric breakdown of the material. This implies that if the pair dielectric strength–ultimate stretch ratio of the film corresponds to a point above the universal curve, the maximal harvested energy is independent of the dielectric strength of the film. In other words, once the ultimate stretch ratio of the film is given, the maximal extractable energy is bounded by the universal curve regardless of the material electric breakdown limit. The universal curve may also serve as a design criterion for DE-based generators.

Besides these in-plane configurations, the performance of a DEG composed of an annular membrane deformed out-of-plane by an external oscillating loading has been investigated employing a hyper-electro-elastic model. Also in this case, the performance quantities, that is efficiency and amount of gained energy per unit mass, have been extensively analysed for several configurations. The main findings can be summarised as follows:

- an optimal initial prestretch of the membrane exists for which the energy conversion is more favourable: its value depends on the external-to-inner radius ratio and it is not larger than 25-30% of the initial length/width. This is a very important design indication as typical imposed prestretches for acrylic films in DE devices are usually on the order of 300–400%;
- for an acrylic elastomer generator, a radius ratio close to one determines the ideal configuration to maximise the amount of energy per unit mass. Differently, efficiency of the energy conversion process reaches the top for radius ratios in the range 2÷2.5;
- similarly, at the optimal prestretch, the efficiency is maximised for maximum loads of about one half of the highest possible F_{max}, while the gained energy is rather proportional to the applied load.

The last two items show that a design based on maximisation of energy may lead to a quite different device with respect to the outcome of an efficiency-guided design. Hence it is important to find the best compromise between the harvested energy and the efficiency.

Soft materials usually employed in dielectric elastomer generators show a remarkable viscoelastic behaviour and may display a deformation-dependent permittivity, a phenomenon known as electrostriction. Therefore, the design and the analysis of soft energy harvesters, which undergo a high number of electromechanical cycles at frequencies in the range of one Hertz, must be based on reliable models that include such behaviour. In the final part of this work, removing the conservative hypothesis, a large strain electro-viscoelastic model for a polyacrilate elastomer, VHB-4910 produced by 3M, has been proposed and calibrated on the basis of experimental data available in the literature.

The model has been used to simulate the performance of a soft prestretched dielectric elastomer generator operating in a circuit where a battery at constant voltage supplies the required charge at each cycle and where an electric load consumes the produced energy. Two periodic in-plane loading conditions, namely homogeneous states under equi-biaxial and uniaxial deformation, are considered for the soft capacitor.

The application of the proposed model has provided, for the generator, *i*) the assessment of viscous and electrostrictive effects on the efficiency and on the net energy gained after each cycle and *ii*) the evaluation of energy losses in all dissipative sources of the device, as a function of the imposed mechanical frequency and of the electrical load characterising the circuit.

The main result of this analysis is that, compared with a hyperelastic model, the efficiency is reduced by viscoelasticity for high values of the mean stretch and of the amplitude of stretch oscillation. The reduction is almost insensitive of the mechanical frequency, whereas the efficiency is further reduced by possible electrostrictive properties of the material. We observed a range of values of the external electric load with a maximal efficiency. Furthermore, at low applied voltage, the viscous dissipation of the material dominates the energy loss stemming from the leakage current across the filled soft capacitor.

Appendix A

Non-linear optimisation: Nelder-Mead method

The Nelder-Mead algorithm is a simplex search method, belonging to the general class of direct search methods. This technique was proposed by John Nelder and Roger Mead in 1965 [47]. The algorithm is designed for multidimensional optimization without derivatives, for this reason it is suitable for problem with non-smooth functions, uncertain function values or discontinuous functions.

The method solves the problem of minimizing a given non-linear function $f : \mathbb{R}^n \to \mathbb{R}$ using only function values at some point in $\mathbb{R}^n$, without attempting to compute an approximate gradient at any of these points.

A simplex $\mathcal{S}$ in $\mathbb{R}^n$ is defined as the convex hull of $n + 1$ vertices $x_0, ..., x_n \in \mathbb{R}^n$, e.g., in $\mathbb{R}^2$ $\mathcal{S}$ is a triangle and in $\mathbb{R}^3$ is a tetrahedron. The Nelder-Mead algorithm begins with a set of $n+1$ points $x_0, ..., x_n \in \mathbb{R}^n$, constituting the vertices of the working simplex $\mathcal{S}$, and the corresponding set of function values at the vertices $f_j = f(x_j)$ for $j = 0, ..., n$. The initial working simplex $\mathcal{S}$ has to be non-degenerate, i.e., the initial points $x_0, ..., x_n$ must not lie on the same hyperplane. The method then perform a sequence of transformation of the working simplex $\mathcal{S}$ with the aim of decrease the function values at its vertices. At each step, the transformation is determined by computing one or more test points and comparing their corresponding function values with those at the vertices of the simplex $\mathcal{S}$. The process terminates when the working simplex $\mathcal{S}$ becomes sufficiently small , or when the function values f_j are close enough.

The method could be implemented in many different ways, depending on the procedure for the construction of the initial simplex and on the selection of the convergence or termination test used to end the iterative process.

Despite these differences, the general algorithm is the following:

1. construct the initial working simplex $\mathcal{S}$;
2. iteration until convergence:
    - *ordering*: determine the indices h, s, l of the worst, second worst and the best vertex, respectively, in the current working simplex $\mathcal{S}$, e.g., $f_h = max_j\, f_j$, $f_s = max_{j \neq h}\, f_j$, $f_l = min_{j \neq h}\, f_j$;
    - *centroid computation*: compute the centroid c of the best side, i.e. the one opposite to the worst vertex x_h;
    - *transformation*: construct a new working simplex from the current one. First of all, try to substitute the worst vertex with a better point using reflection, expansion or contraction with respect to the best side. Else shrink the simplex towards the best vertex x_l, computing new n points.
3. return the best vertex of the current simplex $\mathcal{S}$ and the associated function value.

The initial simplex $\mathcal{S}$ is usually constructed by generating $n+1$ vertices $x_0, ..., x_n$ around a given input point $x_{in} \in \mathbb{R}^n$. In practice, the usual choice is $x_0 = x_{in}$ to allow suitable restarts of the algorithm. The remaining n vertices are determined generating one of the two standard shapes of the simplex $\mathcal{S}$.

The simplex transformation is ruled by four parameters (α, β, γ, δ), controlling, respectively, reflection, contraction, expansion and shrinkage.

The transformation parameters must fulfil the following constraints:

$$\alpha > 0 \qquad 0 < \beta < 1 \qquad \gamma > 1 \qquad \gamma > \alpha \qquad 0 < \delta < 1,$$

standard values, used in many implementation, are $\alpha = 1$, $\beta = 1/2$, $\gamma = 2$ and $\delta = 1/2$.

The algorithm accomplishes the following steps for the transformation of the simplex:

1. **reflection**: compute the reflection point $x_r = c + \alpha(c - x_r)$ and $f_r = f(x_r)$, if $f_l \leq f_r \leq f_s$ the point is accepted and the iteration stop;
2. **expansion**: if $f_r < f_l$, compute the expansion point $x_e = c + \gamma(x_r - c)$ and $f_e = f(x_e)$. If $f_e \leq f_r$ the point x_e is accepted and the iteration finishes, else the point x_r is accepted and the iteration follows;
3. **contraction**: if $f_e \geq f_r$, compute the contraction point x_c using the better point between x_h and x_r

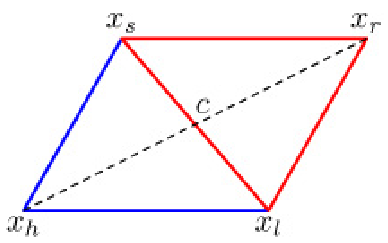

FIGURE A.1: Nelder-Mead method: reflection of the simplex.

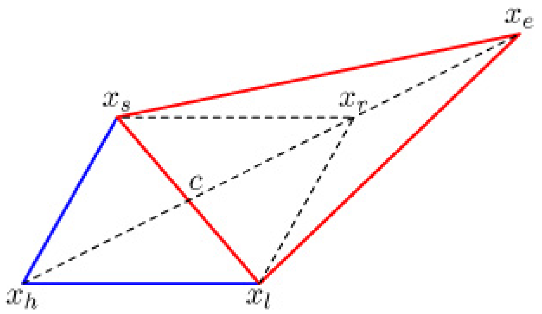

FIGURE A.2: Nelder-Mead method: expansion of the simplex.

- ***outside***:

  if $f_s \leq f_r < f_h$ compute $x_c = c + \beta(x_r c)$ and $f_c = f(x_c)$, if $f_c \leq f_r$, accept x_c and terminate the iteration.

- ***inside***:

  if $f_r \leq f_h$ compute $x_c = c + \beta(x_h c)$ and $f_c = f(x_c)$, if $f_c < f_h$, accept x_c and terminate the iteration.

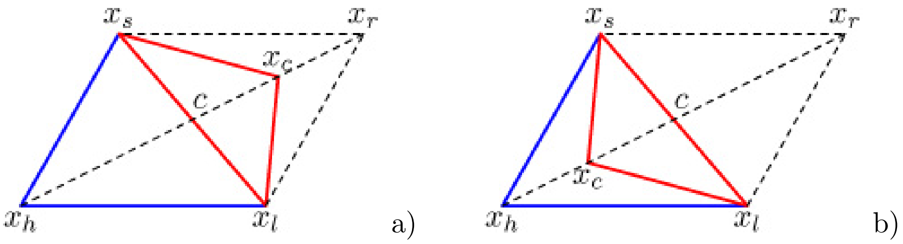

FIGURE A.3: Nelder-Mead method: contraction of the simplex a) outside and b) inside.

4. **shrinkage**: compute n new vertices $x_j = x_l + (x_j x_l)$ and $f_j = f(x_j)$ for $j = 0, ..., n$, with $j \neq l$, generating the new simplex.

In order to ensure the termination of the iterative process in a finite amount of time, the implementation of the Nelder-Mead algorithm must include a termination test. Usually the termination test is composed of three different part:

1. *a domain convergence test*, satisfied when the simplex is small enough;

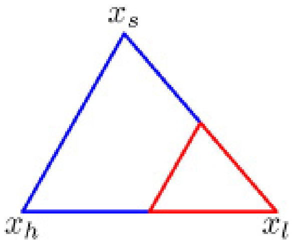

FIGURE A.4: Nelder-Mead method: shrinkage of the simplex.

2. *a function-value convergence test*, satisfied when the function values are close enough;

3. *a no-convergence test*, satisfied when the number of iteration exceeds the maximum value prescribed.

The algorithm ends when at least one of these test is satisfied.

Appendix B

Constrained optimisation problem: Lagrange multiplier method

For an ideal DEG in plane-strain loading mode, the explicit expression for the dimensionless harvested energy

$$\begin{aligned} H_g = & \frac{1}{2}(\lambda_A - \lambda_D)\left[\lambda_D\left(3\bar{\phi}_D^2 - 1\right) + 2\lambda_A + 3\lambda_D^{-3}\right] \\ & + \frac{1}{2}(\lambda_C - \lambda_B)\left[\lambda_B\left(3\bar{\phi}_B^2 - 1\right) + 2\lambda_C + 3\lambda_B^{-3}\right]. \end{aligned} \tag{B.1}$$

involves only the squares of the variables $\bar{\phi}_B$ and $\bar{\phi}_D$. Therefore it is convenient to derive $\bar{\phi}_B^2$ and $\bar{\phi}_D^2$ from conditions (2.31) as functions of the stretches λ_A, λ_B, λ_C and λ_D and substitute them in Eq. (B.1). This will lead to an expression for H_g in terms of the four characteristic stretches. Similar developments can be followed for the constraints defining the failure envelope, whose final expressions determined for all the functions involved are outlined next.

In order to determine the optimal cycle, out of which the maximum energy can be harvested, within the region of admissible states, we formulate the following constrained optimisation problem:

$$\text{find} \min_{\mathbf{\Lambda}} H_g[\lambda_A, \lambda_B, \lambda_C, \lambda_D]$$

with $\mathbf{\Lambda} = [\lambda_A, \lambda_B, \lambda_C, \lambda_D]^T$ and the minimum is sought since $H_g \leq 0$. The optimisation is to be evaluated under the following constraints:

- Equality constraint (active constraint)

  $$f[\lambda_A, \lambda_B, \lambda_C, \lambda_D] = -\lambda_C + \lambda_U = 0;$$

  The simplicity of this constraint enabled us to substitute λ_U for λ_C throughout the Lagrangian function and reduce the set of optimisation variables $\mathbf{\Lambda}$ to $\mathbf{\Lambda}_R = [\lambda_A, \lambda_B, \lambda_D]^T$.

- Inequality constraints (possibly active constraints)

  $$\begin{aligned}
  &k_1[\lambda_A, \lambda_B, \lambda_C, \lambda_D] = S^D_{33}[\lambda_A, \lambda_B, \lambda_C, \lambda_D] \geq 0,\\
  &k_2[\lambda_A, \lambda_B, \lambda_C, \lambda_D] = -\bar{E}^2_D[\lambda_A, \lambda_B, \lambda_C, \lambda_D] + \bar{E}^2_{eb} \geq 0,\\
  &k_3[\lambda_A, \lambda_B, \lambda_C, \lambda_D] = \bar{\phi}^2_B \geq 0 \quad \text{i.e. } \bar{\phi}_B \in \mathbb{R}, \qquad\qquad \text{(B.2)}\\
  &k_4[\lambda_A, \lambda_B, \lambda_C, \lambda_D] = \lambda_A - 1 \geq 0, \qquad k_5[\lambda_A, \lambda_B, \lambda_C, \lambda_D] = -\lambda_A + \lambda_U \geq 0,\\
  &k_6[\lambda_A, \lambda_B, \lambda_C, \lambda_D] = \lambda_B - 1 \geq 0, \qquad k_7[\lambda_A, \lambda_B, \lambda_C, \lambda_D] = -\lambda_B + \lambda_U \geq 0,\\
  &k_8[\lambda_A, \lambda_B, \lambda_C, \lambda_D] = \lambda_D - 1 \geq 0, \qquad k_9[\lambda_A, \lambda_B, \lambda_C, \lambda_D] = -\lambda_D + \lambda_U \geq 0.
  \end{aligned}$$

The detailed expressions for the objective function H_g and the contraints k_1, k_2, k_3 as functions of the stretches are:

$$\begin{aligned}
H_g[\lambda_A, \lambda_B, \lambda_C, \lambda_D] \;=\; & \frac{1}{2(\lambda_A^3\lambda_C^3 - \lambda_B^3\lambda_D^3)}\Big[- \lambda_C^3\lambda_A^5 + 3\lambda_D\left(\lambda_C^3 - \lambda_D^2\lambda_C + \lambda_B\lambda_D^2\right)\lambda_A^4\\
& - \left[3(\lambda_B - \lambda_C)\lambda_D^4 + 2\lambda_C^3\lambda_D^2 + \lambda_C^3\left(2\lambda_B^2 - 3\lambda_C\lambda_B + \lambda_C^2\right)\right]\lambda_A^3\\
& -2\lambda_B^3\lambda_D^3\lambda_A^2 + 3\lambda_B^3\left[\lambda_D^4 + (\lambda_B - \lambda_C)\lambda_C^3\right]\lambda_A\\
& -\lambda_B^3\lambda_D\left[\lambda_D^4 + (\lambda_B - 2\lambda_C)(\lambda_B - \lambda_C)\lambda_D^2 + 3(\lambda_B - \lambda_C)\lambda_C^3\right]\Big],
\end{aligned}$$

$$\begin{aligned}
k_1[\lambda_A, \lambda_B, \lambda_C, \lambda_D] &= \frac{\lambda_A^4\lambda_C^3\lambda_D - \lambda_A^3\lambda_C^3\left(\lambda_D^2 - 1\right) - \lambda_B^3\lambda_D\left(\lambda_B\lambda_C^3 - \lambda_C^4 + \lambda_D^2\right)}{\lambda_A^3\lambda_C^3 - \lambda_B^3\lambda_D^3},\\
k_2[\lambda_A, \lambda_B, \lambda_C, \lambda_D] &= \frac{\lambda_A^4\lambda_C^3\lambda_D^3 - \lambda_A^3\lambda_C^3\left(\lambda_D^4 - 1\right) - \lambda_B^3\lambda_D^3\left(\lambda_B\lambda_C^3 - \lambda_C^4 + 1\right)}{\lambda_D^2(\lambda_A^3\lambda_C^3 - \lambda_B^3\lambda_D^3)} + \bar{E}^2_{eb},\\
k_3[\lambda_A, \lambda_B, \lambda_C, \lambda_D] &= \frac{-\left(\lambda_A^4 - 1\right)\lambda_B^3\lambda_D^3 + \lambda_A^3\lambda_B^3\lambda_D^4 + \lambda_A^3\lambda_C^3\left(\lambda_B^4 - \lambda_B^3\lambda_C - 1\right)}{\lambda_B^4(\lambda_A^3\lambda_C^3 - \lambda_B^3\lambda_D^3)}.
\end{aligned}$$

The following generalized Lagrangian function is evaluated

$$\mathcal{L}[\lambda_A,\lambda_B,\lambda_D,\gamma_1,\gamma_2,\gamma_3,\gamma_4,\gamma_5,\gamma_6,\gamma_7,\gamma_8,\gamma_9] = \\ H_g[\lambda_A,\lambda_B,\lambda_U,\lambda_D] - \sum_{i=1}^{9} \gamma_i\, k_i[\lambda_A,\lambda_B,\lambda_U,\lambda_D],$$

therefore, at every admissible (i.e. satisfying all the constraints) local minimum $\tilde{\mathbf{\Lambda}}_R$, the following Karush–Kuhn–Tucker conditions are to be verified:

$$\begin{cases} \nabla_{\mathbf{\Lambda}_R}\mathcal{L}[\tilde\lambda_A,\tilde\lambda_B,\tilde\lambda_D,\tilde\gamma_1,\tilde\gamma_2,\tilde\gamma_3,\tilde\gamma_4,\tilde\gamma_5,\tilde\gamma_6,\tilde\gamma_7,\tilde\gamma_8,\tilde\gamma_9] = 0, \\ k_i[\tilde\lambda_A,\tilde\lambda_B,\lambda_U,\tilde\lambda_D] \geq 0 \qquad (i=1,\dots,9), \\ \tilde\gamma_i \geq 0 \qquad\qquad\qquad\qquad\; (i=1,\dots,9), \\ \tilde\gamma_i\, h_i[\tilde\lambda_A,\tilde\lambda_B,\lambda_U,\tilde\lambda_D] = 0 \quad (i=1,\dots,9). \end{cases}$$

The gradient operator corresponds to the operation

$$\nabla_{\mathbf{\Lambda}_R}\mathcal{L} = \{\partial\mathcal{L}/\partial\lambda_A,\;\; \partial\mathcal{L}/\partial\lambda_B,\;\; \partial\mathcal{L}/\partial\lambda_D\}^T,$$

where the independent variables have been omitted for the sake of conciseness. Finally, the stationarity condition reads:

$$\nabla_{\mathbf{\Lambda}_R}\mathcal{L}[\lambda_A,\lambda_B,\lambda_D,\gamma_1,\gamma_2,\gamma_3,\gamma_4,\gamma_5,\gamma_6,\gamma_7,\gamma_8,\gamma_9] = \\ \nabla_{\mathbf{\Lambda}_R}H_g[\lambda_A,\lambda_B,\lambda_U,\lambda_D] - \sum_{i=1}^{9}\gamma_i\,\nabla_{\mathbf{\Lambda}_R}k_i[\lambda_A,\lambda_B,\lambda_U,\lambda_D] = 0.$$

Appendix C

Annular membrane solving procedure: numerical shooting method

On the basis of simple trigonometric relationships, we can rephrase Eq. (5.2) in terms of the functions $r(r_0)$ and $z(r_0)$ as

$$r' = \lambda_1 \cos\theta, \qquad z' = -\lambda_1 \sin\theta. \tag{C.1}$$

A combination of the equilibrium equations (5.8) and (5.9) gives

$$\theta' = -\frac{S_2}{S_1 r_0} \sin\theta. \tag{C.2}$$

Equations $(C.1)_1$, (C.2) and (5.8) constitute the system of non-linear differential algebraic equations (DAEs) in the three unknowns $r(r_0)$, $\theta(r_0)$ and $\lambda_1(r_0)$. This system must be integrated with the boundary conditions $(5.1)_{1,2}$.

For the solution of this boundary value problem we employ the *numerical shooting method*. This is a numerical technique for solving a boundary value problem by reducing it to the solution of an initial value problem. Once the applied force $\mathcal{F}$ and the voltage ϕ are imposed, the system is solved with the initial conditions $r(r_0^i) = \lambda_{pre} r_0^i$ and $\lambda_1(r_0^i) = \lambda_1^i$. The boundary constraint $r(r_0^e) = \lambda_{pre} r_0^e$ is imposed comparing iteratively the actual solution with the target, updating at each step the initial value λ_1^i.

Once the system is solved, the function $z(r_0)$ could be consequently determined integrating the differential equation $(C.1)_2$ with the boundary condition $(5.1)_3$.

Bibliography

[1] I.A. Anderson, T.A. Gisby, T.G. McKay, B.M. O'Brien, and E.P. Calius. Multifunctional dielectric elastomer artificial muscles for soft and smart machines. *J. Appl. Phys.*, 112:041101, 2012. doi:10.1063/1.4740023. pages

[2] A. Ask, A. Menzel, and M. Ristinmaa. Electrostriction in electro-viscoelastic polymers. *Mech. Mat.*, 50:9–21, 2012. doi:10.1016/j.mechmat.2012.01.009. pages

[3] A. Ask, A. Menzel, and M. Ristinmaa. Phenomenological modeling of viscous electrostrictive polymers. *Int. J. Non-Linear Mech.*, 47(2):156–165, 2012. doi:10.1016/j.ijnonlinmec.2011.03.020. pages

[4] G. Berselli, R. Vertechy, G. Vassura, and V. Parenti-Castelli. Optimal synthesis of conically shaped dielectric elastomer linear actuators: Design methodology and experimental validation. *IEEE/ASME Trans. Mechatronics*, 16(1):67–79, 2011. doi:10.1109/TMECH.2010.2090664. pages

[5] K. Bertoldi and M. Gei. Instabilities in multilayered soft dielectrics. *J. Mech. Phys. Solids*, 59(1):18–42, 2011. doi:10.1016/j.jmps.2010.10.001. pages

[6] E. Bortot, G. deBotton, and M. Gei. Optimal energy harvesting cycles for load-driven dielectric elastomer generators under equibiaxial deformation. *Meccanica*, 50(11):2751–2766, 2015. doi:10.1007/s11012-015-0213-1. pages

[7] R. Bustamante, A. Dorfmann, and R.W. Ogden. On electric body forces and maxwell stresses in nonlinearly electroelastic solids. *Int. J. Engin. Science*, 47 (11–12):1131–1141, 2009. doi:10.1016/j.ijengsci.2008.10.010. pages

[8] R. Bustamante, A. Dorfmann, and R.W. Ogden. Nonlinear electroelastics: a variational framework. *Z. angew. Math. Phys. (ZAMP)*, 60(1):154–177, 2009. doi:10.1007/s00033-007-7145-0. pages

[9] F. Carpi, D. De Rossi, R. Kornbluh, R. Pelrine, and P. Sommers-Larsen. *Dielectric elastomers as electromechanical transducers – Fundamentals, Materials, Devices, Models and Applications of an Emerging Electroactive Polymer Technology*. Elsevier, Oxford, UK, 2008. pages

[10] S. Chiba, M. Waki, R. Kornbluh, and R. Pelrine. Current status and future prospects of power generators using dielectric elastomer. *Smart Mater. Struct.*, 20(12):124006, 2011. doi:10.1088/0964-1726/20/12/124006. pages

[11] L. Daniele. Ocean wave energy: design of STEWEC, an innovative wave energy converter (WEC). Master's thesis, DISMI – Dept. of Sciences and Methods for Engineering, University of Modena and Reggio Emilia, 2014. pages

[12] D. De Tommasi, G. Puglisi, and G. Zurlo. Inhomogeneous spherical configurations of inflated membranes. *Continuum Mech. Therm.*, 25(2):197–206, 2013. doi:10.1007/s00161-012-0240-2. pages

[13] D. De Tommasi, G. Puglisi, and G. Zurlo. Electromechanical instability and oscillating deformations in electroactive polymer films. *Appl. Phys. Lett.*, 102:011903, 2013. doi:10.1063/1.4772956. pages

[14] L. Di Lillo, A. Schmidt, D. A. Carnelli, P. Ermanni, G. Kovacs, E. Mazza, and A. Bergamini. Measurement of insulating and dielectric properties of acrylic elastomer membranes at high electric fields. *J. Appl. Phys.*, 111:024904, 2012. doi:10.1063/1.3676201. pages

[15] A. Dorfmann and R.W. Ogden. Nonlinear electroelasticity. *Acta Mech.*, 174(3):167–183, 2005. doi:10.1007/s00707-004-0202-2. pages

[16] A. Dorfmann and R.W. Ogden. Nonlinear electroelastic deformations. *J. Elasticity*, 82(2):99–127, 2006. doi:10.1007/s10659-005-9028-y. pages

[17] A. Dorfmann and R.W. Ogden. Nonlinear electroelastostatics: Incremental equations and stability. *Int. J. Engng. Science*, 48(1):1–14, 2010. doi:10.1016/j.ijengsci.2008.06.005. pages

[18] A. Fainleib, R.V. Pires, E.F. Lucas, and B.G. Soares. Degradation of non-vulcanized natural rubber - renewable resource for fine chemicals used in polymer synthesis. *Polimeros*, 23(4):441–450, 2013. doi:10.4322/polimeros.2013.070. pages

[19] C.C. Foo, S.J.A. Koh, C. Keplinger, R. Kaltseis, S. Bauer, and Z. Suo. Performance of dissipative dielectric elastomer generators. *J. Appl. Phys.*, 111:094107, 2012. doi:10.1063/1.4714557. pages

[20] G. Gallone, F. Carpi, D. De Rossi, G. Levita, and A. Marchetti. Dielectric constant enhancement in a silicone elastomer filled with lead magnesium niobate–lead titanate. *Mater. Sci. Eng. C*, 27(1):110–116, 2007. doi:10.1016/j.msec.2006.03.003. pages

[21] M. Gei, S. Colonnelli, and R. Springhetti. A framework to investigate instabilities of homogeneous and composite dielectric elastomer actuators. In Y. Bar-Cohen, editor, *Electroactive Polymer Actuators and Devices (EAPD)*, volume 8340 of *Proc. of SPIE*, page 834010, 2012. doi:10.1117/12.915340. pages

[22] M. Gei, S. Colonnelli, and R. Springhetti. The role of electrostriction on the stability of dielectric elastomer actuators. *Int. J. Solids Structures*, 51(3–4):848–860, 2014. doi:10.1016/j.ijsolstr.2013.11.011. pages

[23] H. Haus, M. Matysek, H. Mössinger, K. Flittner, and H.F. Schlaak. Electrical modeling of dielectric elastomer stack transducers. In Y. Bar-Cohen and F. Carpi, editors, *Electroactive Polymer Actuators and Devices (EAPD)*, volume 8687 of *Proc. of SPIE*, page 86871D, 2013. doi:10.1117/12.2009959. pages

[24] T. He, X. Zhao, and Z. Suo. Dielectric elastomer membranes undergoing inhomogeneous deformation. *J. Appl. Phys.*, 106:083522, 2009. doi:10.1063/1.3253322. pages

[25] J. Huang, S. Shian, Z. Suo, and D.R. Clarke. Maximizing the energy density of dielectric elastomer generators using equi-biaxial loading. *Adv. Funct. Mat.*, 23(40): 5056–5061, 2013. doi:10.1002/adfm.201300402. pages

[26] J. Huang, S. Shian, Z. Suo, and D.R. Clarke. Dielectric elastomer generator with equi-biaxial mechanical loading for energy harvesting. In Y. Bar-Cohen and F. Carpi, editors, *Electroactive Polymer Actuators and Devices (EAPD)*, volume 8687 of *Proc. of SPIE*, pages 86870Q–3, 2013. doi:10.1117/12.2009724. pages

[27] K. Hutter, A.A.F. van de Ven, and A. Ursescu. *Electromagnetic Field Matter Interactions in Thermoelastic Solids and Viscous Fluids.* Springer, Berlin, DE, 2006. pages

[28] NTE Electronics Inc. Nte517 silicon high voltage plastic rectifier data sheet. URL `http://www.nteinc.com/specs/500to599/pdf/nte517.pdf`. pages

[29] K. Jung, J. Lee, M. Cho, J.C. Koo, J. Nam, Y. Lee, and H.R. Choi. Development of enhanced synthetic elastomer for energy-efficient polymer actuators. *Smart Mater. Struct.*, 16(2):S288–S294, 2007. doi:10.1088/0964-1726/16/2/S13. pages

[30] R. Kaltseis, C. Keplinger, R. Baumgartner, M. Kaltenbrunner, T. Li, P. Mächler, R. Schwödiauer, Z. Suo, and S. Bauer. Method for measuring energy generation and efficiency of dielectric elastomer generators. *Appl. Phys. Lett.*, 99:162904, 2011. doi:10.1063/1.3653239. pages

[31] R. Kaltseis, C. Keplinger, S.J.A. Koh, R. Baumgartner, Y.F. Goh, W.H. Ng, A. Kogler, A. Tröls, C.C. Foo, Z. Suo, and S. Bauer. Natural rubber for sustainable high-power electrical energy generation. *RCS Adv.*, 4(53):27905–27913, 2014. doi:10.1039/c4ra03090g. pages

[32] R. Karsten, P. Lotz, and H.F. Schlaak. Active suspension with multilayer dielectric elastomer actuator. In Y. Bar-Cohen and F. Carpi, editors, *Electroactive Polymer Actuators and Devices (EAPD)*, volume 7976 of *Proc. of SPIE*, page 79762M, 2011. doi:10.1117/12.880459. pages

[33] C. Keplinger, M. Kaltenbrunner, N. Arnold, and Bauer S. Rontgen's electrode–free elastomer actuators without electromechanical pull–in instability. *Proc. Natl. Acad. Sci. U.S.A.*, 107:4505–4510, 2010. doi:10.1073/pnas.0913461107. pages

[34] B. Kleuter, A. Menzel, and P. Steinmann. Generalized parameter identification for finite viscoelasticity. *Comput. Meth. Appl. Mech. Engrg.*, 196(35–36):3315–3334, 2007. doi:10.1016/j.cma.2007.03.010. pages

[35] G. Kofod, R. Kornbluh, R. Pelrine, and P. Sommer-Larsen. Actuation response of polyacrylate dielectric elastomers. *J. Intell. Mater. Syst. and Struct.*, 14(12): 787–793, 2003. doi:10.1177/1045389903039260. pages

[36] S.J.A. Koh, X. Zhao, and Z. Suo. Maximal energy that can be converted by a dielectric elastomer generator. *Appl. Phys. Lett.*, 94:262902, 2009. doi:10.1063/1.3167773. pages

[37] S.J.A. Koh, C. Keplinger, T. Li, S. Bauer, and Z. Suo. Dielectric elastomer generators: how much energy can be converted? *IEEE/ASME Trans. on Mechatronics*, 16(1):33–41, 2011. doi:10.1109/TMECH.2010.2089635. pages

[38] R.D. Kornbluh, R. Pelrine, H. Prahlad, A. Wong-Foy, B. McCoy, S. Kim, J. Eckerle, and Low T. From boots to buoys: promises and challenges of dielectric elastomer energy harvesting. In Y. Bar-Cohen and F. Carpi, editors, *Electroactive Polymer Actuators and Devices (EAPD)*, volume 7976 of *Proc. of SPIE*, page 797605, 2011. doi:10.1117/12.882367. pages

[39] M. Lallart, P.J. Cottinet, D. Guyomar, and L. Lebrun. Electrostrictive polymers for mechanical energy harvesting. *J. Polym. Sci. Part B Polym. Phys.*, 50(8):523–535, 2012. doi:10.1002/polb.23045. pages

[40] T. Lu, J. Huang, C. Jordi, G. Kovacs, R. Huang, D.R. Clarke, and Z. Suo. Dielectric elastomer actuators under equal-biaxial forces, uniaxial forces and uniaxial constraint of stiff fibers. *Soft Matter*, 8(22):6167–6173, 2012. doi:10.1039/c2sm25692d. pages

[41] J. Lubliner. A model of rubber viscoelasticity. *Mech. Res. Comm.*, 12(2):93–99, 1985. doi:10.1016/0093-6413(85)90075-8. pages

[42] M. Matysek, H. Haus, H. Mössinger, D. Brokken, P. Lotz, and H.F. Schlaak. Combined driving and sensing circuitry for dielectric elastomer actuators in mobile applications. In Y. Bar-Cohen and F. Carpi, editors, *Electroactive Polymer Actuators and Devices (EAPD)*, volume 7976 of *Proc. of SPIE*, page 797612, 2011. doi:10.1117/12.879438. pages

[43] G.A. Maugin. *Continuum Mechanics of Electromagnetic Solids*. North-Holland, Amsterdam, NL, 1988. pages

[44] T.G. McKay, B.M. O'Brien, E.P. Calius, and I.A. Anderson. Soft generators using dielectric elastomers. *Appl. Phys. Lett.*, 98:142903, 2011. doi:10.1063/1.3572338. pages

[45] R.M. McMeeking and C.M. Landis. Electrostatic forces and stored energy for deformable dielectric materials. *J. Appl. Mech., Trans. ASME*, 72(4):581–590, 2005. doi:10.1115/1.1940661. pages

[46] S. Michel, X.Q. Zhang, M. Wissler, C. Löwe, and G. Kovacs. A comparison between silicone and acrylic elastomer as dielectric materials in electroactive polymer actuators. *Polym. Int.*, 59(3):391–399, 2010. doi:10.1002/pi.2751. pages

[47] J.A. Nelder and R. Mead. A simplex method for function minimization. *Comput. J.*, 7(4):308–313, 1965. doi:10.1093/comjnl/7.4.308. pages

[48] A. O'Halloran, F. O'Malley, and P. McHugh. A review on dielectric elastomer actuators, technology, applications and challenges. *J. Appl. Phys.*, 104:071101, 2008. doi:10.1063/1.2981642. pages

[49] J.S. Plante and S. Dubowsky. Large-scale failure modes of dielectric elastomer actuators. *Int. J. Solids Struct.*, 43(25–26):7727–7751, 2006. doi:10.1016/j.ijsolstr.2006.03.026. pages

[50] S. Reese and S. Govindjee. A theory of finite viscoelasticity and numerical aspects. *Int. J. Solids Structures*, 35:3455–3482, 1998. pages

[51] L.J. Romasanta, P. Leret, L. Casaban, M. Hernandez, M.A. de la Rubia, J.F. Fernandez, J.M. Kenny, M.A. Lopez-Manchado, and R. Verdejo. Towards materials with enhanced electro–mechanical response: $CaCu_3Ti_4O_{12}$–polydimethylsiloxane composites. *J. Mater. Chem.*, 22(47):24705–24712, 2012. doi:10.1039/c2jm34674e. pages

[52] S. Rudykh and G. deBotton. Stability of anisotropic electroactive polymers with application to layered media. *Z. angew. Math. Phys. (ZAMP)*, 62(6):1131–1142, 2011. doi:10.1007/s00033-011-0136-1. pages

[53] S. Rudykh, K. Bhattacharya, and G. deBotton. Snap-through actuation of thick-wall electroactive balloons. *Int. J. Nonlinear Mech.*, 47(2):206–209, 2012. doi:10.1016/j.ijnonlinmec.2011.05.006. pages

[54] R. Sarban, B. Lassen, and M. Willatzen. Dynamic electromechanical modeling of dielectric elastomer actuators with metallic electrodes. *IEEE/ASME Transactions on Mechatronics*, 17(5):960–967, 2012. doi:10.1109/TMECH.2011.2150239. pages

[55] M. Schuster and R. Unbehauen. Analysis of nonlinear electric networks by means of differential algebraic equations solvers. *Electrical Engineering*, 88(3):229–239, 2006. doi:10.1007/s00202-004-0278-7. pages

[56] S.K. Sharma, H. Gaur, M. Kulkarni, G. Patil, B. Bhattacharya, and A. Sharma. PZT–PDMS composite for active damping of vibrations. *Compos. Sci. Technol.*, 77:42–51, 2013. doi:10.1016/j.compscitech.2013.01.004. pages

[57] R. Springhetti, E. Bortot, G. deBotton, and M. Gei. Optimal energy-harvesting cycles for load-driven dielectric generators in plane strain. *IMA J. Appl. Math.*, 79 (5):929–946, 2014. doi:10.1093/imamat/hxu025. pages

[58] V.L. Tagarielli, R. Hildick-Smith, and J.E. Huber. Electro-mechanical properties and electrostriction response of a rubbery polymer for eap applications. *Int. J. Solids Structures*, 49(23–24):3409–3415, 2012. doi:10.1016/j.ijsolstr.2012.07.018. pages

[59] T.E. Tezduyar, L.T. Wheeler, and L. Graux. Finite deformation of a circular elastic membrane containing a concentric rigid inclusion. *Int. J. Non-Linear Mechanics*, 22(1):61–72, 1987. doi:10.1016/0020-7462(87)90049-7. pages

[60] A. Tröls, A. Kogler, R. Baumgartner, R. Kaltseis, C. Keplinger, R. Schwödiauer, I. Graz, and S. Bauer. Stretch dependence of the electrical breakdown strength and dielectric constant of dielectric elastomers. *Smart Mater. Struct.*, 22(10):104012, 2013. doi:10.1088/0964-1726/22/10/104012. pages

[61] R. Vertechy, M. Fontana, G.P. Rosati Papini, and M. Bergamasco. Oscillating-water-column wave-energy-converter based on dielectric elastomer generator. In Y. Bar-Cohen, editor, *Electroactive Polymer Actuators and Devices (EAPD)*, volume 8687 of *Proc. of SPIE*, page 86870I, 2013. doi:10.1117/12.2012016. pages

[62] T. Vu-Cong, C. Jean-Mistral, and A. Sylvestre. New operating limits for applications with electroactive elastomer: effect of the drift of the dielectric permittivity and the electrical breakdown. In Y. Bar-Cohen, editor, *Electroactive Polymer Actuators and Devices (EAPD)*, volume 8687 of *Proc. of SPIE*, page 86871S, 2013. doi:10.1117/12.2007698. pages

[63] X. Wu, W. Sun, M. Li, and J. Zhou. Electromechanical stability of cone dielectric elastomer actuator. In *13th International Conference on Fracture 2013, ICF 2013*, volume 6, pages 4418–4422, 2013. URL `http://www.gruppofrattura.it/ocs/index.php/ICF/icf13/paper/viewFile/11504/10883`. pages

[64] Y. Zhu, H. Wang, D. Zhao, and J. Zhao. Energy conversion analysis and performance research on a cone-type dielectric electroactive polymer generator. *Smart Mater. Struct.*, 20(11):115022, 2011. doi:10.1088/0964-1726/20/11/115022. pages